國 立 交 通 大 學

機 械 工 程 學 系

博 士 論 文

非矽基垂直式梳狀元件之製程研究

Novel Fabrication Schemes for Non-Silicon-Based Vertical Comb Drive

研 究 生：鍾君煒

指導教授：徐文祥 教授

中 華 民 國 九十六 年 十 月

非矽基垂直式梳狀元件之製程研究

Novel Fabrication Schemes for Non-Silicon-Based Vertical Comb Drive

研 究 生：鍾君煒　　Student: Junwei Chung

指導教授：徐文祥　　Advisor: Wensyang Hsu

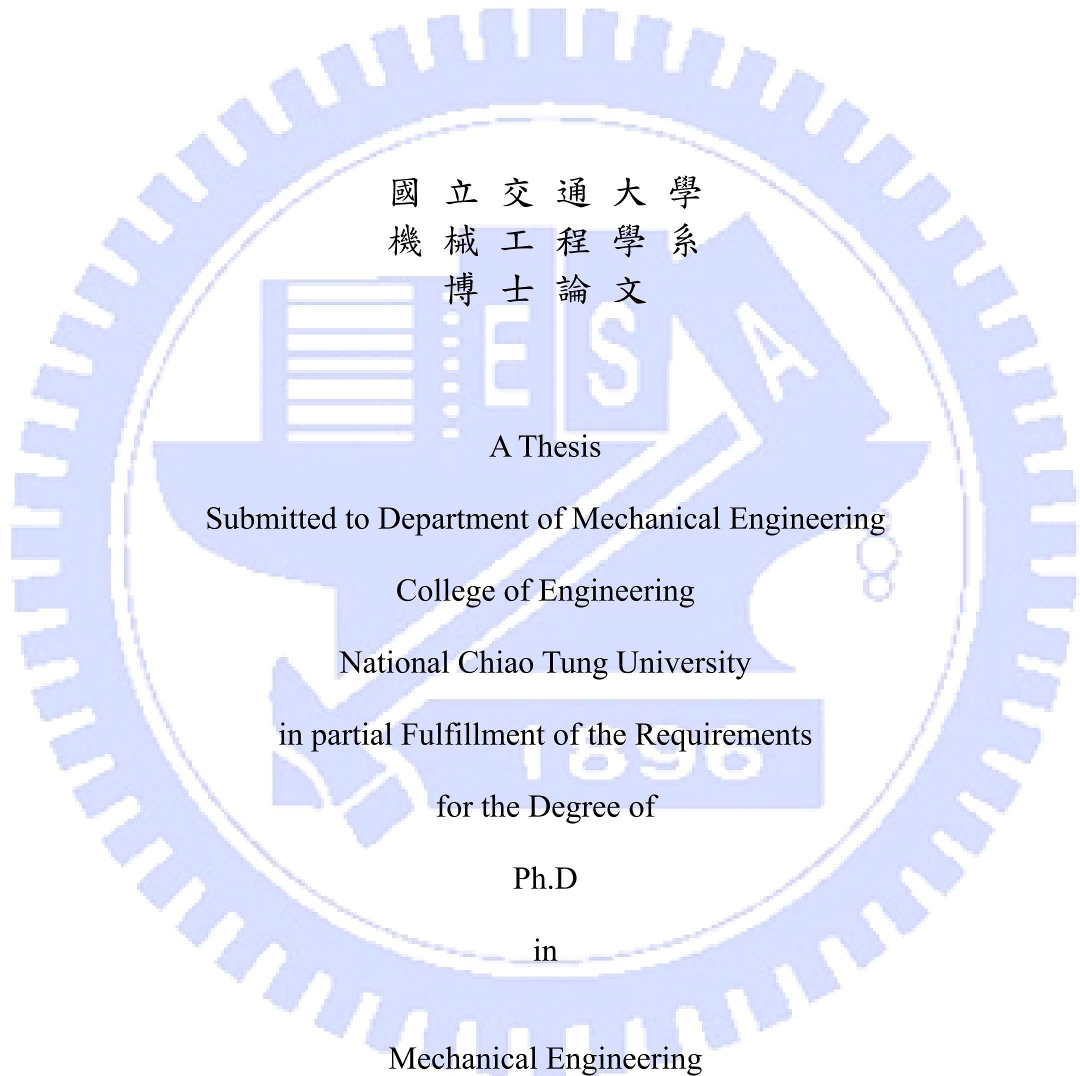

國 立 交 通 大 學
機 械 工 程 學 系
博 士 論 文

A Thesis

Submitted to Department of Mechanical Engineering

College of Engineering

National Chiao Tung University

in partial Fulfillment of the Requirements

for the Degree of

Ph.D

in

Mechanical Engineering

October 2007

Hsinchu, Taiwan, Republic of China

中 華 民 國 九十六 年 十 月

非矽基垂直式梳狀元件之製程研究

學生：鍾君煒　　　　　　　　　　　　　　　　指導教授：徐文祥

國立交通大學機械工程學系（研究所）博士班

摘　要

由於優異的出平面運動特性，垂直式梳狀致動器如今已成為熱門的微機電元件。至今為止，所有被發展出來的垂直式梳狀致動器皆以矽基微加工技術進行製作，並以矽作為結構的材料。然而，這些必須由深反應離子蝕刻(DRIE)進行加工，並以 SOI 晶片為主的技術，也意味著較高的製作成本。相對於矽基材料，金屬與高分子正發展成為極具吸引力的替代性材料，可用來製作低成本的微元件以取代矽基元件。然而，至今仍未見有文獻利用高分子或金屬製作垂直式梳狀致動器。

本論文提出兩種新式的製作方法用以製作高分子與金屬垂直式梳狀致動器，這兩種方法皆屬低溫及低成本的製程，在僅需類 LIGA 製程基礎設備的狀況下，提供了高可適性以及容易負擔的製作方案。首先，論文中對垂直式梳狀致動器進行理論及有限元素分析，以便進行尺寸上的設計。接著，為了製作高分子垂直式梳狀致動器，此處提出一雙面多重部分曝光(DoMPE)的製程平台，此平台經由正面及背面的多階曝光，可有效擴充懸浮光阻結構的外形複雜度。經由此平台及其所建立的參數資料庫，各種複雜的三維光阻結構及垂直式梳狀致動器皆被成功製作及展示。在比較理論分析及實驗結果之後，以高分子製作垂直式梳狀致動器的可行性已被成功驗證。

在金屬垂直式梳狀致動器的製作方面，首先對電鑄鎳進行材料特性調查，並發現電鑄鎳的材料特性會隨著厚度及電流密度的變化而有明顯的改變，這對設計鎳元件而言將很有幫助。在製程上，電鑄鎳與銅分別被用來當作結構層及犧牲層，在交替電鑄鎳與銅之下建構出垂直式梳狀致動器的結構，最後再由濕式蝕刻進行結構釋放。此外，經由控制光阻的斜角，亦可藉由此方法製作具有斜角的垂直式梳狀致動器。

Novel Fabrication Schemes for Non-Silicon-Based Vertical Comb Drive

Student: Junwei Chung Advisor: Wensyang Hsu

Department of Mechanical Engineering
National Chiao Tung University

Abstract

In recent MEMS research, vertical comb drives (VCDs) have attracted lots of attention due to their superior characteristics in out-of-plane motion. To date, all the reported VCDs were fabricated by silicon-based micromachining with using silicon as the structural material, and exhibit a high cost solution with the DRIE process and the mainly required SOI-wafers. In contrast to silicon, the metals and polymers are becoming attractively alternative materials for fabricating the low cost micro devices and components to their silicon or glass-based counterparts. However, no polymer or metal-based VCDs have been reported yet.

In this dissertation, novel fabrication methods are proposed to fabricate the VCDs in different materials—polymer and metal. Both of them are low temperature and low cost techniques, and provide a flexible and affordable solution with the basic equipment of LIGA-like process. First, the operation model of VCD is performed with theoretical analysis and FEM simulation for dimensional design. For the fabrication of polymer-based VCD, the double-side multiple partial exposure (DoMPE) method is developed to extend the multi-level morphology on both the front and back sides of the suspended photoresist microstructures. Depending on the established processing data, different 3D photoresist microstructures made of photoresist AZ9260® are successfully demonstrated, as well as the polymer-based VCD. By comparing the analytical and experimental results, the feasibility on fabricating polymer-based VCD is verified.

For the fabrication of metal-based VCD, the properties of electroplated nickel are first characterized with different thicknesses and current densities, and obvious variations on material properties are observed, which would be helpful in designing micro devices by using electroplated nickel as structural material. To fabricate the metal-based VCD, electroplated nickel and copper are used as the structural and sacrificial layers. By electrodepositing nickel and copper in turn with thick photoresist as the molds, the VCD structures are constructed with the final release performed by wet etching. Also, the VCD with angled fingers could be further realized by controlling the angle of photoresist sidewall by this approach.

誌　謝

本論文能夠順利完成，首先要感謝我的指導教授徐文祥老師。徐老師開明與鼓勵的態度，提供了學生寬廣的想像與自主空間，在不斷的腦力激盪之下，讓我有機會將自己的想法落實在研究上。在這過程中，有興奮，也有挫折；有時思路清晰，有時夾雜不清；有時覺得自己的研究是件寶貝，有時卻覺得是堆壞掉的有機物。但是不管如何，徐老師總能用聰明的方法提醒我，並鼓勵我，讓我能夠嘗試修正錯誤，繼續堅持下去。徐老師的態度總讓人感覺亦師亦友，不僅在研究上給予指導，也常常能夠在人生上給予寶貴的意見。永遠令我印象深刻的是老師對局勢的分析，總讓我目瞪口呆地佩服。

其次要感謝交大電控邱俊誠老師、交大電工鄭裕庭老師、清大動機陳榮順老師、師大機電楊啟榮老師與同步輻射中心許博淵博士能夠在百忙之中撥冗參與學生的論文口試，並給予研究方向上的寶貴意見。此外，還要感謝系上周長彬老師、洪景華老師及楊秉祥老師，在颱風天竟然能夠如此情意相挺地參與學生的論文公開演講，並給予許多研究上的建議，除了讓學生的論文能夠更加完整之外，更令飽受颱風之苦的學生倍感溫馨。

徐老師除了提供了自由的研究空間，亦提供了感情融洽並且設備豐富的研究室。在研究室的成員中，首先要感謝青臺學長、政璋學長、鎮鵬學長及正軒學長，在我碩士班剛進研究室還搞不清楚微機電是圓是扁的時後，你們便如長者般的提攜著我，在專業知識上幫我解惑，在實驗上給予幫助。接著要感謝曹俊杰學長，碩士班時承蒙照顧，並帶領我首次踏入微機電的實作。還要感謝雄章學長，雖然我們很少見面，但每次從你手中接到 CTE 量測儀，心中總是萬分感念。當然還要感謝潘吉祥學長能夠借我們 CTE 量測儀。感謝郁欣學長，不管是碩士班還是博士班，總能互相討論論文，不斷互相鼓勵，並分享各種研究與工作上的心得及資訊，在實驗上也協助良多，希望明年能聽到你拿到學位的好消息。感謝涵評，你升上博士班之後，是第一個幫我分憂

的人，在互吐苦水及互相鼓勵之中，渡過了多年的風風雨雨，果真是艱苦中的好伙伴，也恭喜你即將畢業。感謝駿偉，從我手中接過去不少實驗設備，還接微光機電負責學生的職務，辛苦你了。感謝家聖、毅家及元德在實驗上的協助，尤其在 CIC 進行的靜態及動態量測。感謝鄧永裕，一起完成了電鍍鎳的性質調查，並留下不少電鍍的書籍讓我參考。另外，實驗室的優秀學弟妹們，耕碩、家維、仁宏、昶志、啟煥、岳剛，和你們的相處讓我的生活更為豐富、快樂，謝謝你們。

若沒有國家毫微米實驗室與交大奈米中心的設備支援，這研究是無法完成的。感謝葉雙得先生、陳聯珠小姐及范秀蘭小姐在光罩製作上的大力幫忙，感謝林素珠小姐、陳悅婷小姐、胡進章先生及林聖欽先生在製程上的協助，並感謝范揚禎先生在廠務上的幫忙。

最後，我要謝謝我的父母，能提供我一個衣食無缺毫無牽掛的環境，不但自小讓我能專注於學業，更讓我能自由地選擇攻讀博士學位，沒有你們的體諒、包容與毫無止境的支持，便沒有今日的我，謝謝你們為我提供的避風港。還有洛瑩，在我人生最低潮的時候遇見我，必須忍受我在研究上苦無成果的種種煎熬，還能不斷包容我、鼓勵我，陪我耐心走過這段艱辛的日子，謝謝妳為我所承受及付出的一切。

漫漫人生中，博士般的日子是一段獨特的歷程，並不是每個人都有機會擁有。然而能夠選擇擁有的人，卻也未必能如預期般的絢麗與順遂。就如同在人生道路中，你永遠無法得知下一段道路是日光和煦，抑或狂風暴雨，你也無法得知這將會是海撈一票、抑或血本無歸的投資。然而慶幸的是，決定人生所獲得的，原來不是輸贏了多少，而是你究竟又懂了多少。賠光了家產，卻獲得了內心的資產；贏得了世界，卻輸掉了一切。心中的通達明瞭是本，表面的風光浮華是末，千萬別捨本逐末了。與大家共勉之～

Content

摘　要 i

Abstract ii

誌　謝 iii

Content v

List of Tables vii

List of Figures viii

Chapter 1　Introduction 1

1.1 Background and Motivation 1
1.2 Contributions 3
1.3 Dissertation Outline 4

Chapter 2　Operation Principle 6

2.1 VCD with Torsional Motion 6
2.2 Electrostatic Force 7
2.3 Force Balance Analysis 8
2.4 Effect of Angled Fingers 11

Chapter 3　Double-Side Multiple Partial Exposure (DoMPE) 15

3.1 Procedure of DoMPE Method 17
3.1.1 Suspended front-side multi-level microstructures 17
3.1.2 Suspended back-side multi-level microstructures 18
3.2 Photoresist Processing Parameters 20
3.3 Gray-tone Mask 24
3.4 Results of 3D Photoresist Microstructures 25
3.5 Summary 29

Chapter 4　Polymer-Based Vertical Comb Drive 31

4.1 Fabrication Process 31
4.2 Fabrication Results 33
4.3 Characterization and Discussions 35
4.4 Summary 37

Chapter 5　Property Characterization of Electroplated Nickel 38

5.1 Sample Preparation 40

5.2 Measurements 42
5.3 Results and Discussions 44
5.4 Summary 50

Chapter 6 Metal-Based Vertical Comb Drive 51

6.1 Fabrication Process 51
6.1.1 Modified Process of Metal-Based VCD 54
6.1.2 Slope Photoresist for Angled VCD 57
6.2 Results and Discussions 58
6.2.1 Metal-Based VCD by Modified Process 58
6.2.2 Slope Control of Photoresist Sidewall 65
6.3 Summary 69

Chapter 7 Conclusion 71

7.1 Summary 71
7.2 Future Research Direction 73
7.2.1 Other Approaches to Fabricate the Metal-Based VCD 74

References 78

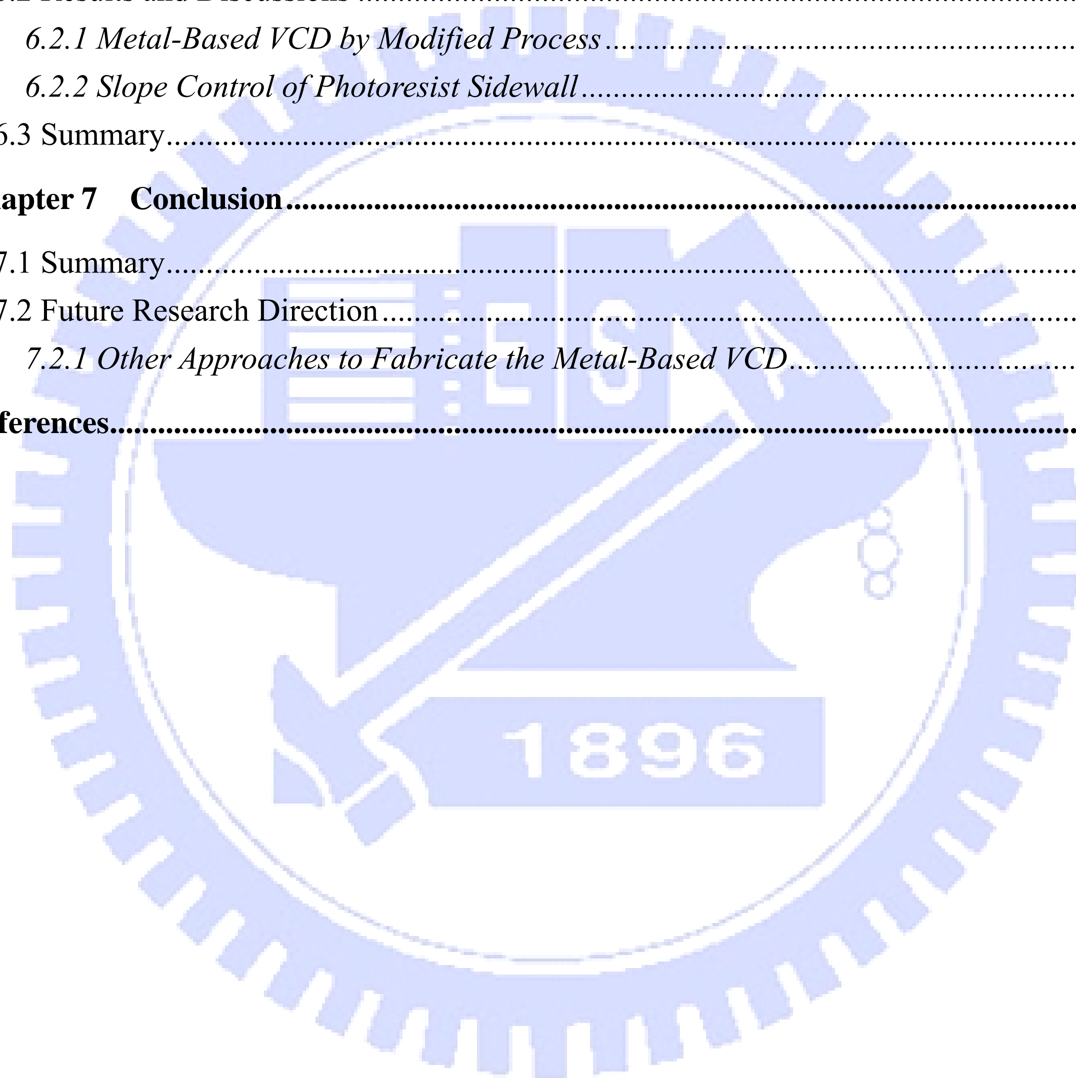

List of Tables

Table 1. The parameters used for the theoretical analysis 10
Table 2. Summary of recent investigations on electroplated nickel; several materials, such as Au, Ti, and Al, are also included. 39
Table 3. The composition of the electrolyte for nickel electroplating. 41
Table 4. The exposure conditions for multiple shifted exposure. (step = 5 μm) 68

List of Figures

Figure 1. The schematic illustration of the vertical comb drive. 6
Figure 2. The simulated cases and results; (a) two simulated cases: with/without the bottom plate; (b) the simulated capacitance of single pair fingers at different displacement, z, and the curve fitting results; the overlap distance is normalized by the finger height of 35 μm. 8
Figure 3. The illustration of the torque induced by electrostatic force from side view of the upper finger and suspending plate, where $T_m(\theta)$ is the induced torque by the mechanical force of the torsion springs 9
Figure 4. The calculated results of the static deflection of vertical comb drive including the cases with or without the bottom plate.. 9
Figure 5. Six cases of VCD are analyzed and discussed; (a) $\theta = 0°$, (b) $\theta = 3°$, (c) $\theta = 6°$, (d) $\theta = 0°$ with bottom plate, (e) $\theta = 3°$ with bottom plate, (f) $\theta = 6°$ with bottom plate. (unit: μm) 11
Figure 6. VCDs without bottom plates; capacitances under different overlap distances are simulated and curve-fitted with finger angles of 0º, 3º, and 6º; the overlap distance is normalized by the finger height of 35 μm. 12
Figure 7. VCDs with bottom plates; capacitances under different overlap distances are simulated and curve-fitted with finger angles of 0º, 3º, and 6º; the overlap distance is normalized by the finger height of 35 μm. 13
Figure 8. The calculated static responses of VCDs (a) without and (b) with bottom plates; the finger angles include 0º, 3º, and 6º. 14
Figure 9. Fabrication of photoresist microstructures with multiple levels on front side; (a) the grove with a depth of d created by front-side partial exposure; (b) the suspending bridge with a space of S created by backside partial exposure; (c) the suspended cantilever with three levels on the front side by front-side multiple partial exposure. 18
Figure 10. Fabrication process of 3D photoresist microstructure with multiple levels on the backside; (a) defining the thick metal film as backside opaque mask; (b) defining the thin metal film as backside gray-tone mask; (c) coating thick positive photoresist; (d) completing backside multiple partial exposure by one exposure; (e) front-side full exposure to define the overall area of structure; (f) development and release. 19
Figure 11. Possible combinations of microstructures fabricated by the DoMPE process with three levels on the front side; (a) six combinations due to two levels on the backside; (b) nine combinations due to three levels on the backside..... 20
Figure 12. Development depth under different development times and exposure

dosages. Photoresist AZ9260® is soft-baked at 90°C for (a) 15 minutes, (b) 60 minutes, and (c) 90 minutes. 21
Figure 13. Bridges made of photoresist AZ9260® with soft-bake time of (a) 40 minutes (b) 90 minutes. 22
Figure 14. Development depth at different development times with or without gentle vibration at two soft-bake times, where the exposure dosage is 394 mJ/cm^2 and the development depths are normalized by overall photoresist thickness of 58 μm. 23
Figure 15. Relationship between development depth and exposure dosage for photoresist AZ9260® at soft-bake time of 90 minutes and development time of 45 minutes. 23
Figure 16. The measured UV-light transmittance at different Ti film thicknesses. 24
Figure 17. Verification on the development depth versus Ti thickness with a photoresist of 58 μm that is soft-baked for 90 minutes and developed for 45 minutes. Line with square symbol is obtained by calculating data in figures 15 and 16. Line with triangle symbol is obtained by direct measurements. 24
Figure 18. 3D microstructures made of photoresist AZ9260® with two levels on the backside; the suspending (a) meander line and (b) coil with one level on the front side; (c)−(d) micro channels with two levels on the front side. 26
Figure 19. 3D microstructures made of photoresist AZ9260® with three levels on the backside and two levels on the front side; (a) microinductor, (b) microstructure with round shape, (c) microstructure with square shape, and (d) mini castle. 27
Figure 20. 3D microstructures made of photoresist AZ9260® with three levels on both the front and back sides; (a)−(b) cantilevers, and (c)−(d) bridges. 28
Figure 21. 3D microstructures made of photoresist AZ9260® by the DoMPE process with four levels on both the front and back sides; (a) cantilevers, (b) bridge. 28
Figure 22. Different beam structures can be fabricated with three levels on both the front and back sides for constructing vertical comb drives with different strokes by the DoMPE process; (a) 9 various beam structures; (b) type I vertical comb structure design with fixed lower comb fingers; (c) type II vertical comb structure design with suspended lower comb fingers. 29
Figure 23. The fabrication process of the polymer VCD on the AA cross-section; (a) defining the Ti film as the backside mask; (b) coating the thick positive photoresist; (c) the front-side partial exposure; (d) the backside partial exposure; (e) the full exposure to define the overall structure; (f) development and release. 32

Figure 24. The fabricated polymer vertical comb drive by DoMPE process; (a) the over view of VCD; (b) the closed view and (c) top view of the finger structures. 34
Figure 25. The dynamic response of vertical comb drive; the peak response is obtained at 6.6 kHz. 36
Figure 26. The mode shapes and natural frequencies of the vertical comb drive; (a) f_1=6.60 kHz, (b) f_2=41.40 kHz, (c) f_3=44.10 kHz, and (d) f_4=54.02 kHz. 36
Figure 27. The experimental and analytical results of the static deflection of vertical comb drive, where the analytical results include the cases with and without bottom plate. 37
Figure 28. The fabrication process of the nickel cantilever beams made by electroforming, (a) photoresist 1 patterning for the sacrificial layer; (b) seed/adhesion layer sputtering and photoresist 2 patterning for the molds; (c) nickel electroplating; (d) release. 41
Figure 29. The experimental setup for the measurement of CTE. 43
Figure 30. The strain sensor to determine the residual strain [14]. (a) Deflection directions with different strain types; (b) pair design to double the deflection. 43
Figure 31. The SEM picture of the fabricated nickel cantilevers for the CTE measurement with the thickness of 8 μm and the suspending space of 5 μm. 45
Figure 32. The variation of CTE at 300℃ in different film thickness and various current densities changing from 5 to 20 mA/cm2. 45
Figure 33. Measurement results of (a) hardness and (b) Young's modulus in different thickness with current densities changing from 5 to 20 mA/cm^2. 46
Figure 34. The fabricated nickel strain sensor with the thickness of 7.6 μm and the used current density of 20 mA/cm^2. 47
Figure 35. The determined residual strain (a) in different thickness with constant current density of 10 mA/cm^2 (b) in different current density with thickness of 7.6~8.4μm. 47
Figure 36. TEM images with plane view of the nickel films at different current densities and thicknesses, which are (a) 5 mA/cm^2 and 3.6 μm (Ni-4), (b) 15 mA/cm^2 and 3.9 μm (Ni-3), and (c) 5 mA/cm^2 and 16.8 μm (Ni-5), respectively. 48
Figure 37. TEM images with cross section view of electroplated nickel film; the dark field images show different grain size in top and bottom regions. 49
Figure 38. Fabrication process of metal-based VCD by electroforming; (a) electroform Cu; (b) define the electroplating molds; (c) electroform Ni and Cu in turn; (d) remove the molds; (e) electroform Cu; (f) electroform Ni

for upper fingers; (g) electroform Ni for springs; (h) release. 52
Figure 39. There is a angle of comb finger fabricated by the photoresist with un-vertical sidewall. By (a) positive photoresist and (b) negative photoresist. 53
Figure 40. Positive photoresist created by (a) front side and (b) backside exposure. 54
Figure 41. Metal-based VCD fabrication process by the backside exposure method; (a) electroform Cu; (b) removal of 1st seed layer; (c) backside exposure; (d) deposit 2nd seed layer; (e) electroform Ni and Cu in turn; (f) remove photoresist; (g) electroform Cu; (h) electroform Ni for upper fingers; (i) electroform Ni for springs; (j) release. 55
Figure 42. The fabrication methods of slope sidewall photoresist. The negative photoresist is used here. (a) the proximity method (b) inclined exposure (c) multiple shifted exposure. 57
Figure 43. The designed dimensions for fabricating the metal-based VCD by the modified fabrication process. (unit: μm). 59
Figure 44. SEM photographs of positive photoresist AZP4620® after backside exposure; (a) overview and (b) closed view of the molds. 59
Figure 45. SEM photographs of positive photoresist AZ9260® after backside exposure; (a) overview and (b) closed view of the molds. 59
Figure 46. Optical microscope pictures of fabrication results: (a) the 2nd seed layer of Ni/Cr deposited on the phtoresist and substrate, (b) after electroforming nickel to form the lower fingers and anchors, and (c) after removing photoresist. 60
Figure 47. Optical microscope pictures of the fabricated metal-based VCD; the process is completed except final release; (a) top of moveable fingers, (b) anchor and torsion spring, and (c) mirror plate. 61
Figure 48. SEM photographs of fabricated metal-based VCD by AZP4620® with tooth shaped lower fingers; (a) upper and lower fingers, (b) closed view, (c) schematic illustration of tooth shape formation, (d) narrow trench with remaining holes, and (e) wide trench without remaining holes. 62
Figure 49. SEM photographs of fabricated metal-based VCD by AZ9260®; (a) upper and lower fingers, (b) closed view, and (c) closed view in another angle. Thickness of 3rd sacrificial layer is about 2–3 μm here.................................... 63
Figure 50. SEM photographs of the fabricated metal-based VCD with the increased thickness of 3rd sacrificial copper layer; (a) thickness of copper layer about 4–6 μm, and (b) thickness of copper layer about 6–8 μm. 64
Figure 51. The electroplated copper concentrates on top of the lower fingers when thickness of 3rd sacrificial layer is increased; (a) the desired uniform deposition of copper layer; (b) the deposition results of copper layer due to

electric line concentration and ion delivery problem. 64
Figure 52. Experimental results of SU-8 structures with thickness of 60–62 μm, and the proximity gaps are (a) 0 μm, (b) 100 μm, (c) 200 μm, and (d) 300 μm, respectively. 65
Figure 53. Experimental results of SU-8 structures with thickness about 55 μm, exposure proximity of 300 μm, and the exposure times are (a) 3 sec, (b) 5 sec, (c) 8 sec, and (d) 12 sec, respectively. 66
Figure 54. Experimental results of multiple shifted exposure; (a) sample 1, (b) sample 2, and (d) sample 3 the photoresist thickness is about 62–65 μm, and the proximity gap is 70 μm; 67
Figure 55. Experimental results of the improved method; original proximity exposure with gaps of (a) 0 μm, (b) 300 μm, and (c) 500 μm; (d)–(f) the proximity exposure with z-axis shifting. 68
Figure 56. Process flow on AA cross-section to fabricate the metal-based VCD through multi-level photoresist mold; (a) deposit thick metal film; (b) deposit thin metal film; (c) deposit seed layer; (d) electroform nickel posts; (e) coating thick photoresist; (f) front side multiple exposure with the glass wafer; (g) deposit 2nd seed layer; (h) electroform nickel structures; (i) release. 75
Figure 57. Process flow on AA cross-section to fabricate the metal-based VCD through the patterned seed layer; (a)–(b) pattern the seed layer; (c) construct the electroplating molds; (d) electroform nickel as the lower fingers (e) electroform copper and nickel in turn as the sacrificial layer and upper fingers; (f) remove molds; (g) electroform nickel as the anchors; (h) release. 77

Chapter 1 Introduction

1.1 Background and Motivation

As a well known component, the electrostatic comb drive has rapidly occupied an important position in microelectromechanical system (MEMS) technology since the first report by Tang *et al.* [1]. With typically two sets of comb fingers, comb drive provides good linearity on output force and capacitive sensing over a considerable displacement range because of constant gap between stationary fingers and movable fingers during operation. Therefore, comb drive has been widely investigated, such as optimal shape design [2] and sub-micron gap comb drive [3], and employed for MEMS applications, such as filter [4], accelerometer [5], gyroscope [6], and optical switch [7].

In addition to operating in in-plane direction, comb drive has also been fabricated with two sets of fingers owning a vertical offset to cause out-of-plane motion, which is called vertical comb drive (VCD). Comparing to the parallel plate electrostatic actuator, the VCD ideally generates steady force over its entire stroke under one applied voltage, and exhibits no pull-in effect. Therefore, the VCDs are very suitable for applications requiring large out-of-plane displacement, low driving voltage, low power consumption, and high operation speed. For these superior characteristics, lots of investigations on the VCDs have been reported in recent decade [8-19]. In these literatures, the fabrication methods could be divided into two categories. The first category fabricated two sets of fingers owing a natural offset, such as SUMMiT-V process through defining two polysilicon layers [8], polysilicon refilled to fabricate the moving fingers and followed by bulk etching [9], deep reactive ion etching (DRIE) to form the upper and lower fingers and followed by bonding method [10], SOI-based (silicon on insulator) technique combining the DRIE etching [11-13], multiple DRIE etching on single-crystal silicon substrate [14]

and the micromachining on (111) single-crystal silicon substrate [15-16]. The second category used the deforming mechanism to elevate or degrade one set of comb fingers to create the required initial offset, such as bending beam caused by residual stress to degrade the stationary fingers [17], photoresist reflowing [18] or residual stress [19] to elevate the moving fingers, and permanent deformation by high temperature annealing to cause the initial offset [20]. All these above mentioned methods used single crystal silicon or polysilicon as structural materials. Most of them are limited in specific wafer, such as SOI or (111) wafer, and the DRIE process is usually the only one way to create comb structures. Thus, these silicon-based methods inherently produce a high production cost.

In contrast to the silicon-based materials, the polymer has become another attractive material in the MEMS technology recently because of their relatively low cost and much easier processing. For example, the polycarbonate (PC) and polymethylmetacrylate (PMMA) have been utilized to fabricate the high aspect ratio microstructures by hot embossing method for MEMS applications [21]. The micro fluidic devices for micro total analysis systems (μ–TAS) applications were also widely fabricated by PMMA, PC, polypropylene (PP), and polydimethylsiloxane (PDMS), etc. [22-24]. In addition to the passive components, the active micro devices have also been demonstrated by polymer materials to lower the cost, such as the electrostatic comb drive constructed by PMMA via the hot embossing technique [25], or by the thick negative photoresist SU-8 [26]. The accelerometer has also been fabricated by using SU-8 as the structural material [27], and the polymer micromechanical devices coated by metal layer via the electroless deposition technique have also been demonstrated [28]. Therefore, polymer is becoming a greatly important low cost alternative to their silicon or glass-based counterparts. However, no VCD made of polymer material has been reported yet.

With full development on LIGA-like process [29], which typically comprises the molds produced by thick photoresist and the metals deposited by electroplating, lots of

MEMS devices were fabricated by electroplated metals, such as switches [30], micro motors [31], electro-thermal actuators [32], accelerometers [33-34], inductors [35], and so on. This metal-based micromachining technique attracts lots of attentions due to its promising advantages including simple process, low cost, low temperature, low material resistivity, easy achievement on thick structure, and easy access of equipment. Especially, the low temperature process provides a good opportunity on integrating MEMS devices with integrated circuit (IC) into single chip for high efficiency system. Comparing to silicon-based materials which needs the doping process to lower resistivity, the superior electrical conductivity of metal structures can remarkably simplify the fabrication process, enhance the handling power and lower the power consumption of micro devices. Furthermore, the great conductivity also exhibits a good potential to fabricate radio frequency (RF) components with high quality factor [36]. Additionally, thick structural layer, i.e. several hundreds μm, which is difficultly deposited by silicon-based process, can be easily achieved by electroforming technique, which is a low cost and easy access process, and improves the device performance. Therefore, with the outstanding characteristics mentioned above, metal-based micromachining has become one of the mainstream fabrication approaches in micro system technology. Also, no investigation on fabricating the metal-based VCD with LIGA-like process has been reported yet.

In this dissertation, novel approaches to fabricate the polymer and metal-based VCDs are proposed, which provide a flexible and low cost solution on fabricating VCD for MEMS applications.

1.2 Contributions

Here, instead of using silicon-based materials, novel approaches are proposed to fabricate the low cost VCDs in different materials—polymer and metal. For the polymer-based VCD, without any additional sacrificial layer, the proposed double-side

multiple partial exposure (DoMPE) method, which has been developed for extending the multi-level morphology on both the front and back sides of the suspended photoresist microstructures, is applied to the positive thick photoresist AZ9260® to carve out the suspending upper fingers and the fixed lower fingers. The front-side partial exposure defines the height of the fixed lower fingers, and the back-side partial exposure creates the suspending space of the upper fingers. Process parameters, including exposure dosage, development time, development depth, soft-bake conditions, and the Ti film thickness as gray-tone mask, have been experimentally characterized. With the proper overhang design to realize the electrical isolation, the metal layer deposited on the structural surface by sputtering provides a suitable electrical conductivity. This approach provides a simple, flexible, and low cost solution to fabricate VCDs.

For the metal-based VCD, only LIGA-like process is used here. Nickel and copper are electroformed in turn with thick photoresist AZ9260® as electroplating molds to form the VCD structure and the sacrificial layer, respectively, in which the trench refilled by nickel fabricates the moving fingers, and the electroformed copper layer works as the sacrificial layer and provides the operation space. With removing the sacrificial copper layer by wet chemical etching, the VCD made of electroformed nickel is released finally. This approach also provides a low cost process for fabricating VCDs, and is IC-compatible by providing a low temperature solution without destroying the underlying materials, i.e. typically the silicon-based materials.

1.3 Dissertation Outline

The goal of this dissertation is to develop novel approaches for fabricating the polymer and metal-based VCDs. The detailed investigations including theoretical analyses, fabrication methods, experimental results, and characterizations are described in the following chapters.

In Chapter 2, the operation principle of VCD, including the theoretical analysis and FEM simulation, are discussed first.

In Chapter 3, the DoMPE process is proposed to enhance the complexity of suspended 3D photoresist microstructures. The related parameters are experimentally characterized, and different complex 3D photoresist microstructures made of AZ9260® are successfully fabricated to demonstrate the enhancement effect.

In Chapter 4, the polymer-based VCD made of photoresist AZ9260® is fabricated through the developed DoMPE process. With a metal film deposited on the structure surface by sputtering for the electrical conductivity, the polymer-based VCD is driven successfully. By comparing the analytical and experimental results, the feasibility of polymer-based VCD is verified, which also demonstrates one application of DoMPE process on active devices.

In Chapter 5, the properties of electroplated nickel, such as Young's modulus, hardness, and coefficient of thermal expansion (CTE), are experimentally investigated with different thicknesses and different current densities.

In Chapter 6, the fabrication method of metal-based VCD is described in detailed, where the backside exposure with photoresist AZ9260® is utilized to create the desired electroplating molds, and the experimental and fabrication results are discussed. Additionally, methods to fabricate the slope photoresist are also investigated.

Finally, Chapter 7 concludes this dissertation and suggests some future research directions. Two simpler fabrication methods of metal-based VCDs are also suggested.

Chapter 2 Operation Principle

For the dimensional design, the operation model of VCD is established here. The theoretical analyses are carried out with solving the force balance equation, which comprises the electrostatic force induced by the comb fingers and the mechanical force generated by the torsion springs, to determine the static response under a driving voltage, where the relationship of capacitance versus displacement is extracted by FEM simulation and twelfth-order polynomial curve fitting.

2.1 VCD with Torsional Motion

As the schematic illustration shown in figure 1, the VCD demonstrated in this dissertation can be simply expressed as two sets of comb fingers. One set of fingers, called the stationary fingers (or the lower fingers, here), is fixed on the substrate and the other set of fingers (or the upper fingers, here), called the movable fingers, is suspended and connected to the suspending plate which is supported by the anchors through the torsion springs. With the voltage applied between the upper and lower fingers, the VCD

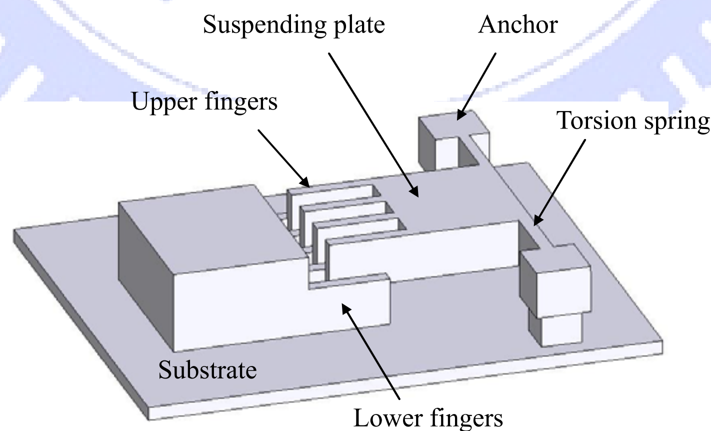

Figure 1. The schematic illustration of the vertical comb drive.

can be driven into torsional motion by the electrostatic force until it is balanced by mechanical force of the torsion springs. Therefore, by solving the force balance equation, the relationship of driving voltage and torsion angle can be determined.

2.2 Electrostatic Force

In general, the electrostatic force generated by the comb drive with n finger pairs is given by [9]

$$F_e(z) = \frac{n}{2}\frac{dC}{dz}V^2 \quad (1)$$

where C is the capacitance between two sets of fingers, z is the vertical displacement in the out-of-plane direction, and V is the applied voltage. However, the capacitance C could not be considered as a simple parallel plate assumption with the fringing fields due to the limited height (or thickness) of fingers. To characterize the dC/dz relationship accurately, the finite element method (FEM) through software ANSYS is used to simulate the capacitance of single pair fingers at different displacements z. Then, these simulated data are curve fitted by twelfth-order polynomial to obtain the capacitance C as a function of displacement z, which is expressed as [9,19]

$$C(z) = a_{12}z^{12} + a_{11}z^{11} + a_{10}z^{10} + \cdots + a_2 z^2 + a_1 z + a_0 \quad (2)$$

Therefore, the function of electrostatic force of VCD could be obtained.

As illustrated in figure 2(a), in addition to the case without the bottom plate, the condition of lower fingers with bottom plate is also analyzed. Figure 2(b) shows one example of the simulation and fitting results with the finger height of 35 μm, the finger width of 14 μm, and the gap of 4 μm. The fitting curve agrees well with the simulation data. For the fingers with bottom plate, the capacitance is similar to that without bottom plate at initial 2/3 stroke, but quite different in the final part of stroke.

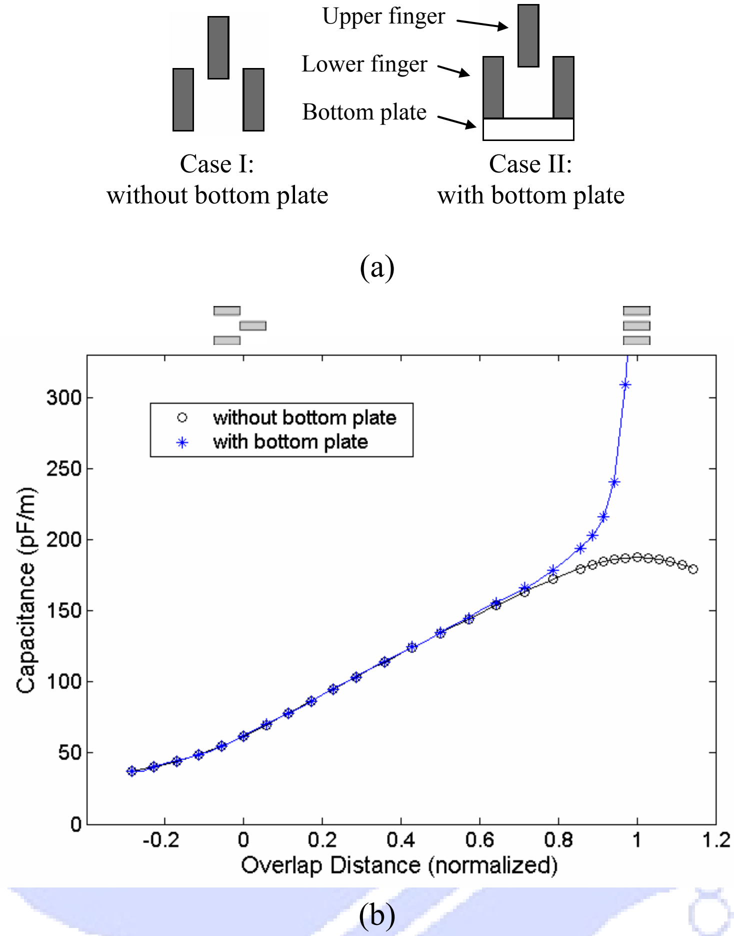

Figure 2. The simulated cases and results; (a) two simulated cases: with/without the bottom plate; (b) the simulated capacitance of single pair fingers at different displacement, z, and the curve fitting results; the overlap distance is normalized by the finger height of 35 μm.

2.3 Force Balance Analysis

Under a driving voltage, the torque induced by electrostatic force is equal to the torque generated by the torsion springs at equilibrium. Thus, the torsion angle could be determined by this force balance analysis. Figure 3 shows side view of the upper finger and torsion plate of the VCD, and the torque T_e induced by electrostatic force of VCD could be expressed as

$$T_e = \int_{x1}^{x2} F_e(z) L_r dx \quad (3)$$

where $x1$ and $x2$ indicate the overlap region of the upper and lower fingers along the

suspending plate (x direction), and L_r is the moment arm of the electrostatic force $F_e(z)$ about the torsional axis and is equal to $x\cos\theta$, in which θ is rotation angle of the VCD. Because the vertical displacement z could be expressed as $x\sin\theta$, equation (3) could be re-written as following by including equation (1) and (2)

$$T_e(\theta) = \frac{nV^2\cos\theta}{2}\left[\sum_{k=1}^{12}\frac{k\left(a_k x^{k+1}\sin^{k-1}\theta\right)}{k+1}\right]_{x1}^{x2} \tag{4}$$

Equation (4) describes the torque induced by the electrostatic force under different rotation angle for a given voltage. In addition, the torque generated by the mechanical

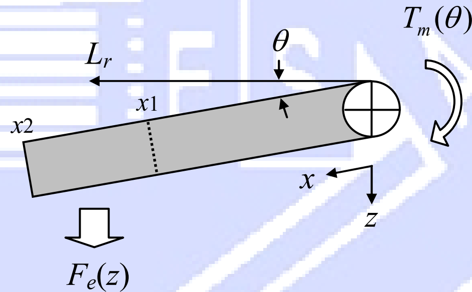

Figure 3. The illustration of the torque induced by electrostatic force from side view of the upper finger and suspending plate, where $T_m(\theta)$ is the induced torque by the mechanical force of the torsion springs

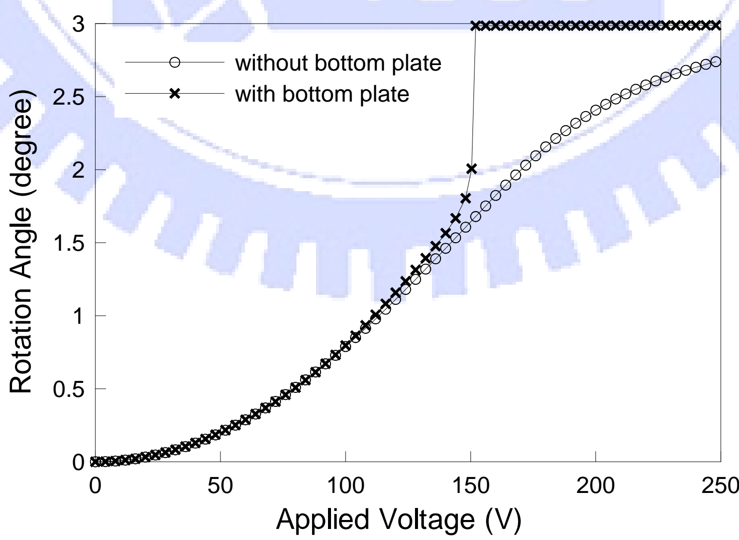

Figure 4. The calculated results of the static deflection of vertical comb drive including the cases with or without the bottom plate

Table 1. The parameters used for the theoretical analysis

Symbol	Value	Symbol	Value
n	11	a_3	(855.38)/(68.52)[§]
$x1$	400 μm	a_4	(-3.15e7)/(3.45e8)[§]
$x2$	480 μm	a_5	(-1.43e13)/(1.56e12)[§]
b	15 μm	a_6	(8.38e17)/(-3.22e18)[§]
h	35 μm	a_7	(2.30e22)/(-7.44e22)[§]
L	90 μm	a_8	(-2.42e27)/(1.80e28)[§]
G	407.9 MPa*	a_9	(1.20e31)/(2.84e32)[§]
a_0	(1.03e-10)/(1.04e-41)[§]	a_{10}	(1.97e36)/(-4.46e37)[§]
a_1	(4.16e-6)/(4.18e-6)[§]	a_{11}	(-4.31e40)/(-3.00e41)[§]
a_2	(-6.98e-3)/(-1.72e-2)[§]	a_{12}	(2.70e44)/(4.02e46)[§]

* G is obtained by $G = E/[2(1+\nu)]$. As described in section 4.3, the effective elastic modulus of 1.142 GPa and Poisson's ratio of 0.4 are used.

[§] Value of (case without bottom plate)/(case with bottom plate).

force of the torsion springs could be described by

$$T_m(\theta) = \frac{G\theta\left(b^3h + bh^3\right)}{6L} \tag{5}$$

where G is the shear modulus of elasticity; b, h and L are the width, height and length of the torsion springs, respectively. Therefore, by equations (4) and (5), the rotation angle of VCD could be found.

Here, the software Matlab is used to calculate the numerical solutions. Figure 4 shows the calculated results with the relative polynomial coefficients and structural dimensions listed in table 1. The initial overlap of two sets of fingers is 10 μm, and the finger height, finger width, and the gap between fingers are the same as that used in figure 2. For the case without bottom plate, the rotation angle increases faster in the first half stroke but much slower in the second half stroke with the increasing voltage. For the case with bottom plate, a similar behavior is observed in the first half stroke but there is a pull-in effect for the rotation angle approximating to 2 degree due to the sudden increase of the capacitance which induces the rapid rise of electrostatic force.

2.4 Effect of Angled Fingers

As described in literature [2], the finger shape of comb drive will affect the delivered output force. By changing the gap profile, the output force versus displacement exhibits different profiles. Generally, the VCD fabricated by recent proposed methods [8-19] has a constant gap between the stationary and movable fingers, thus the driving force ideally keeps constant during most of its operation range with a given voltage. By the novel metal-based VCD fabrication method proposed in this dissertation, the comb fingers with different angles can be fabricated through the construction of sloped photoresist (the detail is described in Chapter 6). Therefore, different output force profiles of VCD can be expressed by controlling the angles of comb fingers. In order to characterize the effect of angled fingers, the static responses of VCDs with different finger angles are analyzed by

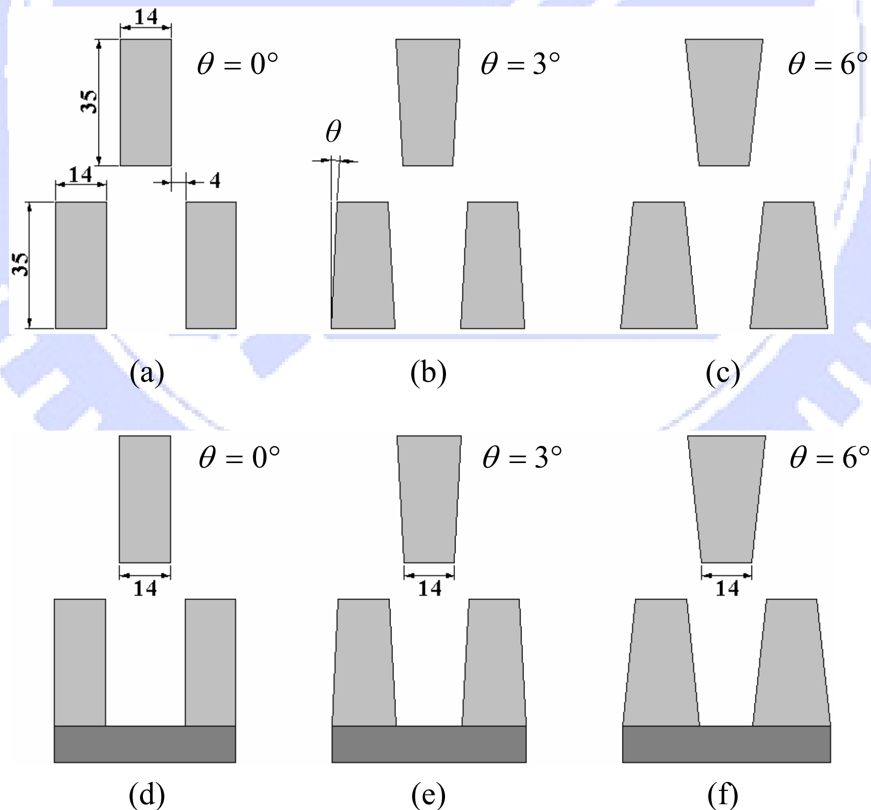

Figure 5. Six cases of VCD are analyzed and discussed; (a) $\theta = 0°$, (b) $\theta = 3°$, (c) $\theta = 6°$, (d) $\theta = 0°$ with bottom plate, (e) $\theta = 3°$ with bottom plate, (f) $\theta = 6°$ with bottom plate. (unit: μm)

the same analysis method discussed in above sections, and both the fingers with and without bottom plate are also discussed. As shown in Figure 5, six cases are performed here. Figures 5(a) and 5(d) show the VCDs with constant gap, which refers to zero angle ($\theta = 0°$), and the other VCDs have the fingers with angles of 3° (figures 5(b) and 5(e)) or 6° (figures 5(c) and 5(f)). The related dimensions for this analysis are labeled in Figure 5(a), which are the same as that used in Figure 2.

For the VCDs without bottom plate (cases of figures 5(a-c)), figure 6 shows the simulation results of capacitance under different overlap distances by FEM method. The curve fittings are also performed by twelfth-order polynomials. The simulation results show that the increasing angle of finger provides the increasing capacitance, especially for the large overlap distance. This increment on capacitance will enhance the output force of VCD and lower the driving voltage. Figure 7 shows the simulation and fitting results for the fingers with bottom plate (cases of figures 5(d-f)). A similar enhancement is also observed—increasing finger angle provides increasing capacitance when the opposite

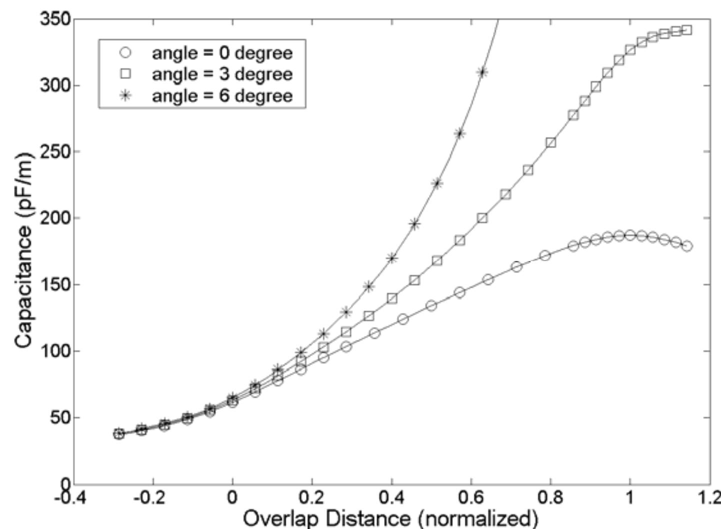

Figure 6. VCDs without bottom plates; capacitances under different overlap distances are simulated and curve-fitted with finger angles of 0º, 3º, and 6º; the overlap distance is normalized by the finger height of 35 μm.

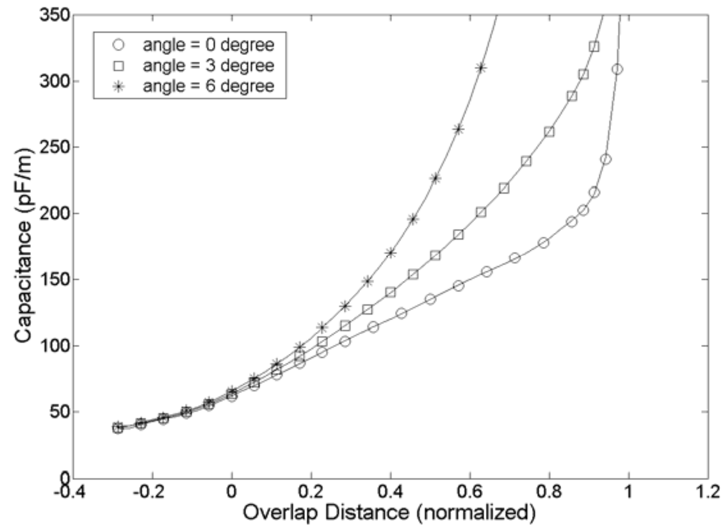

Figure 7. VCDs with bottom plates; capacitances under different overlap distances are simulated and curve-fitted with finger angles of 0º, 3º, and 6º; the overlap distance is normalized by the finger height of 35 μm.

fingers are closing. Furthermore, the static responses of VCDs with angled fingers are also calculated. With the same structural dimensions listed in table 1, figures 8(a) and 8(b) show the calculated results of VCDs without and with bottom plates, respectively. For the VCDs without bottom plates (figure 8(a)), the driving voltage is obviously lowered with the increasing finger angle. Additionally, for the VCD with finger angle of 6 degree, a pull-in phenomenon is also observed. The remarkable increase of capacitance in later half stroke induces the large rise of electrostatic force. For the VCDs with bottom plates (figure 8(b)), a similar enhancement on output force is also observed. The driving voltage is remarkably lowered with the increase of finger angle.

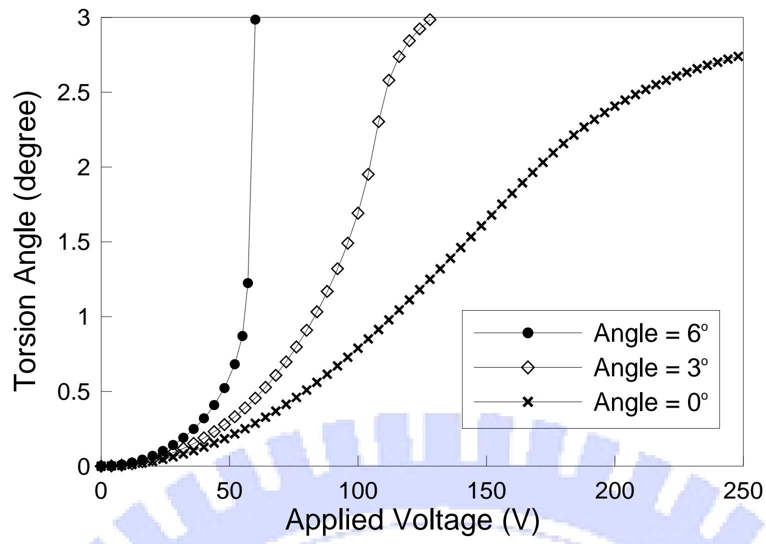

(a)

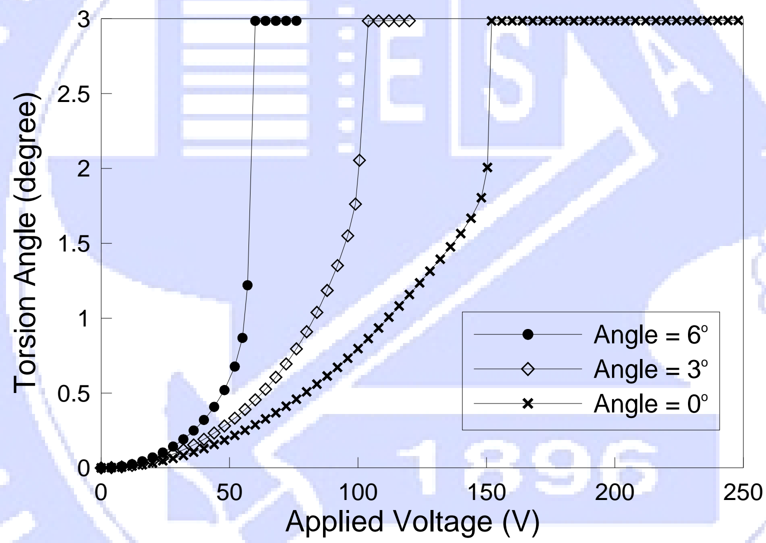

(b)

Figure 8. The calculated static responses of VCDs (a) without and (b) with bottom plates; the finger angles include 0º, 3º, and 6º.

Chapter 3 Double-Side Multiple Partial Exposure (DoMPE)

Fabrication technologies on batch process of IC promote the rapid development of MEMS. Recently, three dimensional (3D) microstructures have proved helpful in applications such as photonics [37], chemical sensors [38], data storage [39], tissue engineering [40], micro fluidic systems [41-43], and micro electronic devices [26-27,44-45]. To date, different approaches have been developed for constructing true 3D microstructures. Beyond the standard lithography technology, the microstereolithography process [46] and two-photon absorption (TPA) polymerization [39,47-49], which are based on light-induced polymerization in photopolymerizable resin, have been proposed to create the 3D structures in arbitrary shapes. However, both approaches lack batch fabrication ability, which must be supported by the introduction of micro transfer molding (μTM) for replicating master structures [50]. Another technique, called multibeam interference lithography (MBIL) [37,51], is a method for constructing 3D microstructures with highly parallel processing; however, only spatially periodic structures can be obtained using this technique. Even though microstereolithography, TPA and MBIL provide specific approaches to construct true 3D or periodic microstructures, unlike the standard lithography, limited equipment availability always restricts their practical applications. Therefore, owning to the advantage of easy access to equipment compatible with IC standard lithography, expanding the fabrication capability of standard lithography technology to 3D microstructures still attracts considerable attention—even the IC fabrication scheme is basically a planar technology.

For the standard lithography technique, the development of thick photoresist technology makes fabricating the 3D microstructures increasingly feasible. First, the high aspect-ratio structures achieved by LIGA or LIGA-like processes, which are often

considered 2.5D techniques, enhance the performance of micro components [29]. By using the inclined and rotated UV lithography, the oblique or curved microstructures, which have been called the 3D microstructures, can be constructed with the negative photoresist SU-8 for the applications of micro channels, filters, mixers [41] and optical mirrors [52]. However, the complexity of 3D microstructures is still quite limited when using either approach. Another important technique, which reportedly defines the photoresist in flexible shape, is the gray-tone lithography that changes the UV-light transmission through the mask, thereby modulating the exposure intensity on the substrate front side [53-56]. To generate the suspending microstructures, the backside partial exposure scheme with glass substrate has been utilized to suspend photoresist microstructures, such as cantilevers and bridges [42], without additional sacrificial material. However, the suspending space was restricted to one level because the backside dosage could only be controlled by the exposure time.

Based on standard lithography equipment, this study presents a novel batch process called the double-side multiple partial exposure (DoMPE) method, which enhances the complexity of suspended 3D photoresist microstructures by incorporating a gray-tone mask on the backside exposure. Here, the gray-tone mask is realized by controlling the thickness of the metal film [56]. The mergence of the gray-tone mask on the backside produces the possibility of carrying out partial exposure on the substrate front and back sides, the photoresist can then be carved out to form increasingly complex 3D microstructures. In this study, microstructures with up to four levels on the front and back sides generated via the DoMPE process are presented to demonstrate the enhancement effect when constructing complex 3D microstructures made of positive photoresist AZ9260®.

3.1 Procedure of DoMPE Method

To remove various thicknesses of positive photoresist on the front and back sides, multi-patterning on the front side and gray-tone lithography on backside are used to achieve the dosage control in each exposure step to generate a desired depth. When these exposure steps are complete, the development solution finally removes the exposed photoresist to obtain free standing 3D photoresist microstructures without using a sacrificial layer and an additional release step. The proposed DoMPE method comprises front-side multiple partial exposure and back-side multiple partial exposure, and requires only standard IC-compatible equipment, such as a spin coater, mask aligner, and PVD system. Process steps for fabricating multi-level microstructures are described as follows.

3.1.1 Suspended front-side multi-level microstructures

Figure 9 illustrates three examples of fabricating suspended photoresist microstructures with various levels on front side through the double-side partial exposure techniques. A glass substrate is used for backside exposure. The front-side partial exposure can utilize a standard front-side mask (figure 9(a)), where the photoresist is partially exposed to define the groove. In figure 9(b), partial exposure on backside is realized through a patterned metal layer, which is previously deposited on the glass substrate as a back-side mask to create a suspending space. Groove depth, d, and suspending space, S, are mainly controlled by exposure dosage. When standard masks are used during front-side partial exposure, multi-patterning can be implemented easily in the front direction by only changing masks with the dosage control; this process is called front-side multiple partial exposure. Via this method, a suspended photoresist cantilever with multiple levels on the front side can be fabricated after final development without an additional release step (figure 9(c)).

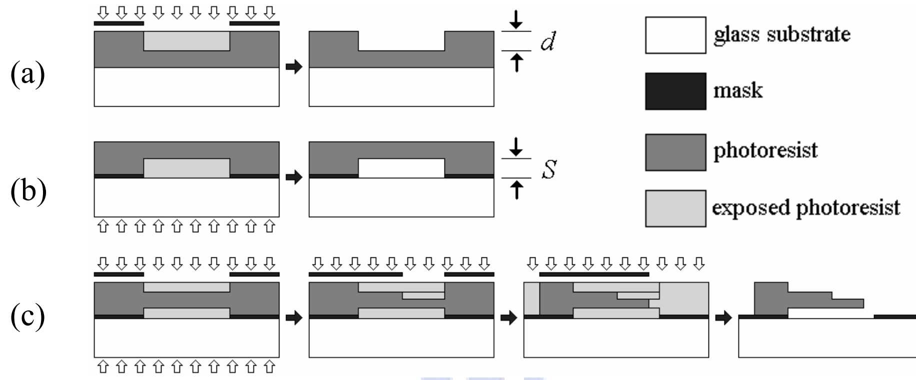

Figure 9. Fabrication of photoresist microstructures with multiple levels on front side; (a) the grove with a depth of *d* created by front-side partial exposure; (b) the suspending bridge with a space of *S* created by backside partial exposure; (c) the suspended cantilever with three levels on the front side by front-side multiple partial exposure.

3.1.2 Suspended back-side multi-level microstructures

To generate multiple levels on the backside of microstructures, a proposed back-side gray-tone mask is utilized, since it is difficult to place and switch the mask for multi-patterning the backside through the glass wafer in a standard aligner with precise line width control. The gray-tone mask is achieved by depositing various thicknesses of metal film on the glass substrate to modulate light transmitted through the glass wafer for back-side multiple partial exposure. Figure 10 presents the fabrication process of a photoresist cantilever with multiple levels on the backside via backside multiple partial exposure. First, a thicker metal film is deposited and patterned by lift-off process as the opaque back-side mask (figure 10(a)). A thinner metal film is subsequently defined at the desired locations also by sputtering as the gray-tone back-side mask for modulating backside exposure dosage (figure 10(b)). Then, the thick positive photoresist is spin-coated and soft-baked (figure 10(c)). After re-hydration, back-side multiple partial exposure is carried out by one exposure (figure 10(d)), in which the photoresist on backside is exposed with different dosages due to the gray-tone mask to create different

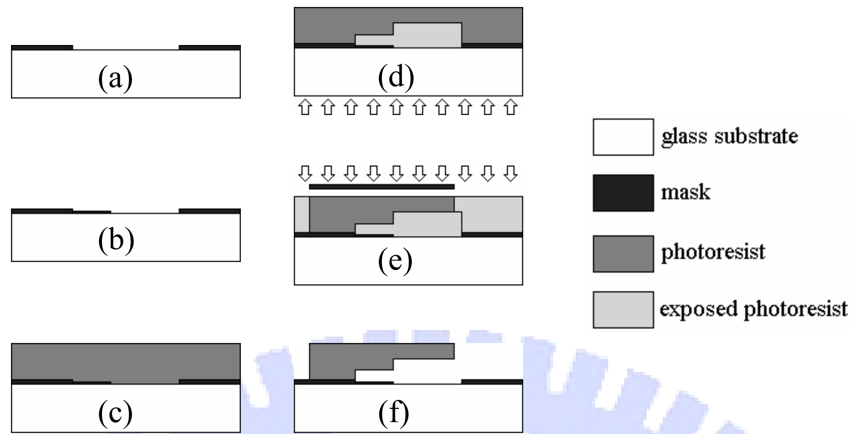

Figure 10. Fabrication process of 3D photoresist microstructure with multiple levels on the backside; (a) defining the thick metal film as backside opaque mask; (b) defining the thin metal film as backside gray-tone mask; (c) coating thick positive photoresist; (d) completing backside multiple partial exposure by one exposure; (e) front-side full exposure to define the overall area of structure; (f) development and release.

exposure depths. Subsequently, front-side exposure on proper area is applied to define overall shape of the microstructures (figure 10(e)). At last, a cantilever with multiple levels on backside can be obtained after final development (figure 10(f)).

By combining multiple partial exposures on the front and back sides, more complex 3D microstructures can be achieved using the proposed DoMPE method. For example, when three front side levels are employed (level 0, 1 and 2)—where level 0 indicates zero dosage—without the backside gray-tone mask, i.e., two different metal film thicknesses (figure 11(a)), one partial exposure can produce two levels in the backside direction; thus, six combinations of microstructures can be fabricated. By using the back-side gray-tone mask (figure 11(b)), three different metal film thicknesses can generate three levels on the backside. Thus, there are nine combinations. Expanding the multi-level fabrication capability on the back or front sides directly enhances the complexity of 3D microstructures.

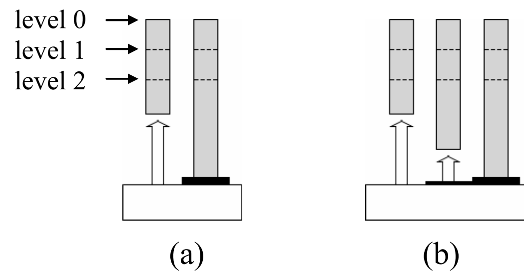

Figure 11. Possible combinations of microstructures fabricated by the DoMPE process with three levels on the front side; (a) six combinations due to two levels on the backside; (b) nine combinations due to three levels on the backside.

3.2 Photoresist Processing Parameters

The commercially available positive thick photoresist (AZ9260®, Clariant) is used here. First, the photoresist with a thickness of 58 μm is spin-coated and then soft-baked at 90°C. After re-hydration for over 30 minutes, the photoresist is exposed to different dosages. Then, different development times are applied using an AZ-400K developer diluted at a ratio of 1:4 with de-ionized water. Figure 12 shows the experimental results for development depths at development times of 5, 10, 20 and 30 minutes and exposure dosages of 66, 131, 262 and 394 mJ/cm^2, respectively, where the photoresist is soft-baked for 15, 60 and 90 minutes, respectively. Development depths are normalized using the overall photoresist thickness of 58 μm. According to experimental results shown in figure 12(a), where soft-bake time is 15 minutes, a large exposure dosage or extended development time increases development depth. Furthermore, the comparison of development depths in figure 12(a) to figure 12(c) clearly indicates that soft-bake time also plays an important role in this process. A longer soft-bake time increases stability and decreases development depth under different development times, especially at the high partial exposure dosages. When the soft-bake time is increased to 90 minutes, as shown in figure 12(c), the development depth is further decreased, especially for the development

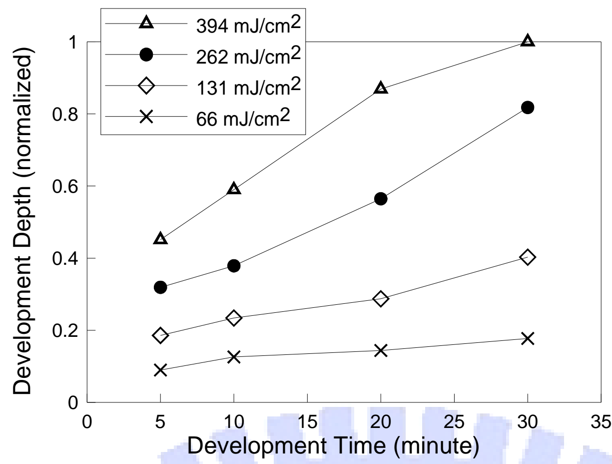

(a)

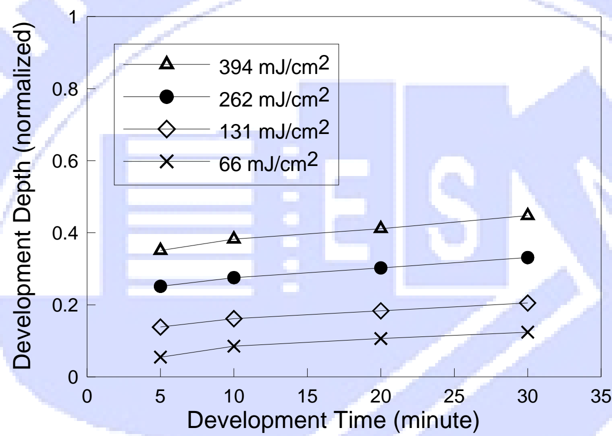

(b)

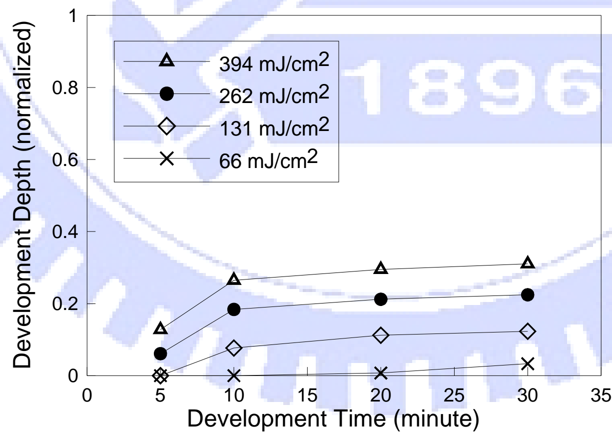

(c)

Figure 12. Development depth under different development times and exposure dosages. Photoresist AZ9260® is soft-baked at 90°C for (a) 15 minutes, (b) 60 minutes, and (c) 90 minutes.

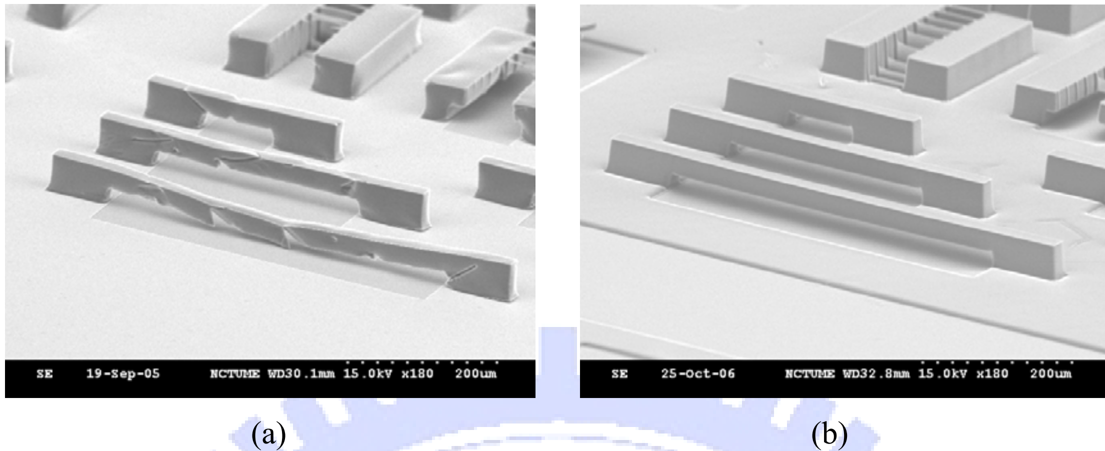

(a) (b)

Figure 13. Bridges made of photoresist AZ9260® with soft-bake time of (a) 40 minutes (b) 90 minutes.

time of 5 minutes, indicating that the photoresist needs at least 10 minutes to reach the stable region. For the development time over 20 minutes, a soft-bake of 90 minutes generates a consistent development depth, which is suitable for processes needing long development times. In addition to improved photoresist development, a long soft bake is also helpful for reliable fabrication of 3D photoresist microstructures. Figure 13(a) and 13(b) show fabrication results for photoresist bridges with soft-bake times of 40 minutes and 90 minutes, respectively. The bridge collapses down after release due to insufficient soft-bake time, and the structure stands well on the substrate with sufficient soft-bake time.

A gentle vibration to refresh the developer above the photoresist during the development may affect development depth, especially with short soft-bake times. Figure 14 shows the influence of vibration on the development depth under two soft-bake conditions with different development times, where the solid symbol indicates the development with gentle vibration while the hollow symbol presents the results obtained without any vibration. Experimental results show that the vibration markedly enlarges the development depth when soft-baked for 15 minutes, especially under long development times. For a soft bake of 90 minutes, the influence of gentle vibration on development

depth is not obvious when development time exceeds 20 minutes. Figure 15 shows the detailed relationship between development depth and exposure dosage under soft-bake time of 90 minutes and development time of 45 minutes without the gentle vibration, where development depths are normalized by overall photoresist thickness of 58 μm. Experimental results indicate a stable but not quite linear increase to development depth by increasing exposure dosage.

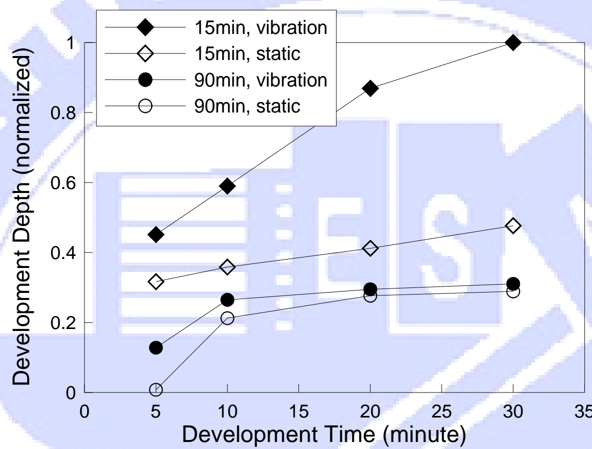

Figure 14. Development depth at different development times with or without gentle vibration at two soft-bake times, where the exposure dosage is 394 mJ/cm^2 and the development depths are normalized by overall photoresist thickness of 58 μm.

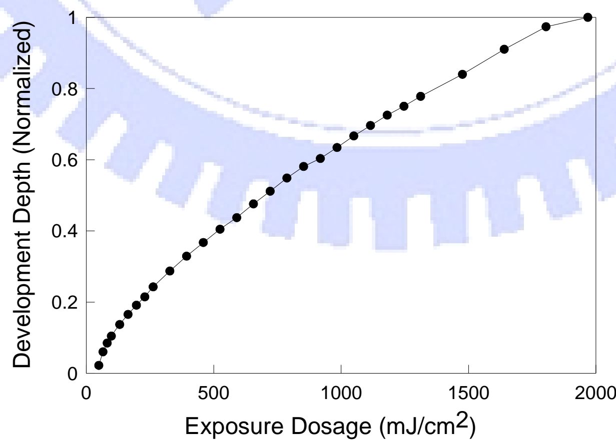

Figure 15. Relationship between development depth and exposure dosage for photoresist AZ9260® at soft-bake time of 90 minutes and development time of 45 minutes.

3.3 Gray-tone Mask

To achieve back-side multiple partial exposure, the modulation capability of the gray-tone mask realized by different thicknesses of metal film must be characterized. In this work, an opaque mask and gray-tone mask for backside multi partial exposure are both formed by Ti film deposited by a sputtering system. With different thicknesses of Ti film deposited on the glass substrate, the transmittance of Ti film is measured by a radiometer with a spectral response of 310–515 nm and peak response of 405 nm. Experimental results show (figure 16) that a thicker Ti film reduces transmittance. For example, Ti film

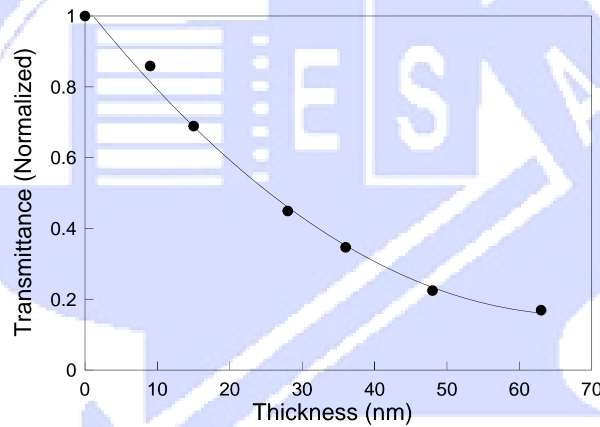

Figure 16. The measured UV-light transmittance at different Ti film thicknesses.

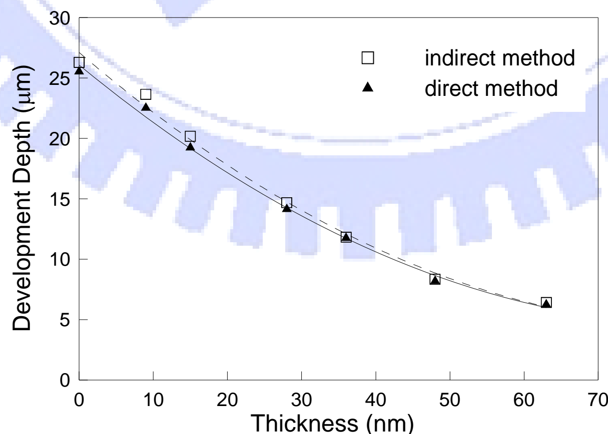

Figure 17. Verification on the development depth versus Ti thickness with a photoresist of 58 μm that is soft-baked for 90 minutes and developed for 45 minutes. Line with square symbol is obtained by calculating data in figures 15 and 16. Line with triangle symbol is obtained by direct measurements.

with thicknesses of 15 nm and 63 nm provide about 68.9% and 16.9% UV-light transmittance, respectively, where transmittance is normalized by the measured exposure intensity of 34.1 mW/cm^2 under the glass substrate without Ti deposition. Therefore, based on experimental data, the dosage distribution in the back-side multi partial exposure can be designed to fabricate various desired suspending gaps when Ti thickness is properly controlled. Figure 17 shows experimental verification of development depth under different Ti thicknesses with an exposure dosage of 616 mJ/cm^2, where the square symbol indicates calculated depth using experimental data (figures 15 and 16), and the triangle symbol indicates direct measurement results under different Ti thicknesses. Experimental results show that the dosage modulation of Ti film characterized by the radiometer agrees well with direct measurement results.

3.4 Results of 3D Photoresist Microstructures

After establishing the process parameters, different 3D microstructures made of AZ9260® are fabricated and presented to demonstrate the effectiveness of the proposed DoMPE process. The photoresist with a thickness of approximately 60 μm is spin-coated and soft-baked at 90°C for 90 minutes. Figure 18 shows the structures with only two levels on the backside. For only one level on the front side, the meander (figure 18(a)) and coil (figure 18(b)) with the line width of 30 μm is fabricated and suspended 19 μm from the substrate with a back-side exposure dosage of 407 mJ/cm^2. By introducing two front dosages, the suspending channels have a depth of 20 μm (figures 18(c)−(d)), in which two levels exist on both the front and back sides.

Figures 19 and 20 show the microstructures fabricated by double-side multiple partial exposure, where the gray-tone mask creates three levels on the backside. With two levels on the front side, figure 19 shows a microinductor (figure 19(a)), a round 3D structure (figure 19(b)), a square 3D structure (figure 19(c)), and a mini castle (figure 19(d)) with

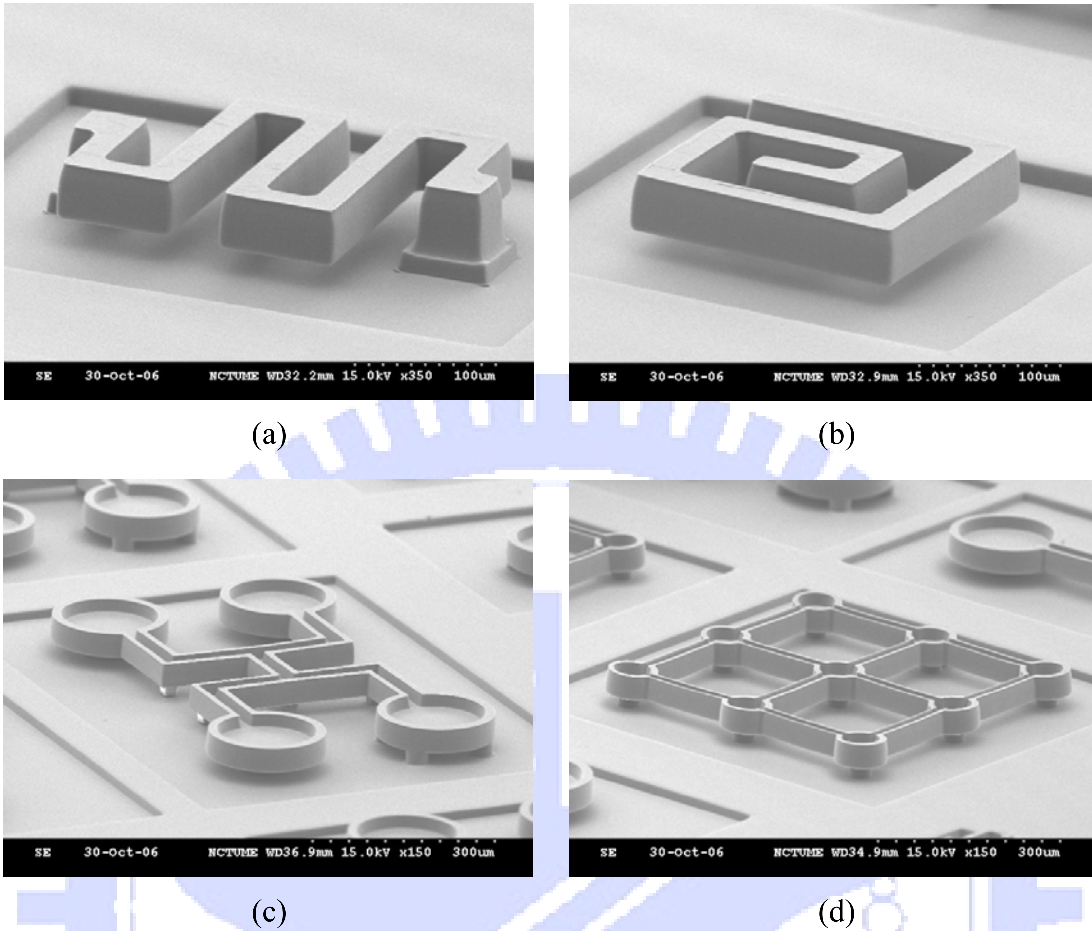

Figure 18. 3D microstructures made of photoresist AZ9260® with two levels on the backside; the suspending (a) meander line and (b) coil with one level on the front side; (c)−(d) micro channels with two levels on the front side.

different suspending gaps, respectively. Figure 20 shows the cantilevers (figure 20(a)−(b)) and bridges (figure 20(c)−(d)) with uneven thicknesses and three levels constructed on both the front and back sides. Increased thickness variation on the gray-tone mask can provide additional levels on the backside. With an opaque mask formed by a Ti thickness of 160 nm and a gray scale formed by Ti thicknesses of 0 mm, 28nm and 48nm, Figures 21(a) and 21(b) show the fabricated cantilevers and bridges with four levels on both front-side and back-side directions. The 3D microstructure complexity is successfully enhanced by incorporating gray-tone lithography on backside exposure. These photoresist 3D microstructures are useful for enhancing the complexity of 3D molds

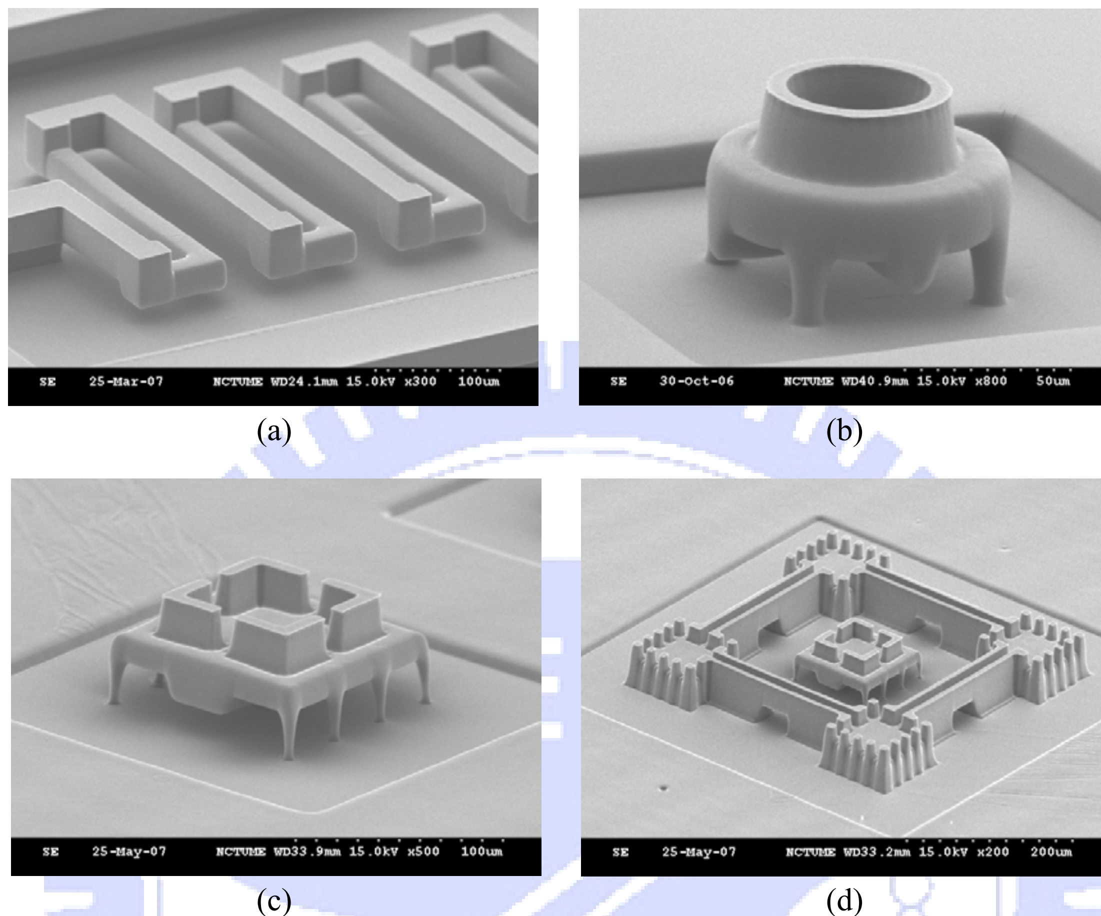

Figure 19. 3D microstructures made of photoresist AZ9260® with three levels on the backside and two levels on the front side; (a) microinductor, (b) microstructure with round shape, (c) microstructure with square shape, and (d) mini castle.

on forming 3D micro channels with polydimethylsiloxane (PDMS) [42], or providing channel cross sections with increased flexibility while directly fabricating micro fluidic components, such as embedded channels, filters, and mixers [41,43].

Moreover, by incorporating metallization schemes, such as electroless [44] and physical vapor [26,27,45] depositions, polymer-based 3D microstructures have been demonstrated to extend to be electrical-conductive devices, such as microinductors [44], electro-thermal actuators [45], accelerometers [27], and comb drives [26]. Here, for example, with metallization by physical vapor deposition, a 3D microinductor by the DoMPE process is fabricated (figure 19(a)) instead of using the conventional

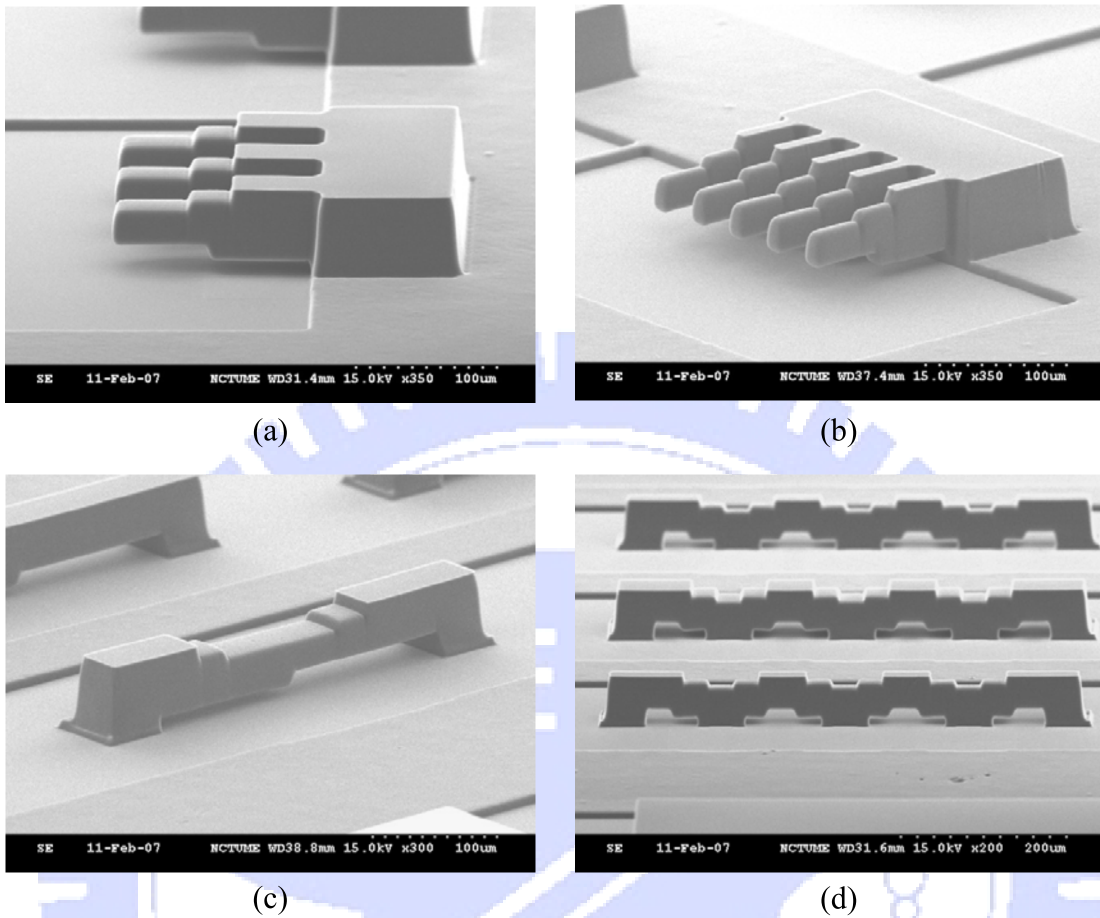

Figure 20. 3D microstructures made of photoresist AZ9260® with three levels on both the front and back sides; (a)–(b) cantilevers, and (c)–(d) bridges.

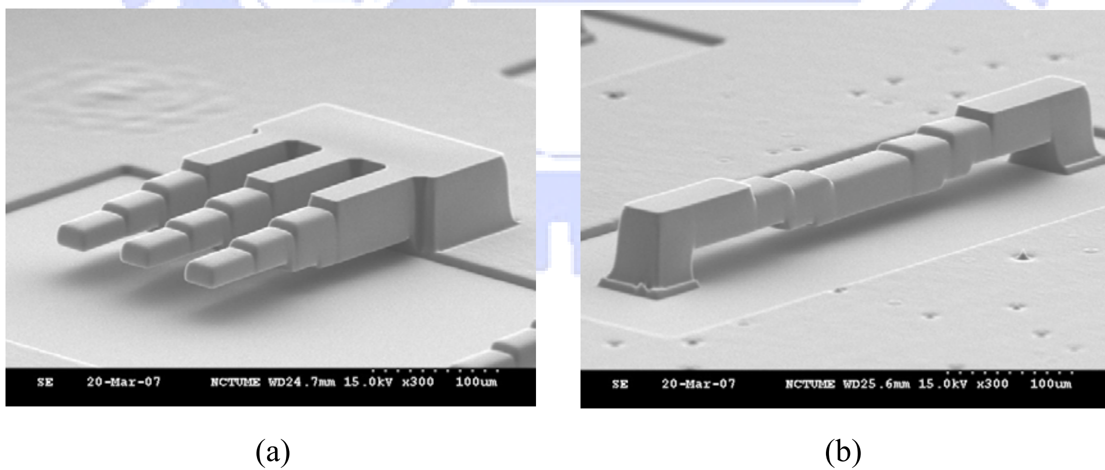

Figure 21. 3D microstructures made of photoresist AZ9260® by the DoMPE process with four levels on both the front and back sides; (a) cantilevers, (b) bridge.

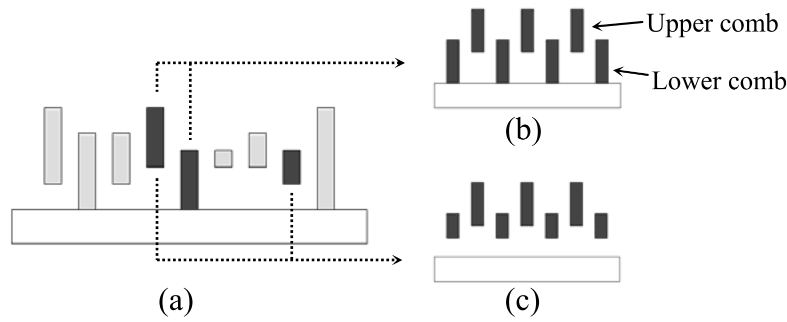

Figure 22. Different beam structures can be fabricated with three levels on both the front and back sides for constructing vertical comb drives with different strokes by the DoMPE process; (a) 9 various beam structures; (b) type I vertical comb structure design with fixed lower comb fingers; (c) type II vertical comb structure design with suspended lower comb fingers.

layer-by-layer method. An electrostatic actuated vertical comb drive can also be realized with the DoMPE process by fabricating two staggering sets of fingers. Figure 22(a) illustrates structures that can be fabricated using the DoMPE process with three levels on both the front and back sides. By selecting different pairs of structures, VCDs with different strokes can be constructed. Figures 22(b) and 22(c) show VCD with the fixed lower fingers and VCD with the suspended lower fingers, respectively. A metal layer finally deposited on the structural surfaces by sputtering can provide the desired electrical conductivity for these vertical comb drive structures to act as active devices.

3.5 Summary

Using standard lithography equipment, the proposed DoMPE process enhances the complexity of suspended 3D photoresist microstructures by incorporating back-side gray-tone lithography and a partial exposure technique. Process parameters, including exposing dosage, development time, development depth, soft-bake conditions, and the Ti film thickness as gray-tone mask, have been characterized experimentally. Experimental

results indicate that soft-bake time plays a significant role in the DoMPE process, and affects development depth and fabrication stability. By increasing the thickness variation on the gray-tone mask, complexity of 3D microstructures can be further enhanced. The DoMPE process can act as a basic platform that provides an affordable solution to construct flexible features in three dimensions for MEMS applications.

Chapter 4 Polymer-Based Vertical Comb Drive

As described in Chapter 3, by the DoMPE process, two sets of comb fingers owning the initial vertical offset can be directly constructed, which composes the vertical comb drive (VCD) to perform the out-of-plane motion. Here, the DoMPE process with two levels in both front and back sides is employed and totally needs only three masks.

4.1 Fabrication Process

Figure 23 shows the detailed fabrication procedure of the proposed polymer VCD. The soda-lime glass is used as the substrate, and the commercial positive thick photoresist, AZ9260® (Clariant), is utilized to demonstrate this process. First, the Ti layer of 2500 Å is deposited and patterned by the lift-off process as the mask for the backside partial exposure, as shown in figure 23(a). Then, the photoresist AZ9260® with thickness about 55 μm is spin-coated and soft-baked at 90℃ for 90 minutes, as shown in figure 23(b). After re-hydration, the photoresist is exposed by the front-side partial exposure for the desired development depths, as shown in figure 23(c), which defines the height, i.e. thickness, of the lower fingers. Then, the backside partial exposure is carried out for the suspending space of the upper fingers, as shown in figure 23(d), which provides the desired operation stroke of VCD. Subsequently, the full exposure is carried out to define the overall structure, as shown in figure 23(e), in which the upper and lower fingers are self-aligned to avoid the misalignment problem. After all the required exposing procedure, the final development is performed with the developer of AZ400k (20% diluted by de-ionized water). At this step, the release process of VCD is also completed without any additional sacrificial layer and etching step. Then, the structure of VCD is fabricated, as shown in figure 23(f). Furthermore, in order to provide the desired electric conductivity to activate the VCD, a thin Cu layer with thickness of 2000 Å is deposited on

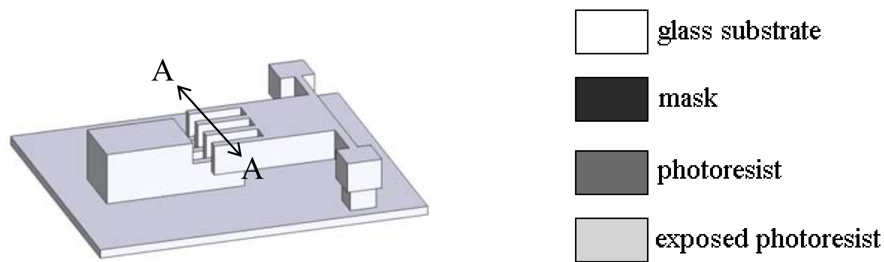

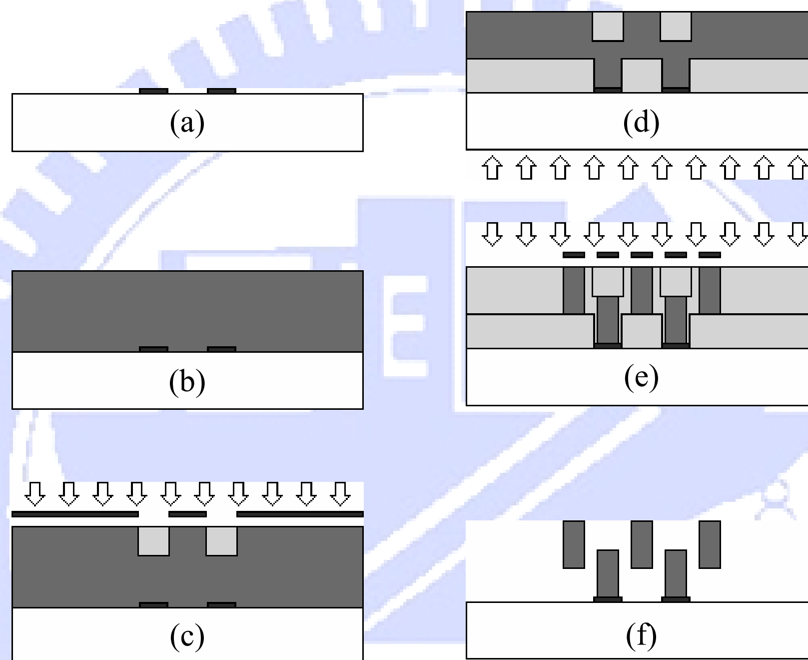

Figure 23. The fabrication process of the polymer VCD on the AA cross-section; (a) defining the Ti film as the backside mask; (b) coating the thick positive photoresist; (c) the front-side partial exposure; (d) the backside partial exposure; (e) the full exposure to define the overall structure; (f) development and release.

the structural surface by sputtering system. In addition, to achieve a locally electric isolation to avoid the electric short between the upper and lower sets of fingers, the overhang design at the anchors of suspending structures is employed. The backside masks under the anchors are defined as a smaller size, so the overhang structures are created after the development.

As described in Chapter 3, the development depth of photoresist is mainly controlled by the exposure dosage. In other words, the larger dosage creates the deeper depth. Additionally, other processing parameters of photoresist, such as the development time and soft-bake time, also play important roles in this process. Therefore, a proper set of parameters is needed to obtain the stable fabrication results. Here, the photoresist thickness about 55 μm, the soft-bake time of 90 minutes and the development time of 45 minutes are employed on the fabrication of polymer VCDs. Depending on the experimental data shown in figure 15, the desired suspending space of upper fingers and the height of lower fingers could be fabricated by using the corresponding dosages.

4.2 Fabrication Results

With photoresist processing conditions described above, the polymer VCDs with two levels both in front and back sides are fabricated by the DoMPE process. Figure 24(a) shows the fabricated VCD made of AZ9260® after the final deposition of Cu by sputtering, where the size of suspending plate is 300×360 μm, and the width and length of torsion springs are 12 μm and 60 μm, respectively. The introduced partial exposure dosage of 426 mJ/cm^2 creates the development depth about 20 μm in the front-side direction, which results in the height of lower fingers about 35 μm. By the introduced partial exposure dosage of 525 mJ/cm^2 in the backside direction, the suspending space of upper fingers about 24 μm is obtained, which induces the thickness of suspended structures about 31 μm. Figures 24(b) and 24(c) show the closed view and top view of the finger structures, respectively. Finally, the torsion springs near the set of upper fingers are removed by the manual probe locally with the tip diameter about 10 μm for the following measurement.

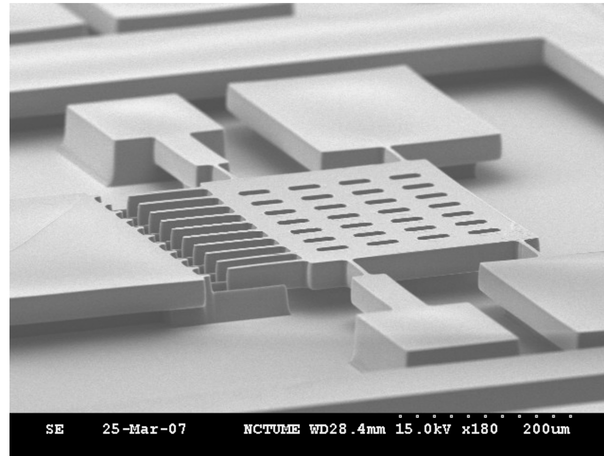

(a)

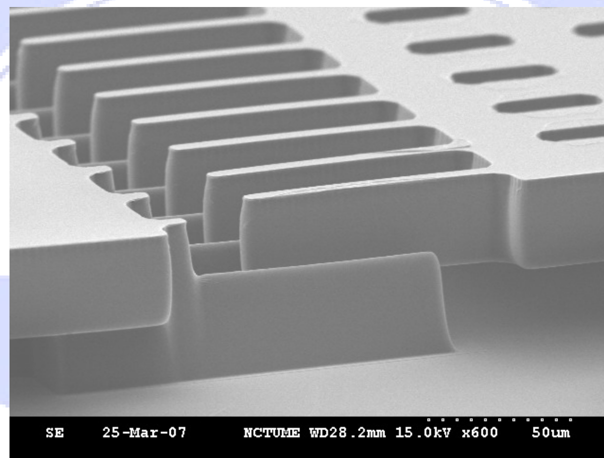

(b)

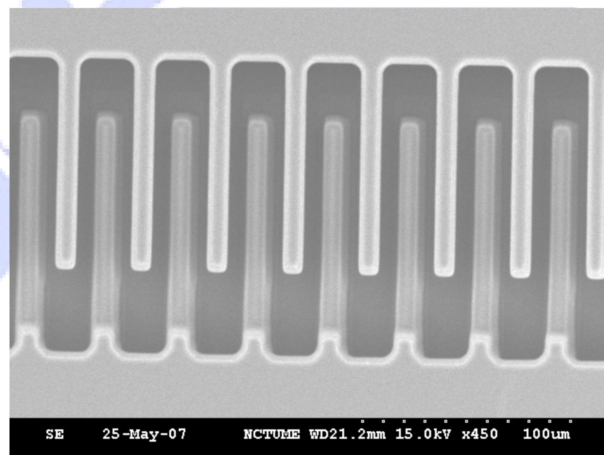

(c)

Figure 24. The fabricated polymer vertical comb drive by DoMPE process; (a) the over view of VCD; (b) the closed view and (c) top view of the finger structures.

4.3 Characterization and Discussions

The static deflection and dynamic response of the polymer VCD are measured by the white light interferometer and the MEMS motion analyzer, respectively. According to the measurement on static deflection, the maximum rotation angle of 2.31° can be achieved by the driving voltage of 158.3V with the same dimensions shown in figure 24. Figure 25 shows the measured results of dynamic response, where the VCD is activated by a sinusoid wave with amplitude of 20V and offset of 20V, and the first mode natural frequency of 6.6 kHz is obtained. With this characterized natural frequency, the elastic modulus could be found by further determining the density of photoresist. Here, a simple experiment is performed to obtain the density of AZ9260®. The photoresist is spin-coated on a wafer with the calibrated weight, and then patterned into a circle with a specified diameter. By determining the increase of total weight and the final thickness of photoresist film, the density of photoresist could be obtained through the characterized value of weight over volume. Then, with the determined density of 1180±7 Kg/m^3 and first natural frequency of 6.6 kHz, the effective elastic modulus of 1.142 GPa is used in the FEM simulation, where the Poisson's ratio is assumed as 0.4. Figure 26 shows the simulated results of modal analysis, in which the model of the VCD includes the suspending plate, the torsion springs, and the upper fingers. The second, third, and fourth natural frequencies are also found as 41.40 kHz, 44.10 kHz, and 54.02 kHz, respectively.

With the above material properties, the static deflection of polymer VCD is calculated by the software Matlab through the analytical model described in Chapter 2. Figure 27 shows the experimental and analytical results of the polymer VCD, where the latter includes the cases with and without the bottom plate. In the analytical results, the case without bottom plate presents a more linear behavior but a little lower rotation angle under different driving voltages. For the case with bottom plate, a similar behavior is observed in the first half stroke but there is a pull-in effect for the rotation angle of 2.17°

with the applied voltage of 167.37V due to the obvious increase of the capacitance which induces the rapid rise of electrostatic force. By comparing to experimental results, where a snapping phenomenon is also observed between the voltages of 158.3V and 161.8V, the bottom plate effect has an evident influence on the performance of VCD, especially at high driving voltage.

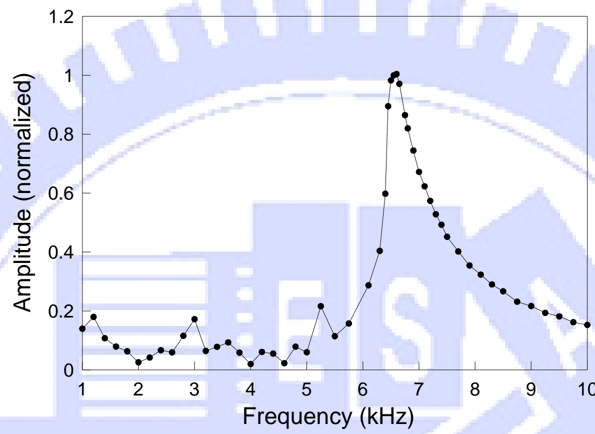

Figure 25. The dynamic response of vertical comb drive; the peak response is obtained at 6.6 kHz.

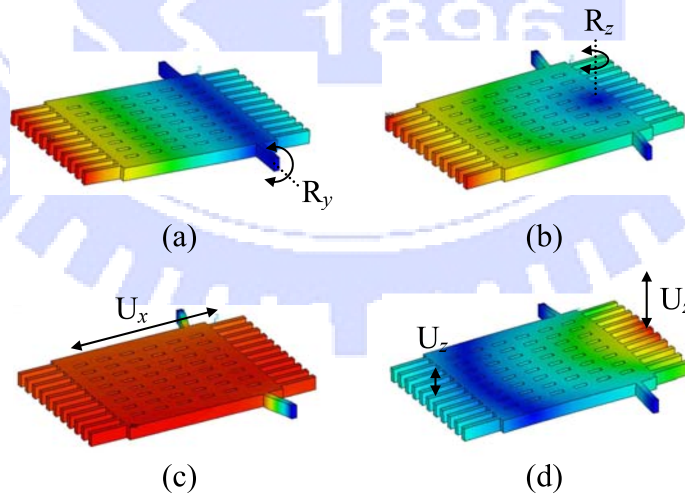

Figure 26. The mode shapes and natural frequencies of the vertical comb drive; (a) f_1=6.60 kHz, (b) f_2=41.40 kHz, (c) f_3=44.10 kHz, and (d) f_4=54.02 kHz.

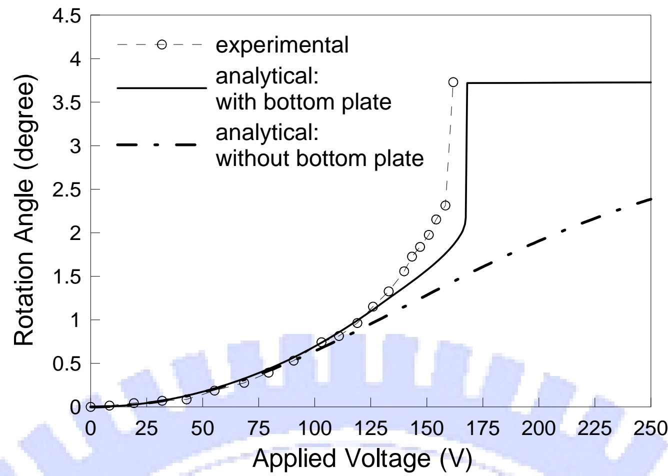

Figure 27. The experimental and analytical results of the static deflection of vertical comb drive, where the analytical results include the cases with and without bottom plate.

4.4 Summary

This investigation proposes a reliable approach to fabricate the polymer-based vertical comb drive by using the positive thick photoresist AZ9260® as the structural material. A double-side multi partial exposure (DoMPE) method is employed to create the suspending upper fingers and the fixed lower fingers without any additional sacrificial layer and etching process. The proper processing parameters of photoresist for the fabrication of polymer VCDs have been established. For the activation of the polymer VCDs, the metal layer deposited on the structural surface by the sputtering system provides the desired electric conductivity while the overhang design realizes the electric isolation. According to the measurement results, the rotation angle of 2.31° can be achieved by the driving voltage of 158.3V, which agrees with the analytical results and verifies the feasibility of the proposed approach to fabricate the polymer VCDs.

Chapter 5 Property Characterization of Electroplated Nickel

The electroplated nickel is one of the typical metals utilized in micro electromechanical systems (MEMS) for its low electrical resistance, low process temperature, and wide thickness range from several μm to hundreds of μm [29,31-32]. The mechanical properties of materials used in micro component will affect the performance of the device directly. Therefore, the accurate values on material properties become important for MEMS designers to obtain the predictable performance on the designed micro components. For the past decade, the properties of electroplated nickel, including the microstructure, micro texture, Young's modulus, yield strength, ultimate tensile strength, and hardness, have been studied extensively [57-62]. The effects due to different electroplating solutions were reported [59] and the influences due to different electrodepositing conditions were also studied. It was found that, differing from the traditional bulk nickel, the mechanical properties of electroplated nickel are strongly influenced by the deposition conditions. The increasing of electrodepositing current density would reduce the hardness, Young's modulus, and tensile strength [60]. Also, the dramatic deterioration of strength was observed after annealing [59,61], or at high temperature environment [62].

The coefficient of thermal expansion (CTE) is another important mechanical property for MEMS devices, especially for electro-thermal microactuators. Qian *et al.* reported that the CTE of the nanocrystalline copper increased with the increase of the microstrain [63]. Furthermore, it was found that the permanent strain would enhance the CTE of the graphite [64], and the residual stress in the sputtered thin film was suggested to act as an important mechanism to influence the CTE [65]. However, only few literatures have investigated the CTE on electroplated nickel. Dini and Johnson characterized CTEs of

Table 2. Summary of recent investigations on electroplated nickel; several materials, such as Au, Ti, and Al, are also included.

Reference	[58]	[61]	[60]	[62]	[69]	[59]	[70]	[66]	[71]	[72]	[65]	[73]	[74]
Year	1997	2001	2002	2003	2003	2003	2004	1975	2001	2005	2000	2003	2005
Materials	Ni	Ni	Ni	Ni	Ni	Ni Ni-Co Ni-Fe	Ni Ni-Fe	Ni	Ni	Ni	Ti Al	Au	Au
Process	EP	PE	EP	EP	EP	EP	EP	EP	EP	EP	PVD	PVD	EP
Elastic modulus	●	●	●	●	●	●	●		●			●	●
Yield stress	●	●	●	●	●	●						●	
Ultimate stress	●	●	●	●	●	●							
Hardness	●		●				●						
Creep				●									
Fatigue				●						●			
Micro structure	●	●	●	●	●	●				●			●
Orientation		●											
Texture/XRD			●		●								
Fracture behavior					●					●			
CTE								●	●		●		
Residual stress											●		●
Residual strain									●				
Stress gradient													●
Current density			●				●						●
Testing Temp.				●				●	●				
Anneal		●				●							
KD of Electrolyte						●							
Width of sample				●								●	
THK of sample			●		●						●	●	

P.S. EP, KD, and THK indicate 'electroplating', 'kind', and 'thickness', respectively.

nickel electrodeposited from the sulfamate bath electrolyte [66], but no investigation about the influences by the deposition conditions and the dimension effect on electroplated nickel. Table 2 lists the summary of recent investigations on electroplated nickel, and some

investigations on gold, titanium, and aluminum deposited by physical vapor deposition (PVD) system or electroplating are also included for comparison.

In MEMS devices, the requirement of a structural thickness may depend on different applications. Therefore, the CTEs of electroplated nickel films by the LIGA-like process at different electroplating current densities and different film thicknesses around 10 μm are investigated here. Other properties, including the hardness, elastic modulus, and residual strain are also experimentally characterized. The measured results show the obvious variation when the thickness and current density are changed, and these experimental data are also useful for the design of metal-based VCDs.

5.1 Sample Preparation

In order to characterize the mechanical properties, including CTE, hardness, Young's modulus, and residual strain of electroplated nickel films, suspended cantilever beams and strain sensors with different thickness and electroplating current densities are fabricated.

The electroplating seed layer of Cu/Ti is first deposited on the silicon substrate by sputtering, and the electroplating molds are formed by novolak positive photoresist (AZP4620®, Clariant) for the desired structures. The nickel films are electroplated with thicknesses at 4, 8, 12 and 16 μm, respectively, using a commercially available nickelsulfamate solution, and the current density is set at 5, 10, 15 and 20 mA/cm^2, respectively. The composition of the electrolyte is listed in table 3. The operation temperature of electroplating is 50±1°C, and the pH of the electrolyte is kept in the range of 3.5~4.4. The thickness of electroplated nickel film is identified by 3D micro profile measurement instrument (ET4000, Kosaka) with the vertical resolution of 0.1 nm after the removal of electroplating molds by acetone.

The electroformed nickel cantilever beams of 1000 μm in length are fabricated for the measurement of mechanical properties. Figure 28 shows the fabrication process of the

cantilever beams. The photoresist AZP4620® with thickness of 5 μm is coated and defined as the sacrificial layer, as shown in figure 28(a), then the seed/adhesion layer of Cu/Ti with thickness of 1000Å/200Å is deposited by the sputtering. The second photoresist AZP4620® with thickness of 20 μm is formed as the electroplating mold, as shown in figure 28(b). After the electroforming of nickel to the desired thickness (figure 28(c)), the structures are released in acetone with ultrasonic agitation, and the nickel cantilever beams are fabricated, as shown in figure 28(d). With the same process flow, the strain sensor [67] is also fabricated for the characterization of the residual strain which is built in the nickel film during the electrodeposition.

Table 3. The composition of the electrolyte for nickel electroplating.

Composition	Quantity
Nickel Sulfamate, $Ni(SO_3NH_2)_2 \cdot 4H_2O$	400 g/L
Nickel Chloride, $NiCl_2 \cdot 6H_2O$	5 g/L
Boric Acid, H_3BO_3	40 g/L
EPC-30	10 ml/L
NPA	2 ml/L
Wetting Agent	5 ml/L

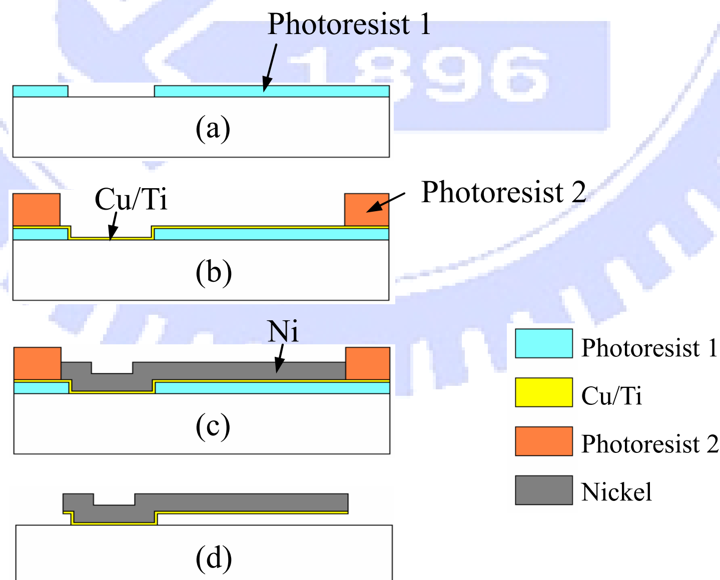

Figure 28. The fabrication process of the nickel cantilever beams made by electroforming, (a) photoresist 1 patterning for the sacrificial layer; (b) seed/adhesion layer sputtering and photoresist 2 patterning for the molds; (c) nickel electroplating; (d) release.

5.2 Measurements

The CTE is measured by an in-house CTE measurement apparatus illustrated in figure 29, and the hardness as well as Young's modulus is characterized by the nanoidentation system. The CTE of the electroplated nickel is determined by measuring the elongation of the nickel cantilevers directly. The sample is placed on the stage in the chamber with a transparent cover on top for observation with the optical microscope above. The chamber is heated by the heating coil and cooled by the water with temperature control through the thermal couple surrounding the sample stage. The heating rate in the chamber is 20°C/min. The elongation, ΔL, of the nickel cantilevers are determined by the optical microscope with the x-y stage, which provides the resolution of 0.5 μm in the planar direction. By measuring the elongations of nickel cantilever with the length of L at temperature increment of ΔT at steady states, the CTE of the electroplated nickel, α, can be obtained by the equation of $\alpha = \Delta L / L\Delta T$.

The hardness and Young's modulus of the electroplated nickel are measured by the nanoindentation system. From the load-displacement data, the Young's modulus E can be obtained by the following equations:

$$E^* = \frac{1}{2}\sqrt{\frac{\pi}{A}} \times \frac{\mathrm{d}P}{\mathrm{d}h} \tag{6}$$

$$\frac{1}{E^*} = \frac{1-\nu^2}{E} + \frac{1-\nu_i^2}{E_i} \tag{7}$$

where E^* is the reduced modulus, A is the projected area of elastic contact, $\mathrm{d}P/\mathrm{d}h$ is the stiffness at the as-unloading region of the load-displacement curve, and the ν_i and E_i are the Poisson's ratio and Young's modulus of the indenter [68], respectively. The Poisson's ratio of the specimen, ν, is 0.31 here, which is assumed to be the same as the traditional bulk nickel. The indentation is carried out by the three-sided pyramidal indenter (Berkovich) with the tip radius of 50 nm.

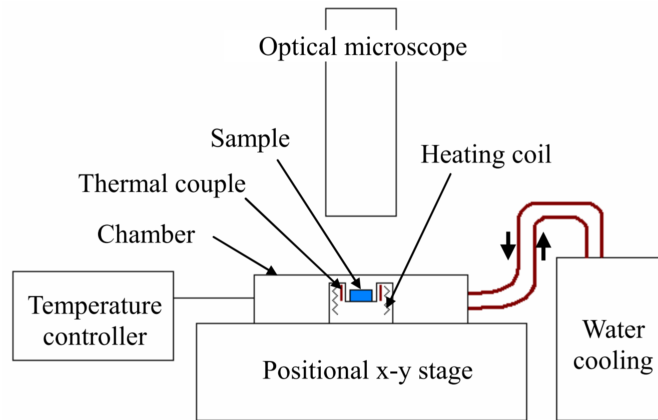

Figure 29. The experimental setup for the measurement of CTE.

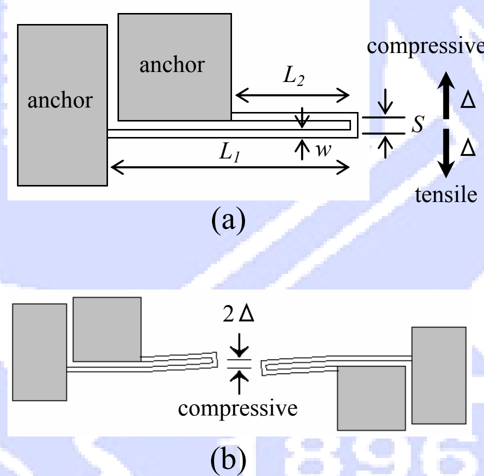

Figure 30. The strain sensor to determine the residual strain [14]. (a) Deflection directions with different strain types; (b) pair design to double the deflection.

The residual strain of the electroplated nickel is in situ determined by the strain sensor with a long-short beams design [67]. As shown in figure 30(a), the tip of the strain sensor deflects laterally due to the different elongation, in compressive stress, or the different contraction, in tensile stress, caused by the residual strain between the two beams. Then, the doubled deflection, 2Δ, of the tip is determined by the optical microscope with CCD camera through the arrangement of a pair of strain sensors shown in figure 30(b). By means of the equations of $\varepsilon = \gamma \cdot \Delta$ [67] and $\sigma = E\varepsilon$, where ε and σ are the residual

strain and stress respectively, γ is the geometrical factor described in reference [67], Δ is the displacement of the tip, and E is the Young's modulus, the residual strain and stress of the electroplated nickel can be obtained.

5.3 Results and Discussions

The nickel cantilevers with thicknesses of 4, 8, 12 and 16 μm are successfully fabricated. The actual thickness is found to be deviated within 0.7 μm. However, the CTE of cantilever at thickness of 4 μm can not be carried out due to serious warps. Figure 31 shows some samples of the fabricated nickel cantilevers at thickness of 8 μm with different length. Figure 32 shows the calibrated results of CTE at 300℃ in different film thickness with various electroplating current densities. The results indicate that CTE is elevated with the increasing thickness and electroplating current densities. For example, at the current density of 10 mA/cm^2, the CTE is increased from 9.9±1.8 (10^{-6}/℃) to 13.6±1.8 (10^{-6}/℃) when the thickness of nickel film increases from 8.2 μm to 15.9 μm, which is about 37.4% enhancement in CTE. For samples at the same thickness, for example at 12 μm, CTE is varied from 10.0±1.8 (10^{-6}/℃) to 16.6±1.8 (10^{-6}/℃) when the current density increases from 5 mA/cm^2 to 20 mA/cm^2, about 66% enhancement in CTE. This result reveals that the CTE of electroplated nickel is strongly affected by the electroplating current density.

The hardness and Young's modulus are measured at the anchor area of the cantilever by the nanoindentation system, and each specimen is calibrated eight times at different locations. Figure 33(a) and 33(b) show the measurement results of hardness and Young's modulus, respectively, which reveal a different trend with increasing thickness and current density. For the films at similar thickness, for example 7.5~8.2 μm, with different electroplated current densities from 5 mA/cm^2 to 20 mA/cm^2, the averaged hardness is

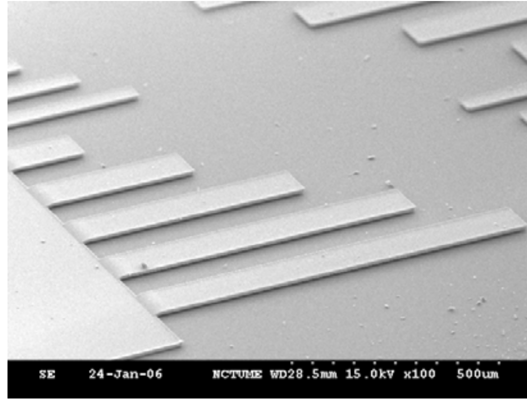

Figure 31. The SEM picture of the fabricated nickel cantilevers for the CTE measurement with the thickness of 8 μm and the suspending space of 5 μm.

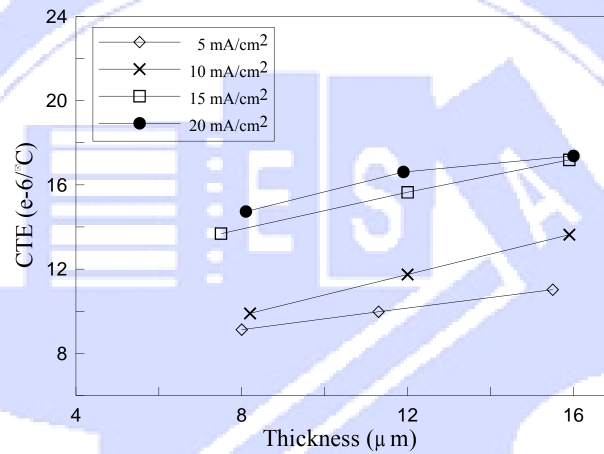

Figure 32. The variation of CTE at 300℃ in different film thickness and various current densities changing from 5 to 20 mA/cm2.

found to be decreased from 5.32 GPa to 4.58 GPa, and Young's modulus is reduced from 209.9 GPa to 197.0 GPa, which is consistent with the results reported by Fritz *et al.* [39] where a lower current density was shown to result in higher mechanical strength. For the commonly used current density of 10 mA/cm^2, the averaged hardness is found to be reduced from 5.29 GPa to 4.52 GPa, Young's modulus is decreased from 212.5 GPa to 191.0 GPa, when the thickness increases from 4.0 μm to 15.9 μm. Both properties show a falling trend with the increasing current density and film thickness.

The residual strains of the electroplated nickel at different thickness and current densities are also measured by means of the strain sensors. The length of the long-beam,

L_1, is 700 μm, the length of short-beam, L_2, is 300 μm, the beam width, w, is 10.5 μm, and the space, S, is 20 μm. Figure 34 shows the SEM pictures of the fabricated nickel strain sensor with the thickness of 7.6 μm. The measurement results of the residual strain are shown in Figure 35 with each point averaged by four strain sensors at least. The deflection direction of the tip of strain sensor indicates that electroplating conditions in this work induce a compressive residual strain in the nickel film. Figure 35(a) shows the residual strain at different thickness with the constant current density of 10 mA/cm^2. The

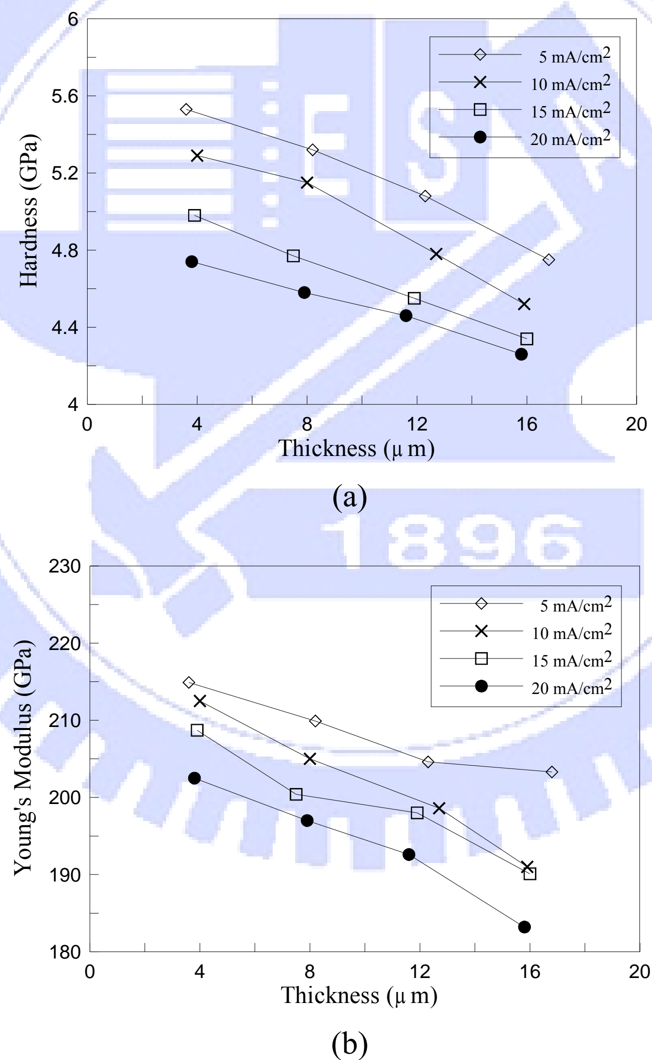

Figure 33. Measurement results of (a) hardness and (b) Young's modulus in different thickness with current densities changing from 5 to 20 mA/cm^2.

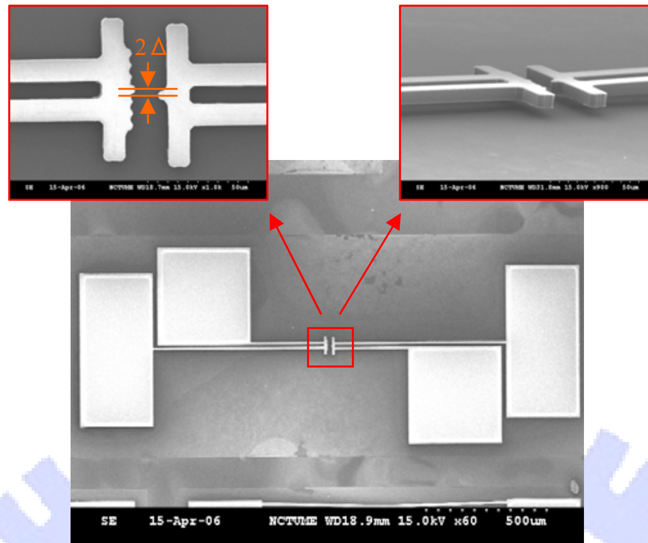

Figure 34. The fabricated nickel strain sensor with the thickness of 7.6 μm and the used current density of 20 mA/cm^2.

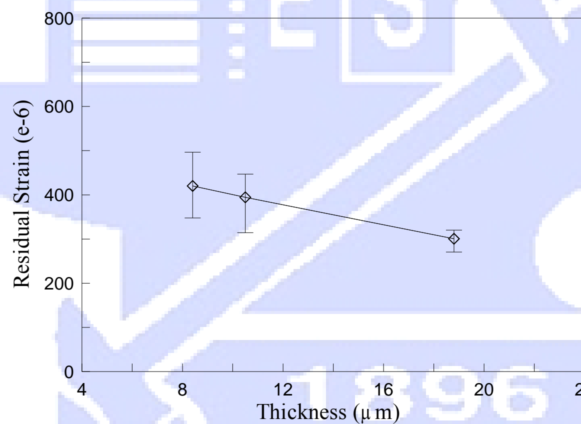

(a)

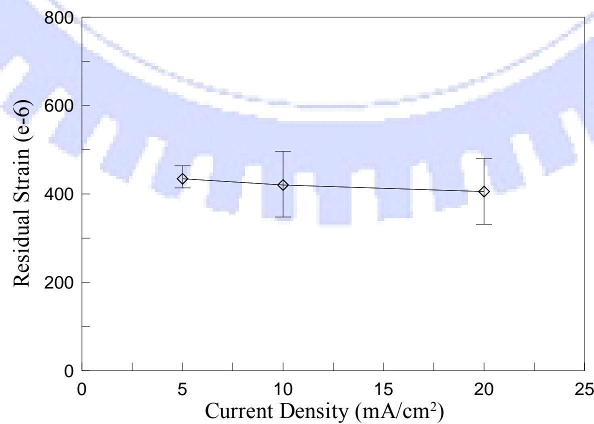

(b)

Figure 35. The determined residual strain (a) in different thickness with constant current density of 10 mA/cm^2 (b) in different current density with thickness of 7.6~8.4μm.

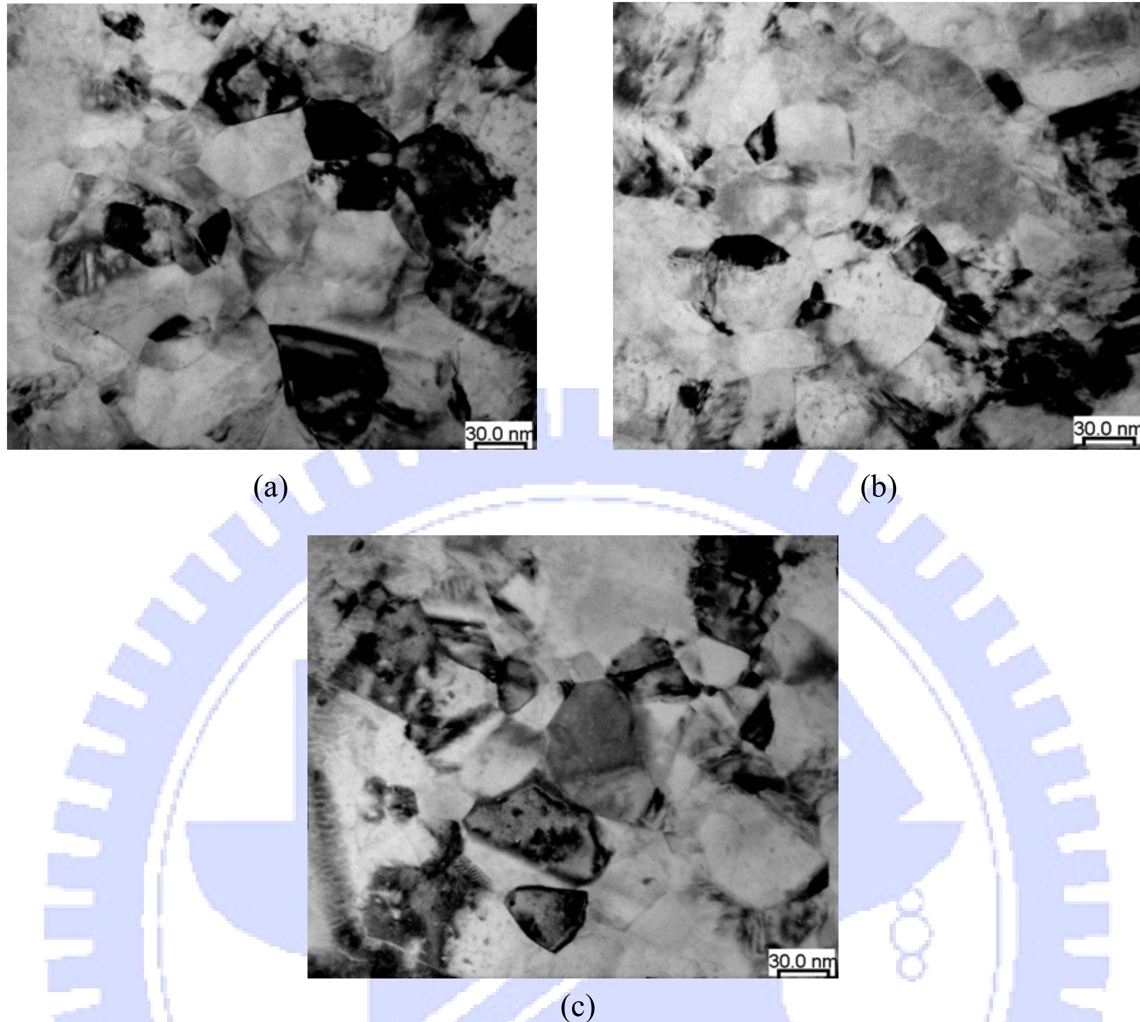

Figure 36. TEM images with plane view of the nickel films at different current densities and thicknesses, which are (a) 5 mA/cm^2 and 3.6 μm (Ni-4), (b) 15 mA/cm^2 and 3.9 μm (Ni-3), and (c) 5 mA/cm^2 and 16.8 μm (Ni-5), respectively.

averaged residual strain is found to be reduced with increasing film thickness. Figure 35(b) shows the residual strain at different current densities of 5, 10 and 20 mA/cm^2 at the similar thickness around 8 μm. The averaged residual strain is found to be only slightly decreased with the increasing current density. The measured results on residual strain indicate that the residual strain variation is more evident at various thickness than the cases of different current densities within our testing range.

Furthermore, the grain sizes of electroplated nickel with different deposition conditions are also identified by transmission electron microscope (TEM). The TEM

images with plane view of the nickel films are shown in figure 36, which includes three samples: nickel films with current density and thickness of 5 mA/cm^2 and 3.6 μm for figure 36(a), respectively, 15 mA/cm^2 and 3.9 μm for figure 36(b), and 5 mA/cm^2 and 16.8 μm for figure 36(c). According to the TEM images shown in figure 36(a) and 36(b), the averaged grain size decreases from 43.97 nm to 35.15 nm when current density increases from 5 mA/cm^2 to 15 mA/cm^2 with the similar film thickness. The increase of current density slightly reduces the grain size of electroplated nickel. By comparing figure 36(a) with 36(c), the averaged grain size changes from 43.97 nm to 42.56 nm when thickness increases from 3.6 μm to 16.8 μm with the same current density of 5 mA/cm^2. The increase of film thickness almost does not influence the grain size of electroplated nickel within our testing range.

Figure 37(a) shows the cross section view of an electroplated nickel film with thickness of 3.6 μm and current density of 5 mA/cm^2. It can be seen that grain size is different at various thickness range. Grain size variance can be further observed by the dark field TEM images shown in figure 37(b) and 37(c), which show the top part and bottom part of the nickel film, respectively. A fine grain size is found on the bottom part

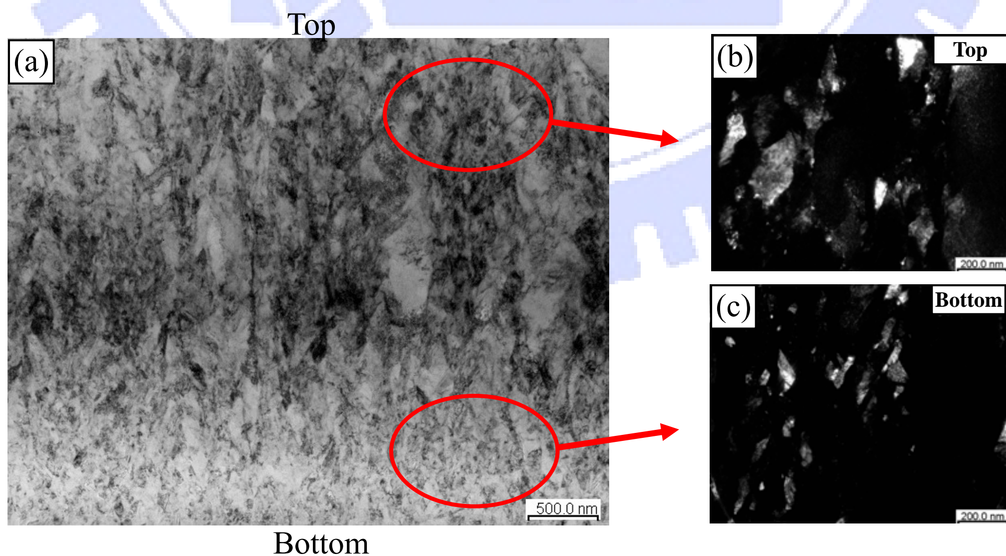

Figure 37. TEM images with cross section view of electroplated nickel film; the dark field images show different grain size in top and bottom regions.

while a coarse grain size is observed on the top part of the nickel film. It is suggested that the amorphous copper seed layer deposited by PVD induces the fine grain size of nickel film near the seed layer since the electrodeposited metal will try to copy the structure of the substrate [75]. When thickness of nickel film exceeds about 1 μm, the grain grows obviously. Then, the grain size is almost consistent when film thickness is over 4 μm, which can be found by comparing figures 36(a) and 36(c).

5.4 Summary

In this study, the CTE and thickness effects of the electroplated nickel films below 20μm at different electroplating current densities are experimentally investigated, and evident variations on CTE, hardness, and Young's modulus are observed. The experimental results indicate that the CTEs are enhanced by the increasing of film thickness and current density. At the current density of 10 mA/cm^2, there is about 37.4% enhancement in CTE with the thickness increased from 8.2 μm to 15.9 μm. At the same thickness about 12 μm, CTE is elevated about 66% when the current density is increased from 5 mA/cm^2 to 20 mA/cm^2. It is also found that hardness and Young's modulus are reduced with the increasing thickness and current density. Furthermore, at different thicknesses, variation of residual strain is a little more evident than that at different current densities, and no obvious deviation on grain size is observed. These results would be helpful in designing micro devices utilized electroplated nickel film at different thickness.

Chapter 6 Metal-Based Vertical Comb Drive

Recently, different fabrication methods of vertical comb drive (VCD) have been widely reported by literatures [8-20] due to its superior characteristics, especially for the considerable out-of-plane displacement with relatively low driving voltage. However, all the reported methods for fabricating VCD are the silicon-based micromachining, which is generally considered as a high cost process and difficult to be integrated with IC circuit. To lower fabrication cost and enhance integration with IC circuit, a low temperature process based on LIGA-like technique to fabricate metal-based VCD is proposed here. In this chapter, the fabrication methods of metal-based VCD are described in detail, and the experimental results are presented and discussed. Furthermore, the fabrication of VCD with angled fingers is also illustrated, which could be achieved by constructing the slope photoresist molds.

6.1 Fabrication Process

The metal-based VCD is fabricated by LIGA-like process, where the lithography technique defines the photoresist as the electroplating mold and the electrodeposition technique produces the metal structures. In this investigation, nickel and copper are electroformed in turn to form the comb structures and sacrificial layers, respectively, and the electroplating molds are created by commercial positive thick photoresist AZ-series (Clariant). Furthermore, electroplated nickel and copper also can act as the seed layer for each other. Therefore, no additional seed layer is required in this process except the first seed layer deposited by sputtering system. With total five photo masks, figure 38 shows the detailed process flow from the combination of AA and BB cross section, where AA cross section presents fabrication of finger structures and BB cross section shows fabrication of springs. First, the seed layer of Cu/Ti is deposited by sputtering system and

copper is electroformed as the 1st sacrificial layer with the 1st mask, as show in figure 38(a), where the 1st copper sacrificial layer provides the operation space (stroke) of the upper (movable) fingers. Subsequently, thick phtoresist is spin coated and patterned with the 2nd mask as the molds for the following electrodeposition, as shown in figure 38(b).

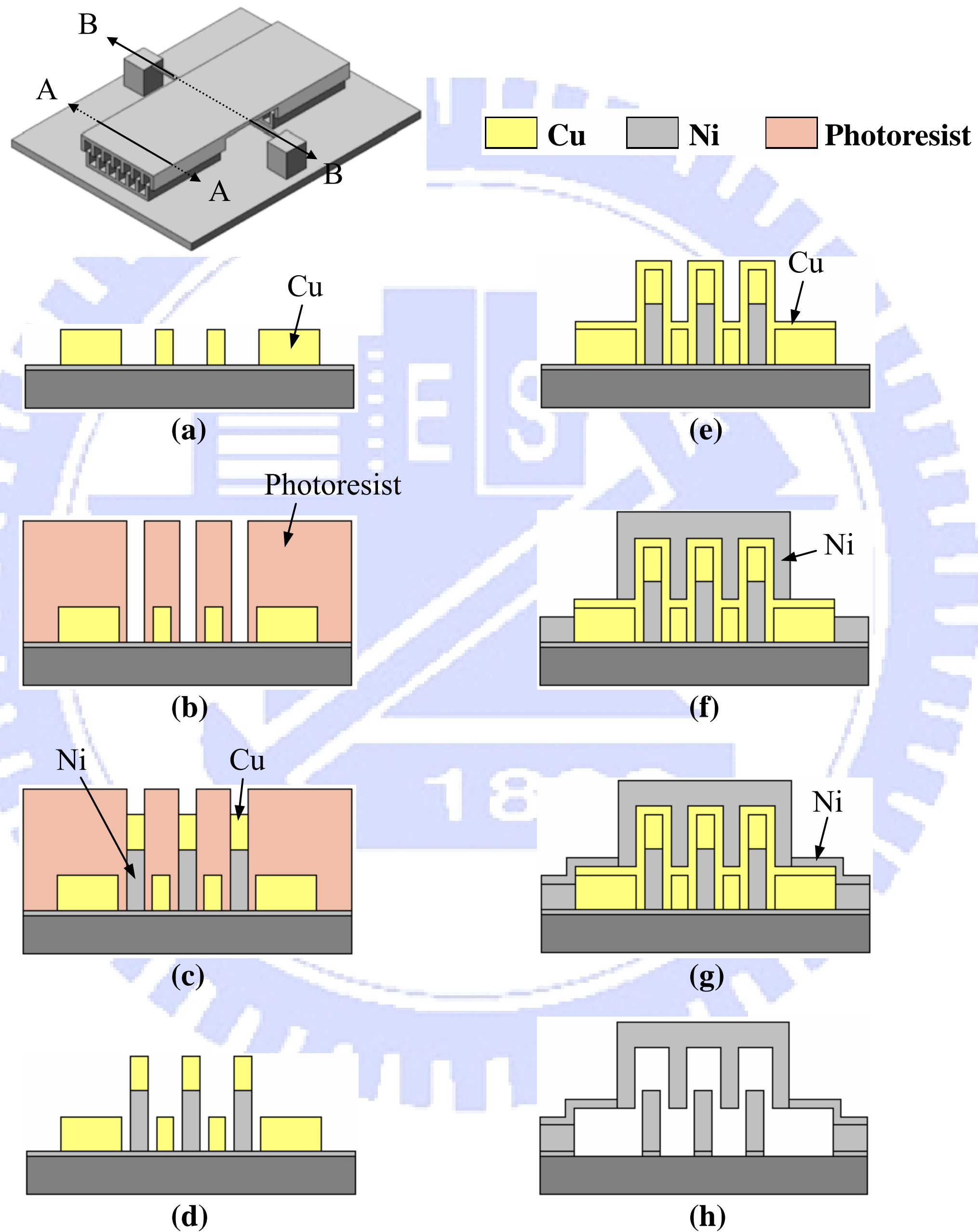

Figure 38. Fabrication process of metal-based VCD by electroforming; (a) electroform Cu; (b) define the electroplating molds; (c) electroform Ni and Cu in turn; (d) remove the molds; (e) electroform Cu; (f) electroform Ni for upper fingers; (g) electroform Ni for springs; (h) release.

Then, nickel is electrodeposited to form the lower fingers which are followed by electroplating copper for creating the 2nd sacrificial layer, as shown in figure 38(c) , where the 2nd sacrificial layer also provides the stroke for VCD operation. After removal of thick photoresist, as shown in figure 38(d), the 3rd sacrificial layer of copper is electroformed with the 3rd mask and creates the gap between the upper and lower fingers, as shown in figure 38(e). Subsequently, with the 4th mask, the upper comb fingers are fabricated with refilling the trenches through nickel electroforming, and the anchors are also constructed simultaneously, as shown in figure 38(f). Then, the springs are electroformed with the molds created by the 5th mask, as shown in figure 38(g). Finally, the fabrication of metal VCD is completed after the release process by wet etching, as shown in figure 38(h).

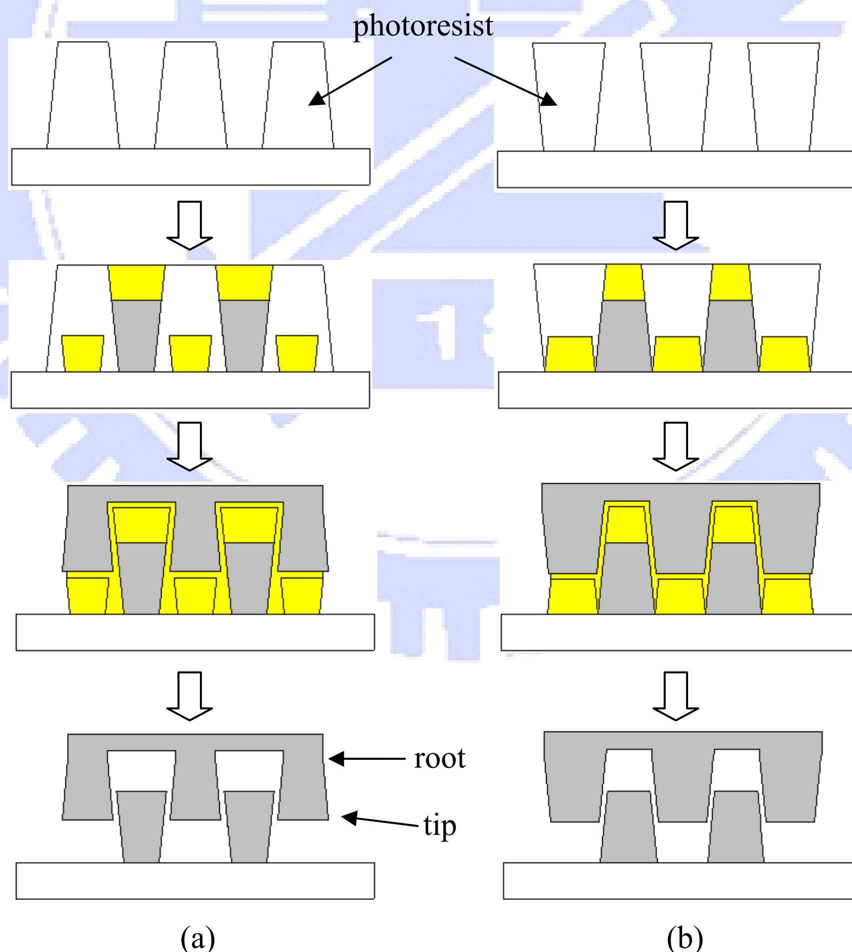

Figure 39. There is a angle of comb finger fabricated by the photoresist with un-vertical sidewall. By (a) positive photoresist and (b) negative photoresist.

By fabrication method of metal-based VCD described above, shape of comb finger is determined by shape of photoresist mold. Generally, the sidewall of comb finger of metal-based VCD is not exactly perpendicular to the substrate because there is always a slight or serious slope of photoresist sidewall, no matter we use positive or negative photoresist. Therefore, the different slope sidewalls of photoresist causes the different finger shapes, called the angled fingers, which affects the actuation performance of VCD. As illustrated by figure 39(a), positive photoresist finally creates the fingers with a wide tip and a narrow root. On the contrary, negative photoresist fabricates the fingers with a narrow tip and a wide root (figure 39(b)). Therefore, negative photoresist is preferred here because it creates a better slope angle of comb finger, which provides the larger output force and the lower driving voltage as described in Chapter 2.

6.1.1 Modified Process of Metal-Based VCD

In general, positive photoresist is more available and has better sidewall performance than negative photoresist for the commercial thick photoresist. For positive photoresist, the profile similar to negative photoresist can be achieved by backside exposure, which means that UV light source is at the backside direction of substrate, because the high intensity region is located on the bottom of photoresist and causes a wide opening on bottom of the photoresist trench, as shown in figure 40. Otherwise, for the backside exposure, contact between photoresist and mask is better than that of the general front side exposure because the photoresist is directly coated on the backside mask, and then creates

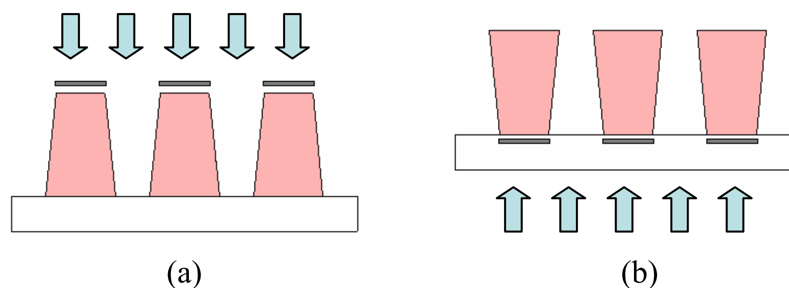

(a) (b)

Figure 40. Positive photoresist created by (a) front side and (b) backside exposure.

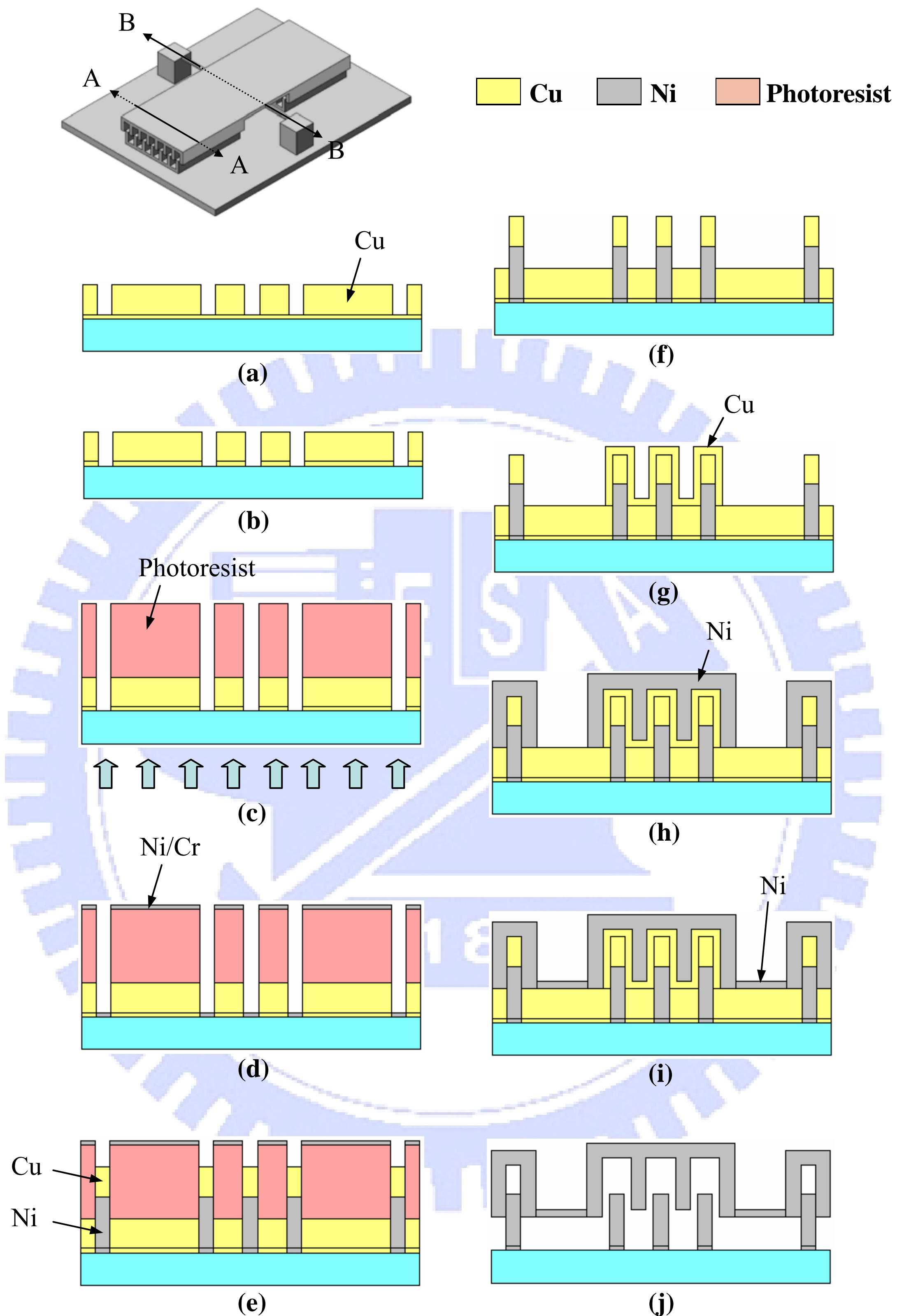

Figure 41. Metal-based VCD fabrication process by the backside exposure method; (a) electroform Cu; (b) removal of 1st seed layer; (c) backside exposure; (d) deposit 2nd seed layer; (e) electroform Ni and Cu in turn; (f) remove photoresist; (g) electroform Cu; (h) electroform Ni for upper fingers; (i) electroform Ni for springs; (j) release.

the better photoresist profile. Therefore, a modified fabrication process of metal VCD by backside exposure is proposed here. The total mask number (4 masks) is one less than that described in figure 38 (5 masks). Additionally, there is also an auto alignment mechanism between 1st sacrificial layer and lower comb finger structure. This mechanism greatly reduces the misalignment problem and makes this process much feasible. Figure 41 shows the detailed fabrication process flow, and the transparent substrate is used here for backside exposure. First, the 1st seed layer of Cu/Ti with thickness of 1000/200 Å is sputtered on the glass substrate, and the 1st sacrificial layer of copper is electroformed (figure 41(a)), which provides the stroke of upper fingers. Then, the seed layer is removed by wet etching for backside exposure (figure 41(b)), where the seed layer of copper is etched away by diluted CR7T (chromium photomask etchant) and titanium is removed with the diluted B.O.E. (buffered oxide etchant). After spin coating the thick positive photoresist, backside exposure is carried out to define the molds (trench structures) for electroforming the lower fingers (figure 41(c)). Subsequently, the 2nd seed layer of Ni/Cr is deposited by electron beam evaporator (figure 41(d)), in which the seed layer deposited on top of photoresist should be electrically isolated from the seed layer deposited on the substrate to avoid electroplating metal on top of photoresist. So, a thin seed layer is preferred here. Then, the lower comb fingers of nickel and the 2nd sacrificial layer of copper are electroformed in turn (figure 41(e)), where the 2nd sacrificial layer also provides the stroke for VCD operation. After removal of photoresist (figure 41(f)), the 3rd sacrificial layer of copper is electroformed to separate the upper and lower comb fingers (figure 41(g)). Then, the upper comb structure and the anchors are fabricated by electroformed nickel (figure 41(h)), which is followed by electroforming the nickel springs (figure 41(i)). After the final release by wet etching, sacrificial copper layers are removed and the metal-based VCD is fabricated (figure 41(j)).

6.1.2 Slope Photoresist for Angled VCD

As described in figure 39, the shape of comb finger is determined by the shape of photoresist mold. Therefore, the angled metal-based VCD can be fabricated with slope control of photoresist sidewall, and its fabrication process flow is the same as the metal-based VCD. There are three general methods to fabricate photoresist with slope sidewall, as shown in figure 42. The first method is proximity exposure (figure 42(a)). Gap between the mask and the photoresist causes diffraction which provides gray scale light intensity at the edge of mask, which produces slope sidewall of the photoresist. The second method is the inclined exposure [41,52], as shown in figure 42(b). Depending on the UV light incident angle, no mater we tilt the light source or the wafer, the photoresist is exposed with an inclined angle, which creates the desired slope sidewall of photoresist. The third method is called multiple shifted exposure [76], as illustrated in figure 42(c). By the partial exposure at each shifting step, the gray scale intensity of UV light can be created with dragging mask in in-plane direction. Thus, the slope of photoresist sidewall can be controlled.

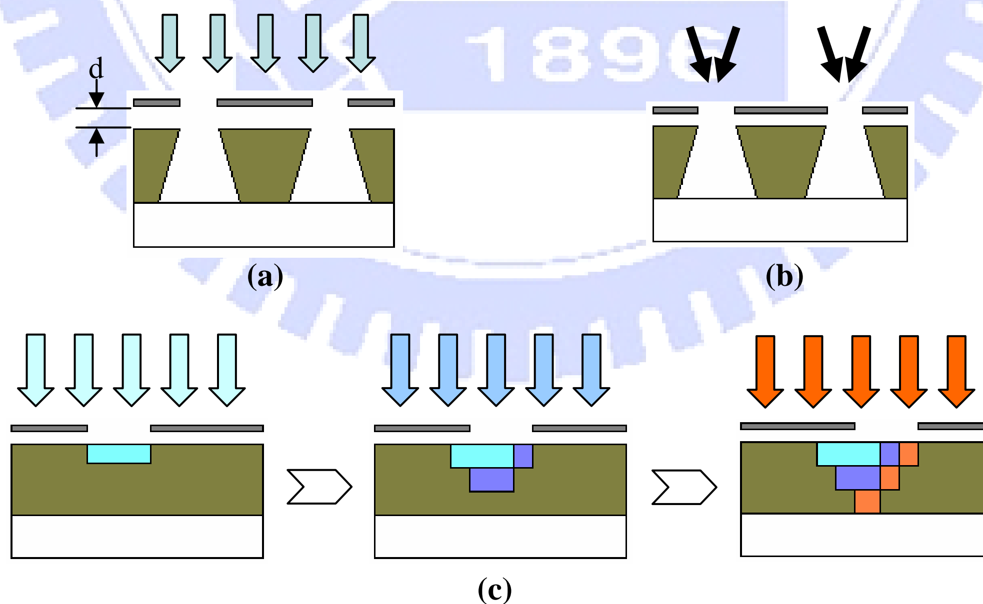

Figure 42. The fabrication methods of slope sidewall photoresist. The negative photoresist is used here. (a) the proximity method (b) inclined exposure (c) multiple shifted exposure.

6.2 Results and Discussions

6.2.1 Metal-Based VCD by Modified Process

The metal-based VCD is fabricated by the modified fabrication process shown in figure 41 in anticipation of better results and performance. In this process, nickel and copper are electroformed as structure and sacrificial layer, respectively, and two positive photoresists, AZP4620® and AZ9260®, are used for electroplating molds. The designed dimensions for the fabrication process are indicated in figure 43. The widths of upper and lower fingers after fabrication are 4–14 μm and 8–15 μm respectively when thickness of 3rd sacrificial layer of copper is deposited as 3 μm. The total stroke of VCD will be 12.5 μm, and the overlap distance of the moving and fixed fingers is 5 μm.

For constructing the molds with backside exposure method (figure 41(c)) to electroform the lower fingers and the 2nd sacrificial layer (figure 41(e)), different photoresists provide different performances. Figure 44 and 45 show SEM pictures of the experimental results after backside exposure (figure 41(c)) by means of AZP4620® and AZ9260®, respectively. As shown in figure 44, a serious shrinkage on bottom of the AZP4620® molds caused by diffraction effect is observed. This shrinkage not only affects the shape of lower comb fingers, but also makes the following process be failed and lowers the production yield. As shown in figure 45, AZ9260® obviously exhibits less shrinkage and provides a more vertical sidewall of electroplating mold than AZP4620®, and this improvement also results in a better yield in the following processes.

In the fabrication step shown in figure 41(d), electron beam evaporator is employed due to its poor capability of lateral deposition, and the seed layer as thin as possible is attempted to avoid the deposition of metal on photoresist sidewall, which induces electrical short between the deposited seed layers on top of photoresist and on glass substrate. Here, the 2nd seed layer of Ni/Cr with thickness 80/50 Å is utilized. Figure 46(a) shows the optical microscope pictures of the results after the deposition of 2nd seed layer, which

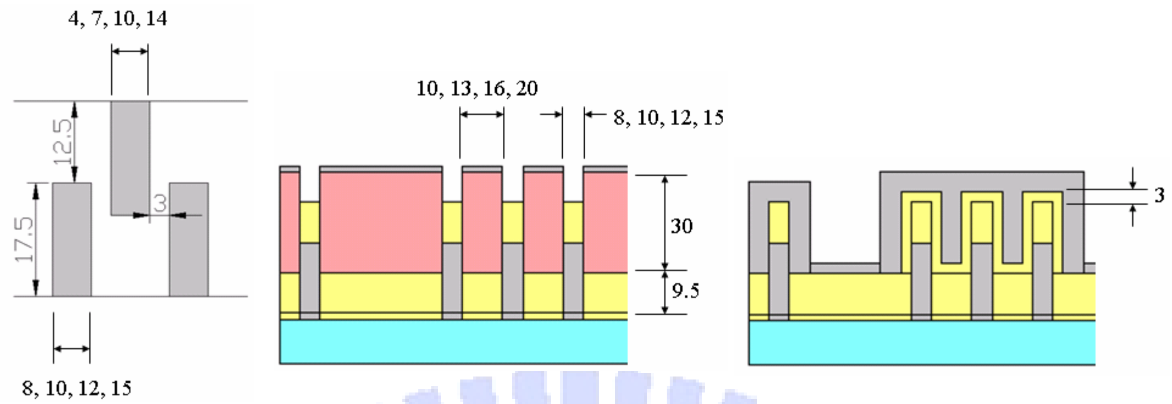

Figure 43. The designed dimensions for fabricating the metal-based VCD by the modified fabrication process. (unit: μm).

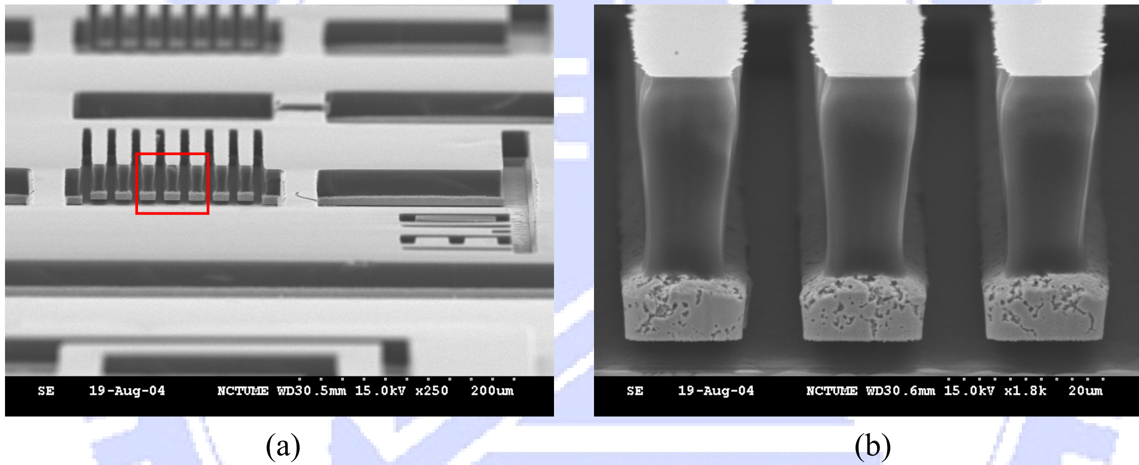

(a) (b)

Figure 44. SEM photographs of positive photoresist AZP4620® after backside exposure; (a) overview and (b) closed view of the molds.

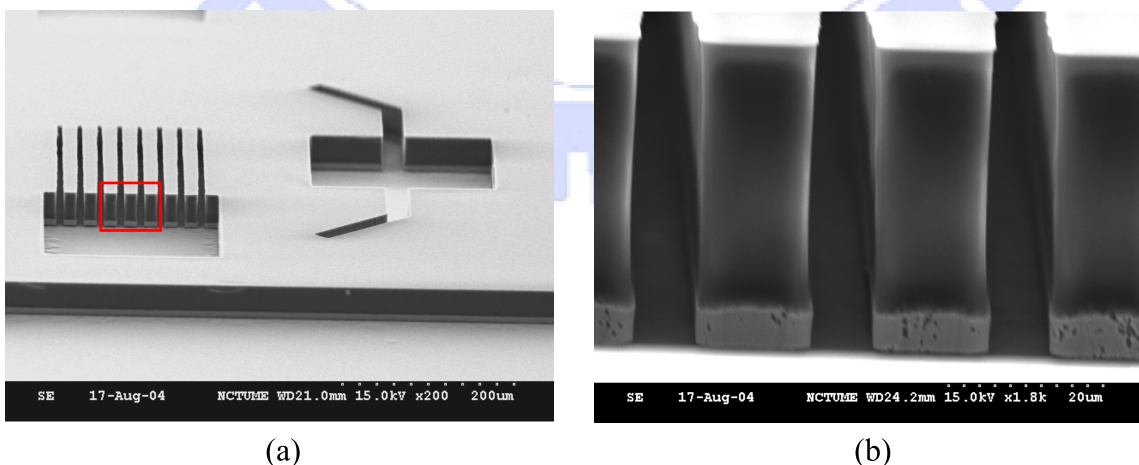

(a) (b)

Figure 45. SEM photographs of positive photoresist AZ9260® after backside exposure; (a) overview and (b) closed view of the molds.

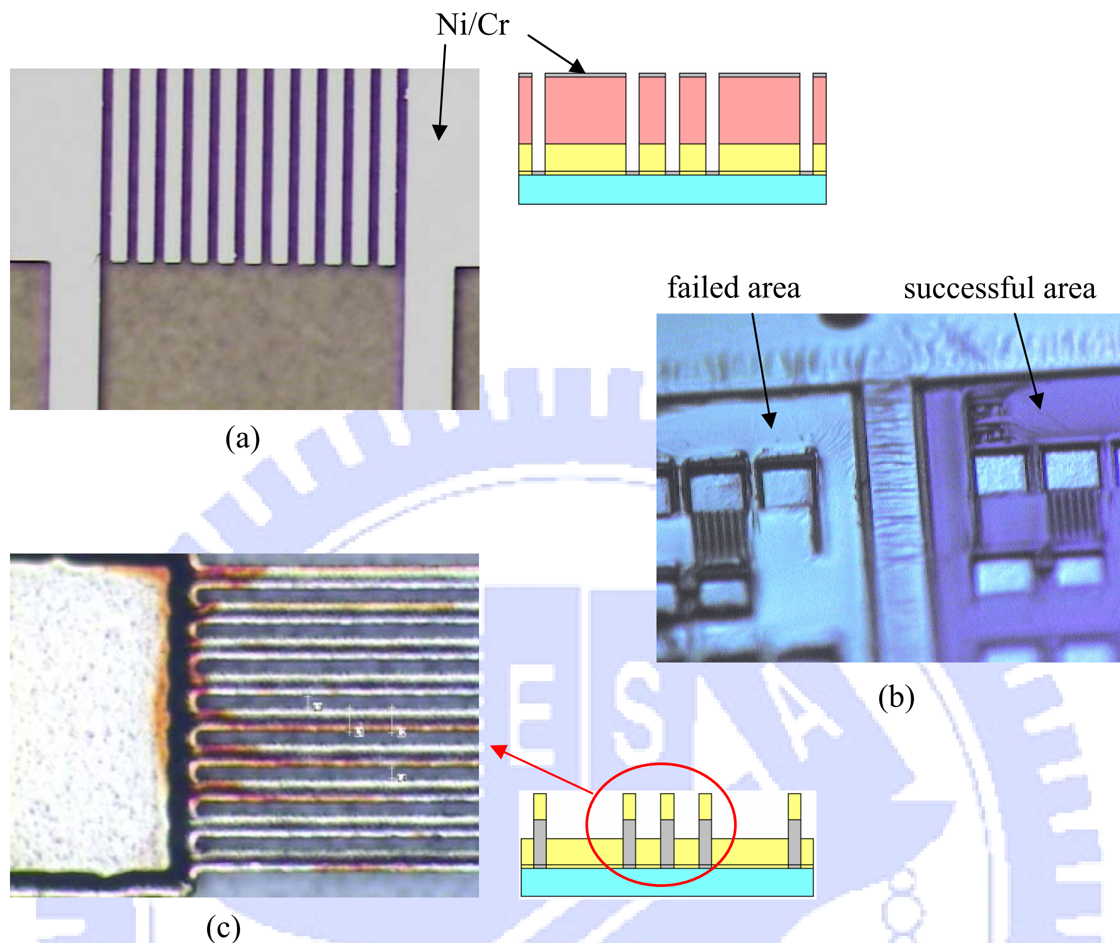

Figure 46. Optical microscope pictures of fabrication results: (a) the 2nd seed layer of Ni/Cr deposited on the phtoresist and substrate, (b) after electroforming nickel to form the lower fingers and anchors, and (c) after removing photoresist.

successfully supplies the following electroforming. Although the seed layer on top of photoresist is initially not electrical short to the seed layer on substrate, some devices are still failed after electroforming the lower comb structures because metal is finally electroplated on top of the photoresist. As shown in figure 46(b), some Ni films are electroplated on top of the photoresist in the failed areas, which is not expected, and no unwanted metal films are deposited in the successful areas. Yield (without electroplating on top of the photoresist) of this step is about 5~10% with AZP4620®, and 90% with AZ9260®. Figure 46(c) shows the fabrication result after removal of photoresist, in which the 2nd sacrificial copper layer is deposited (as the step shown in Figure 41(f)).

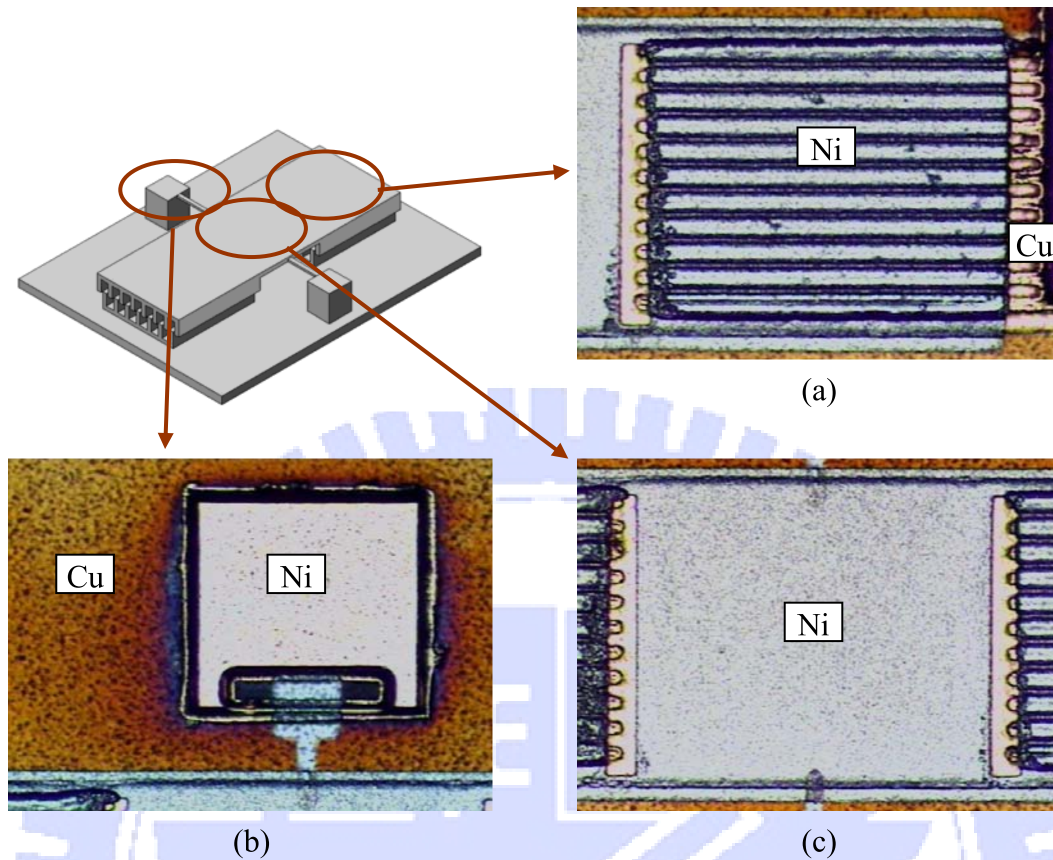

Figure 47. Optical microscope pictures of the fabricated metal-based VCD; the process is completed except final release; (a) top of moveable fingers, (b) anchor and torsion spring, and (c) mirror plate.

Figure 47 shows the optical microscope pictures of different parts of the fabricated metal-based VCD without the final release. The silver areas are the electroformed Ni structure and the brown areas are the electroformed Cu sacrificial layer. Figure 47(a) shows top of the moveable fingers, figure 47(b) shows anchor and torsion spring of the VCD, and figure 47(c) shows the mirror plate made of nickel. After wafer dicing, the chips are etched by solution of $NH_4OH + H_2O_2$ for final release, which is followed by immersing the chips in isopropyl alcohol (IPA) to replace water for reducing the surface tension force during drying. Figure 48 shows the SEM pictures of VCD fabricated by means of AZP4620® after final release, in which the serious shrinkage of AZP 4620 during backside exposure causes the tooth shape of lower fingers. Figure 48(c) illustrates the

formation process of tooth shape. Furthermore, when the trench is narrow, there are holes remained at center of cross section of upper fingers due to incomplete nickel refilling during electroforming, as shown in figure 48(d), and the wide trench helps eliminate these remaining holes with the complete nickel refilling, as shown in figure 48(e).

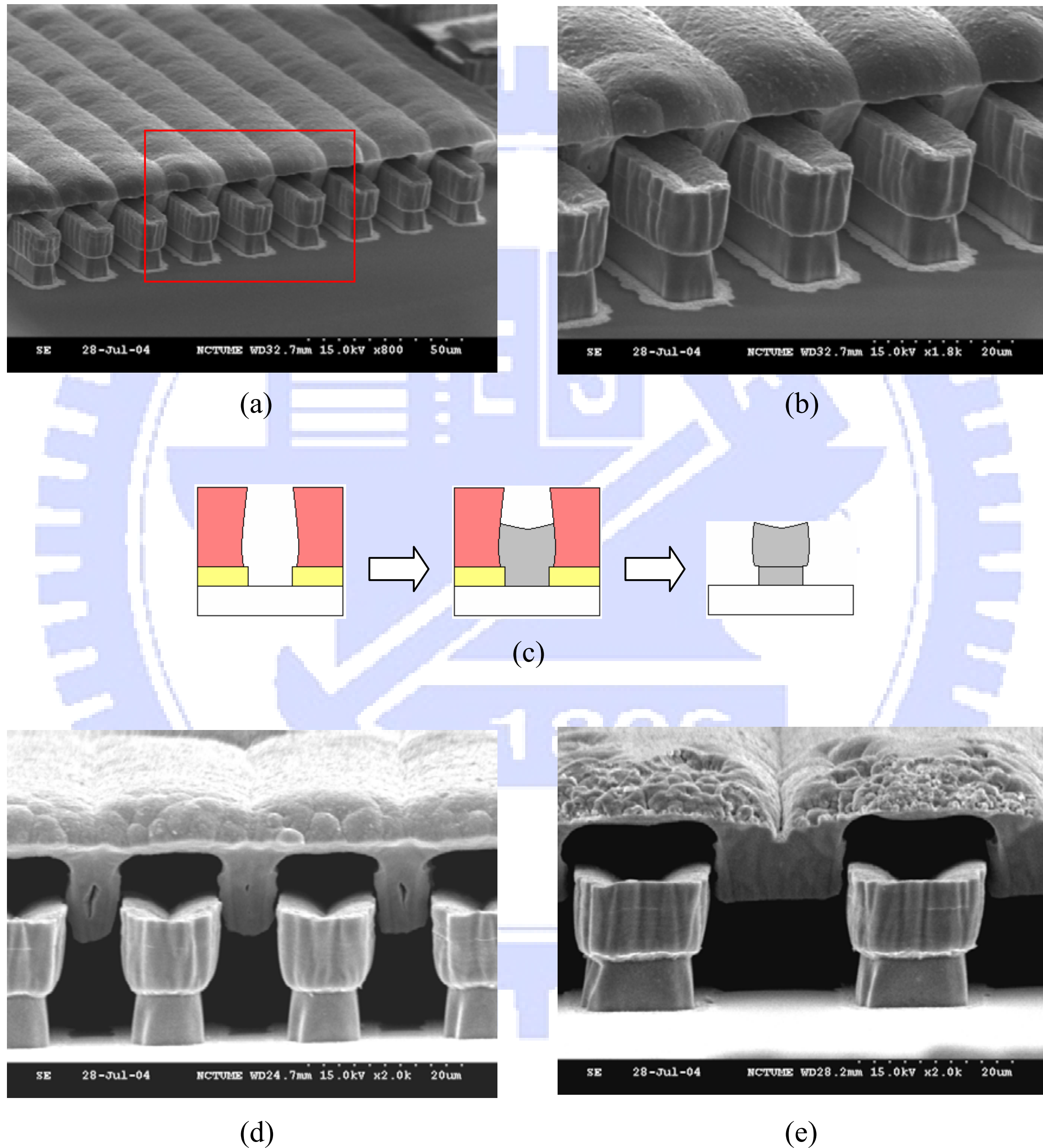

Figure 48. SEM photographs of fabricated metal-based VCD by AZP4620® with tooth shaped lower fingers; (a) upper and lower fingers, (b) closed view, (c) schematic illustration of tooth shape formation, (d) narrow trench with remaining holes, and (e) wide trench without remaining holes.

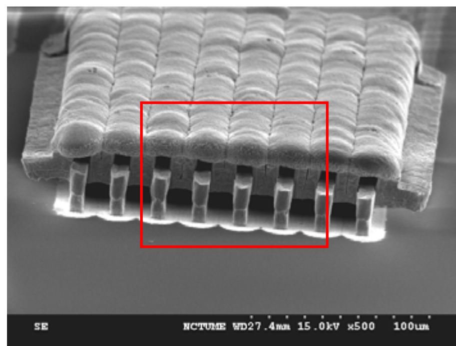

(a)

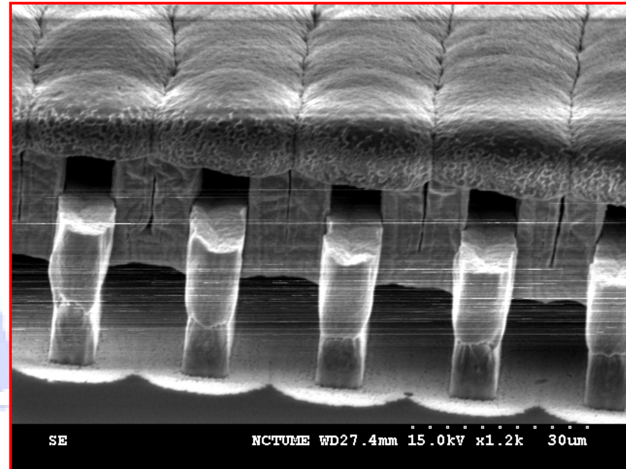

(b)

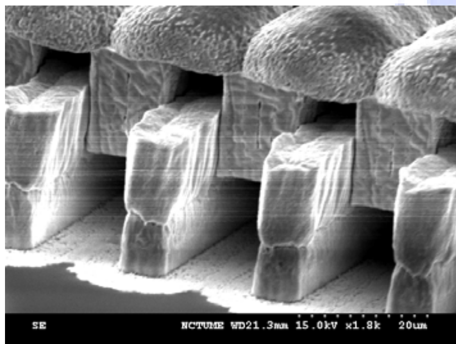

(c)

Figure 49. SEM photographs of fabricated metal-based VCD by AZ9260®; (a) upper and lower fingers, (b) closed view, and (c) closed view in another angle. Thickness of 3rd sacrificial layer is about 2–3 μm here.

Employment of photoresist AZ9260® provides a good improvement on reducing tooth shape of the lower fingers caused by diffraction. As shown in figure 49, the tooth shape of lower comb finger is reduced obviously, and there is a properly vertical sidewall of lower fingers, as shown in figure 49(b). However, the upper fingers are stuck on the lower fingers, even though a long releasing time is tried (7 days). It is suggested that thickness of 3rd sacrificial copper layer about 2–3 μm utilized here is insufficient to separate the upper and lower fingers. To create the desired gap, the thicker 3rd sacrificial copper layers about 4–6 μm and 6–8 μm are electroformed, respectively. However, as observed by experimental results shown in figure 50, the upper fingers are still stuck on the lower fingers with the increase of copper thickness. The thicker copper layer does not work. In figure 50(b), it is clearly found that gaps on roots of the upper fingers are large

especially, which reveals that the electroformed 3rd sacrificial copper layer is concentrated on top of the 2rd sacrificial copper layer. Therefore, as schematic illustration in figure 51, it is suggested that concentration of electric line on the metal corners results in concentration of the next copper deposition. Additionally, the trench structure also limits the copper ion to be transported from top to bottom of the trench. So, it is difficult to deposit a uniform metal layer in a trench with high aspect ratio, and the upper and lower fingers cannot be separated successfully by increasing thickness of the 3rd sacrificial copper layer.

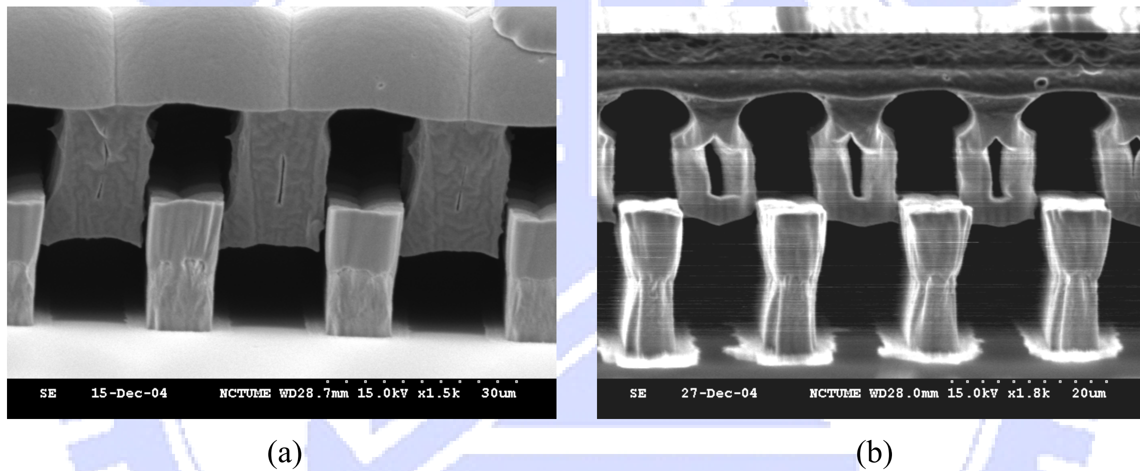

(a) (b)

Figure 50. SEM photographs of the fabricated metal-based VCD with the increased thickness of 3rd sacrificial copper layer; (a) thickness of copper layer about 4–6 μm, and (b) thickness of copper layer about 6–8 μm.

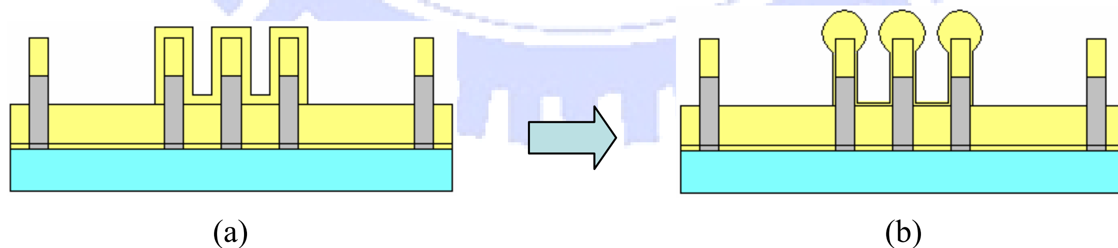

(a) (b)

Figure 51. The electroplated copper concentrates on top of the lower fingers when thickness of 3rd sacrificial layer is increased; (a) the desired uniform deposition of copper layer; (b) the deposition results of copper layer due to electric line concentration and ion delivery problem.

6.2.2 Slope Control of Photoresist Sidewall

As described in figure 39 and section 6.1.2, the angled metal-based VCD can be achieved through controlling the photoresist profile. Here, the technique for fabricating slope photoresist is also developed. In order to construct the slope thick negative photoresist for the preferred inclined angle of comb finger, the process of SU-8 GM1060 with thickness about 60 μm is investigated. Figure 52 shows the experimental results by proximity exposure, in which the thickness of SU-8 is about 60–62 μm, the tested gaps include 0 μm, 100 μm, 200 μm and 300 μm with the same exposure dosage, 5 sec with exposure intensity of 40mW/cm^2. The experimental results indicate that proximity exposure enhances the slope of SU-8 with increasing gap, but it is an obviously curved sidewall, which is not expected. Therefore, increase of exposure dosage is further tested

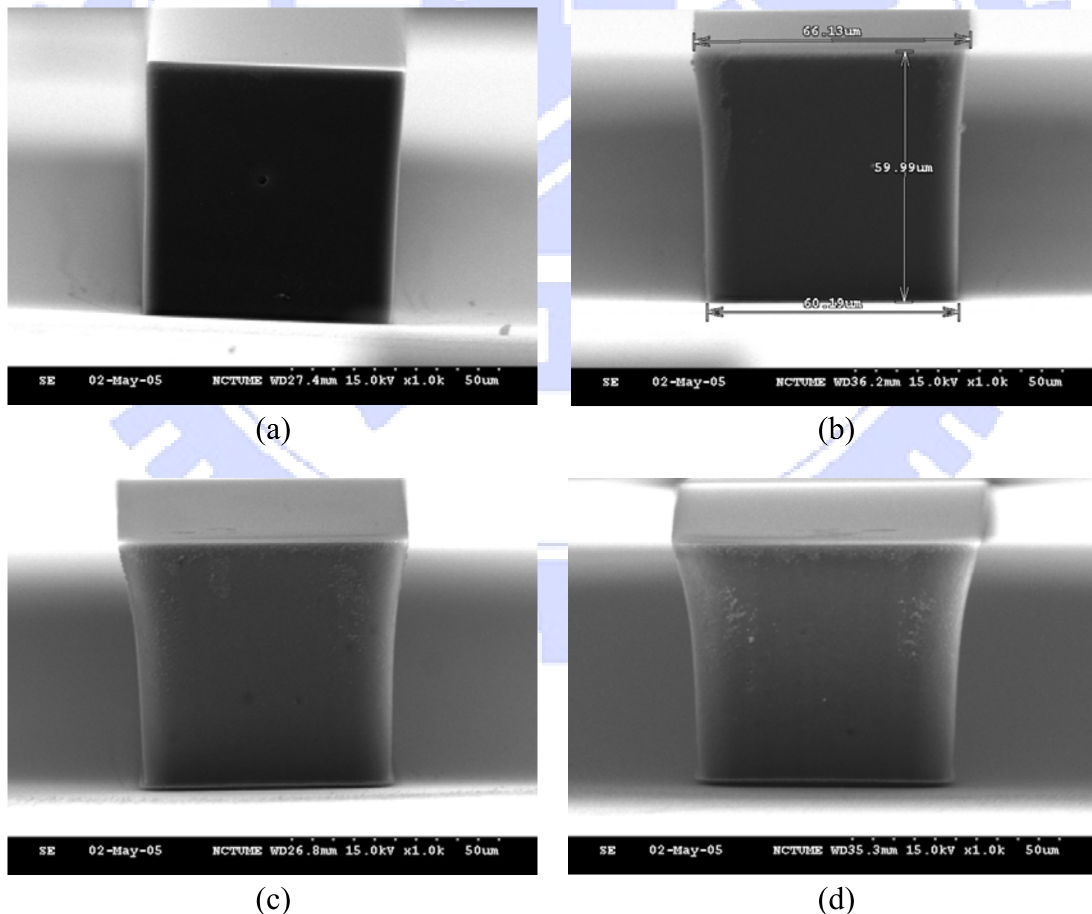

Figure 52. Experimental results of SU-8 structures with thickness of 60–62 μm, and the proximity gaps are (a) 0 μm, (b) 100 μm, (c) 200 μm, and (d) 300 μm, respectively.

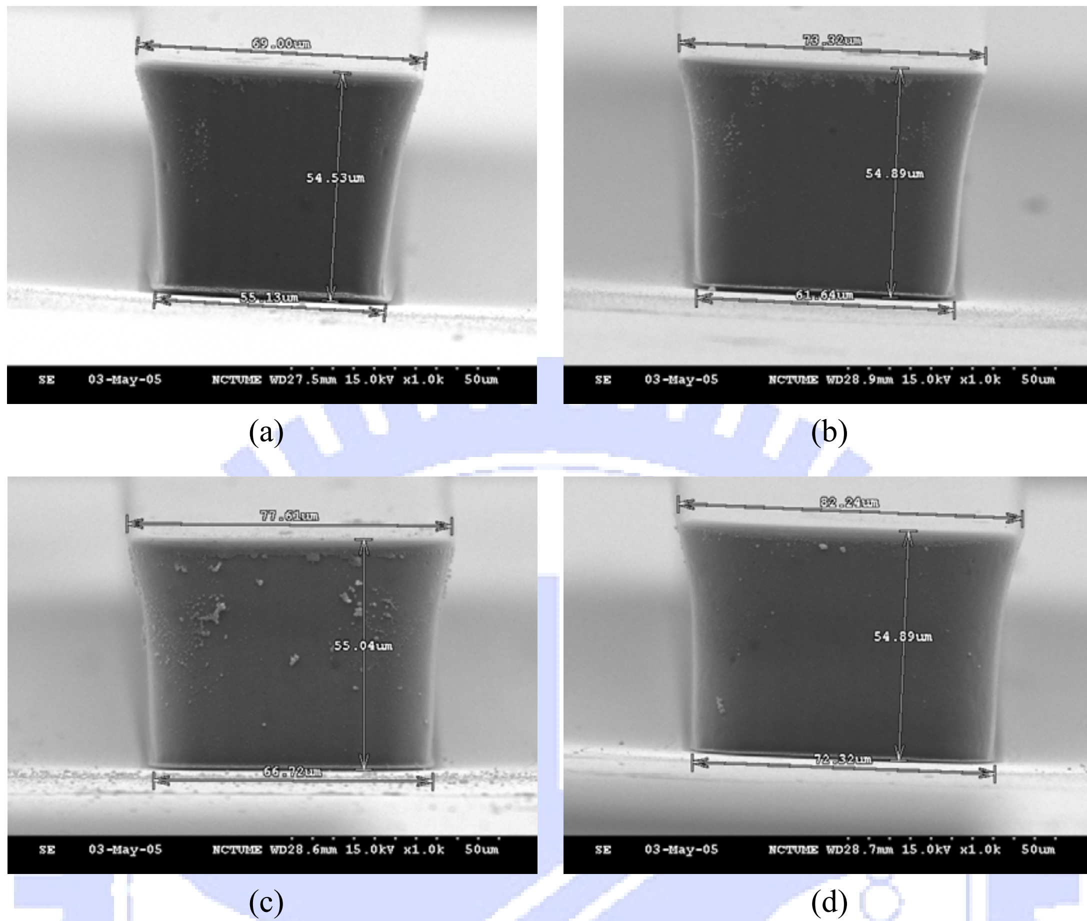

Figure 53. Experimental results of SU-8 structures with thickness about 55 μm, exposure proximity of 300 μm, and the exposure times are (a) 3 sec, (b) 5 sec, (c) 8 sec, and (d) 12 sec, respectively.

for constructing the non-curved sidewall of photoresist. As shown in figure 53, exposure times including 3 sec, 5 sec, 8sec and 12 sec are tested with SU-8 thickness of 55 μm and proximity gap of 300 μm. However, it is found that the increase of exposure dosage only makes the SU-8 structures wider, but not straighter. The curved photoresist sidewall has not been improved.

Another method by multiple shifted exposure is also tested here. In this experiment, the SU-8 thickness about 62–65 μm and proximity gap of 70 μm are used. The total exposure times are 1.0 sec, 2.0 sec and 2.6 sec, respectively. The detailed exposure conditions are listed in table 4, and each shifting distance (step) is 5 μm. For sample 1,

the exposure is divided into 10 steps, and the exposure time in each step is 0.1 sec. Thus, the total exposure time is 1 sec for sample 1. For sample 3, the exposure condition is similar to sample 1, but the exposure time in each step is increased from 0.1 sec to 0.2 sec. For sample 2, the exposure is also divided into 10 steps, but the exposure dosage is doubled in the center steps. Figure 54 shows the experimental results, which indicate that a large slope angle can be obtained by multiple shifted exposure. But the serious curve of photoresist sidewall is also observed, which cannot be further eliminated even though the exposure dosage is increased in medium of moving range.

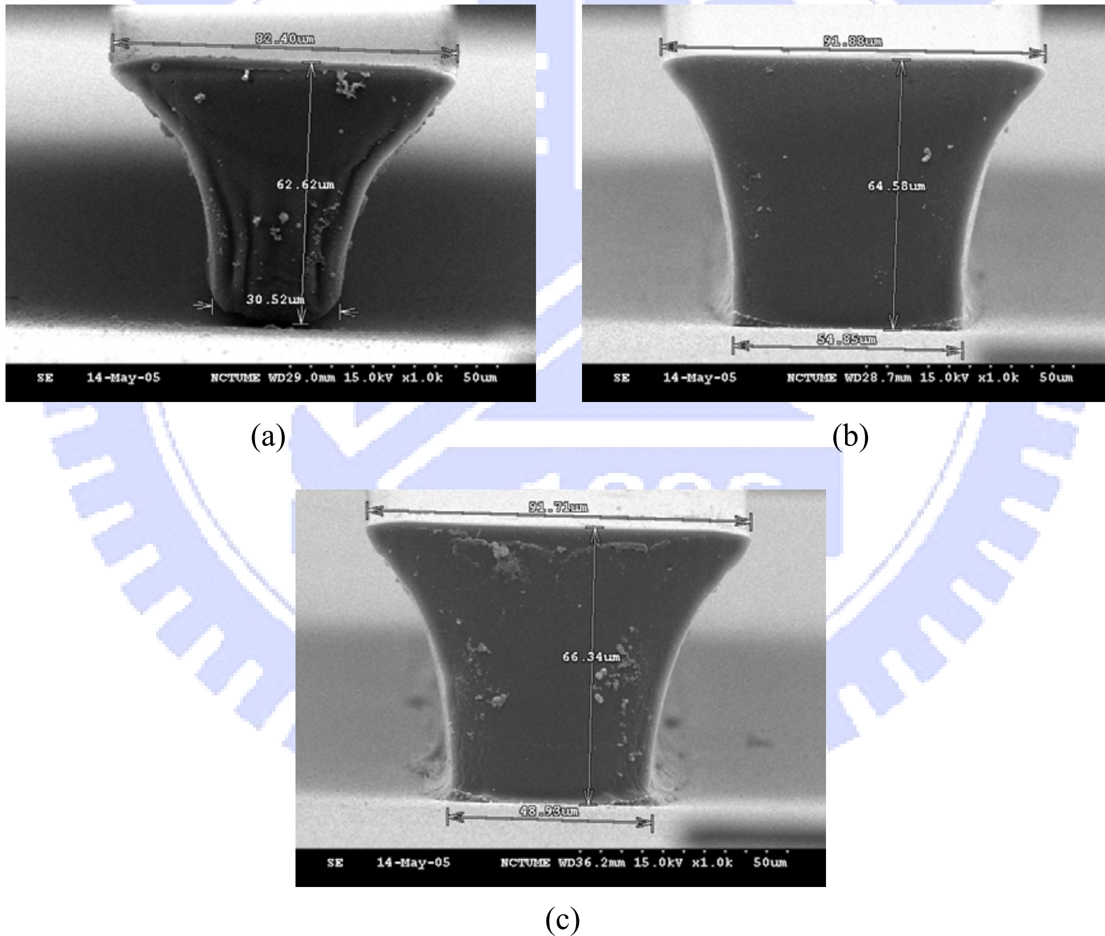

(a) (b)

(c)

Figure 54. Experimental results of multiple shifted exposure; (a) sample 1, (b) sample 2, and (d) sample 3 the photoresist thickness is about 62–65 μm, and the proximity gap is 70 μm;

Table 4. The exposure conditions for multiple shifted exposure. (step = 5 μm)

Sample No.	Exposure conditions
1	0.1 sec × 10 steps
2	0.2 sec × 4 steps → 0.4 sec × 3 steps → 0.2 sec × 3 steps
3	0.2 sec × 10 steps

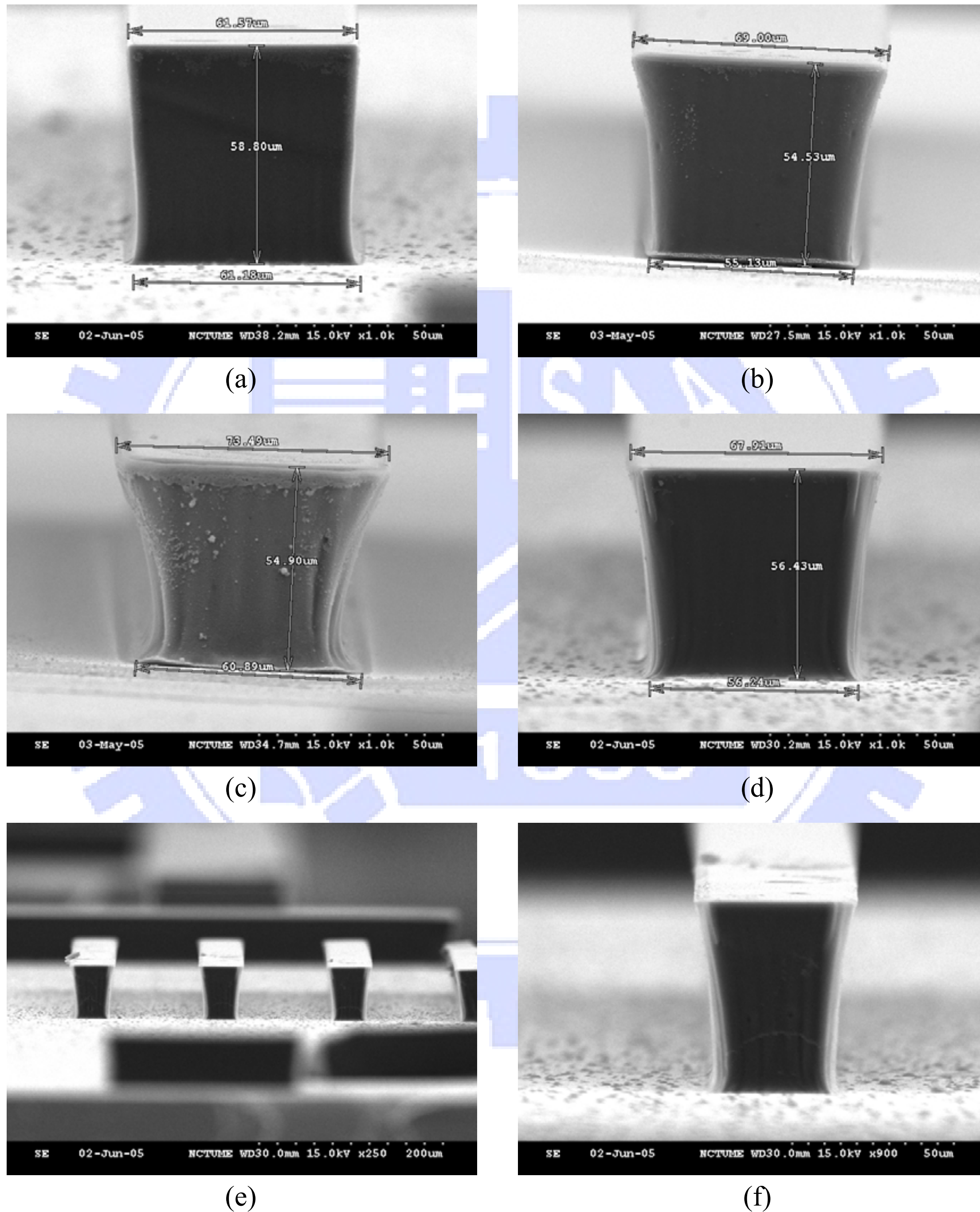

Figure 55. Experimental results of the improved method; original proximity exposure with gaps of (a) 0 μm, (b) 300 μm, and (c) 500 μm; (d)–(f) the proximity exposure with z-axis shifting.

Here, another new idea is tested by combining the proximity exposure and the multiple shifted exposure. By this method, the multiple shifted exposure is carried out in z axis direction and provides a new approach for adjusting the dosage profile in proximity exposure. In this experiment, the total exposure time of 3 sec is used with SU-8 thickness about 57 μm. Then, the exposure is divided into 6 steps. Thus, the exposure time is 0.5 sec in each step. The proximity gaps of 0 μm, 100 μm, 200 μm, 300 μm, 400 μm and 500 μm are performed in turn. Figure 55 shows the SEM images of experimental results. Figures 55(a), 55(b), and 55(c) show the original proximity exposure results with proximity gaps of 0 μm, 300 μm, and 500 μm, respectively, and figures 55(d)–(f) show experimental results of the modified method, proximity exposure with z-axis shifting. Obviously, this exposure method improves the curve problem of photoresist sidewall comparing to the original proximity exposure method and the multiple shifted exposure—the slope sidewall of SU-8 is straighter. These experimental results are helpful for fabricating the metal-based VCD with angled fingers.

6.3 Summary

Here, a novel method with low cost and low temperature process for fabricating the metal-based VCD is proposed, in which nickel and copper are electroformed in turn to form the VCD structures and the sacrificial layer. Employment of photoresist AZ9260® improves sidewall quality of the electroplating molds created by backside exposure, and the 2nd seed layer of Ni/Cr with thickness of 80/50 Å deposited by electron beam evaporator provides a successful electrodeposition for the following structures. However, the non-uniform deposition of copper film (3rd sacrificial layer), which is concentrated on top of the trench structures, fails to separate the upper and lower fingers. Three methods are suggested here to overcome this non-uniform problem: first, a thin copper layer pre-deposited on the trench surface by sputtering could improve the film uniformity in the

following electrodeposition. Second, the pulse-reverse current source generally enhances uniformity of the deposited film. Third, the superconformal electrodeposition of copper film used in damascene process provides a good deposition on bottom of the trench [77-78], which avoids the deposited copper concentrating on top of the trench.

Additionally, the slope control of photoresist sidewall is also investigated with the commercial negative photoresist SU-8. A new method, called proximity exposure with z-axis shifting, is demonstrated to improve the curve problem of photoresist sidewall, in which the slope sidewall of photoresist SU-8 is increasingly straight. The fabrication of slope photoresist mold is helpful for fabricating the metal-based VCD with angled fingers.

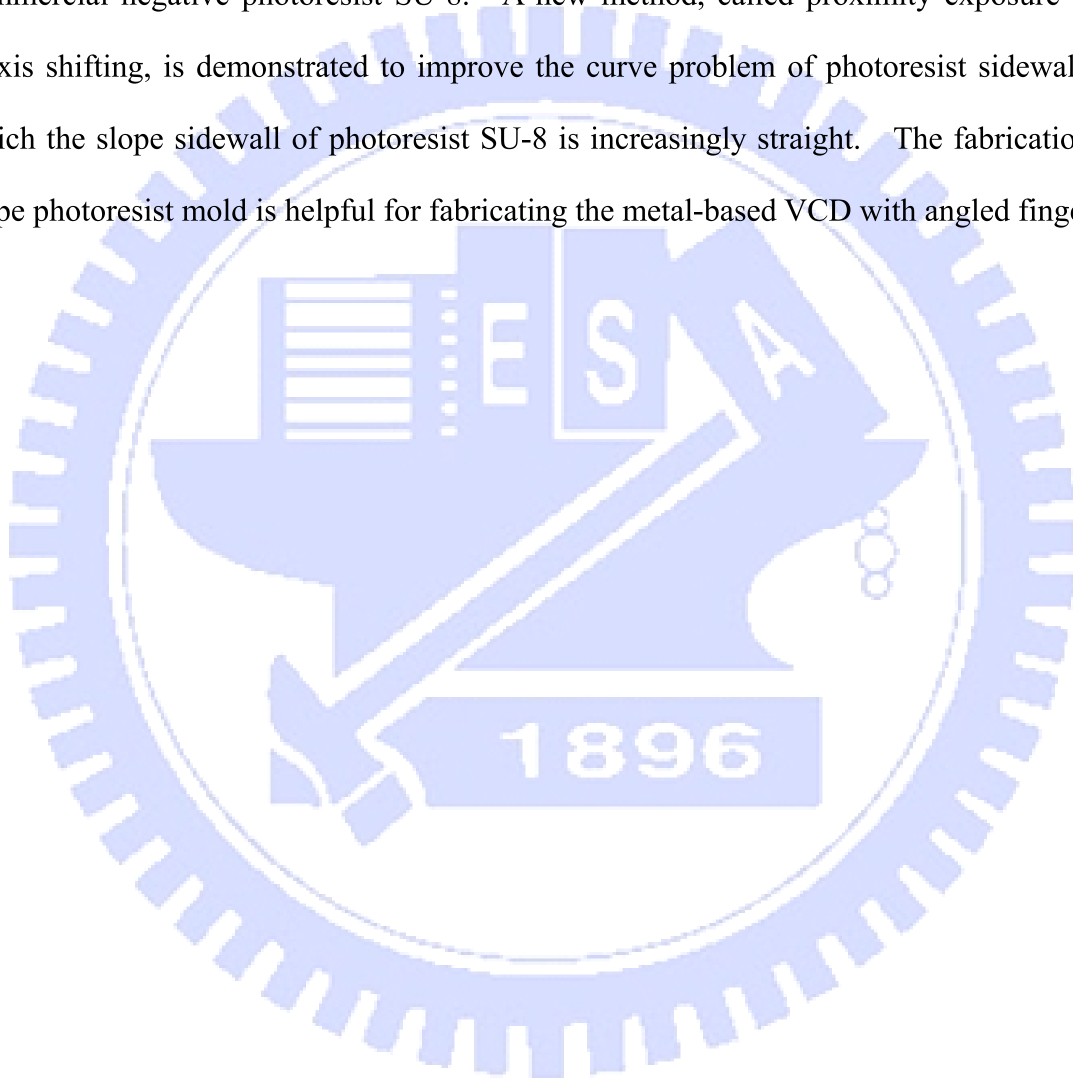

Chapter 7 Conclusion

7.1 Summary

In this study, novel fabrication methods are proposed to fabricate the polymer and metal-based VCDs. All methods are low cost and low temperature, which provides the increasingly processing flexibility and the potential on integrating with IC, and only the basic equipment of LIGA-like process is required.

In Chapter 2, the operation model of VCD is established first. The theoretical analyses are performed with solving the force balance equation to determine the static response of VCD, where the relationship of capacitance versus displacement is extracted by FEM simulation. According to the static analysis, the bottom plate has an evident influence on the performance of VCD, especially for the final part of operation stroke. It is also found that the angled finger enhances the output force of VCD, which results in a low driving voltage at the same rotation angle.

In Chapter 3, the DoMPE process is proposed to enhance the complexity of suspended 3D photoresist microstructures by incorporating backside gray-tone lithography and a partial exposure technique. The process parameters are experimentally characterized. It is found that soft-bake time plays a significant role in the DoMPE process, and affects development depth and fabrication stability. Different 3D photoresist microstructures with multiple levels on the front and back sides are successfully fabricated and presented to show the enhancement effect using the proposed technique. The increase of thickness variation on the gray-tone mask can further enhance the complexity of 3D microstructures. Without any additional sacrificial layer and etching process, the DoMPE process can act as a convenient and basic platform that provides an affordable solution to construct flexible features in three dimensions for MEMS applications.

In Chapter 4, the polymer-based VCD by using the positive thick photoresist AZ9260® as the structural material is fabricated through the proposed DoMPE process. The front-side partial exposure defines the height of the fixed lower fingers, and the back-side partial exposure creates the suspending space of the upper fingers. The staggering sets of fingers with a proper initial overlap and self-alignment are easily achieved by this way. The metal layer is finally deposited on the structural surface by the sputtering system for the suitable electric conductivity to activate the polymer VCD, and the desired electric isolation is realized by the overhang design. By comparing the analytical and experimental results, the feasibility on fabricating polymer VCD through DoMPE process is verified with a measured rotation angle of 2.31° under the driving voltage of 158.3V. This investigation also demonstrates one application of DoMPE process on active devices.

In Chapter 5, the material properties of electroplated nickel are experimentally characterized, and evident variations on CTE, hardness, and Young's modulus are observed under different film thicknesses and current densities. By increasing the film thickness and current density, experimental results indicate that the CTEs are enhanced, and the hardness and Young's modulus are both reduced. These results would be helpful in designing micro devices with utilizing electroplated nickel film at different thicknesses and current densities.

In Chapter 6, the novel method for fabricating the metal-based VCD is proposed, where the nickel and copper are electroformed in turn to form the VCD structures and the sacrificial layer. Experimental results show that introducing photoresist AZ9260® improves the sidewall quality of the electroplating molds and also provides the high production yield. However, it is found that depositing a uniform copper film cover the trench surface as the 3rd sacrificial layer is a key step in this process. Furthermore, the investigation of slope control of photoresist sidewall indicates that a novel method, called

proximity exposure with z-axis shifting, improves the curve problem of photoresist sidewall, in which the sidewall of the sloped photoresist SU-8 is increasingly straight.

7.2 Future Research Direction

The future research directions focus on improving and extending the current results. For the polymer-based VCD, the removal of torsion springs near the stationary fingers is performed by manual probe in this dissertation. This method lowers the production yield. In the future, the yield should be obviously improved by using excimer laser or focus ion beam (FIB) micromachining to cut the torsion springs. Additionally, with the better physical and chemical properties, photoresist SU-8 may replace AZ9260® on fabricating the polymer-based VCDs for the better performances, in which IPA can be further introduced to reduce the stiction phenomenon during the final release.

For the property characterization of electroplated nickel, one should be interested to the mechanism that induces the large variation range of CTE. According to literatures, grain size [79-81] and internal stress (or strain) [63-65] should be important factors that result in CTE deviation, because the change of former causes different occupied volumes of grain boundaries, where the structure in grain boundary is much different from that in grain, and the latter indicates the defect quantity contained in material. Generally, texture also affects the material properties due to different orientations [75]. In the future, x-ray diffraction (XRD) characterization may help to determine the grain size, internal stress, and texture, which should reveal some information about CTE deviation.

For the fabrication of metal-based VCD, a uniform copper film cover trench surface as the 3rd sacrificial layer should be deposited successfully for separating the upper and lower fingers. Three methods are suggested:

(1) Pre-deposition of a thin copper layer on trench surface.

(2) Pulse-reverse electrodeposition.

(3) Superconformal electrodeposition.

where a thin copper layer pre-deposited on the trench surface by sputtering could improve the film uniformity in the following electrodeposition, and the pulse-reverse current source generally enhances uniformity of the deposited metal film. The superconformal electrodeposition of copper film used in damascene process provides a good deposition on bottom of the trench [77-78], which avoids the deposited copper concentrating on top of the trench.

7.2.1 Other Approaches to Fabricate the Metal-Based VCD

Here, two approaches for fabricating the metal-based VCD are proposed. The first approach employs the multi-level electroplating mold constructed by front side multiple partial exposure to fabricate the staggering fingers. Figure 56 shows the process flow in detailed. First, a thick metal film as the opaque mask is deposited and patterned by lift-off process on the glass wafer (figure 56(a)). With the same process, a thin metal as the gray-tone mask is also defined on the desired areas (figure 56(b)). Then, this glass wafer is used as the mask for the front side multiple exposure. On another substrate, a seed layer is deposited by PVD first (figure 56(c)). Then, the nickel posts, which work as the anchors of VCD, are constructed by LIGA-like process (figure 56(d)). Subsequently, a thick positive photoresist is spin-coated (figure 56(e)), and the front side multiple partial exposure with the pre-fabricated glass wafer as mask is carried out (figure 56(f)), where trenches with different depths (shallow or deep) are created. In figure 56(f), the dotted line indicates the shallow trench for constructing the torsion springs, which also provide the required electroplating current through the nickel posts. After development, the trenches are fabricated, which is followed by metal deposition by electron beam evaporator (figure 56(g)). This metal film works as the 2nd seed layer for the following nickel deposition. Then, the nickel is electroformed to form the whole structures of the

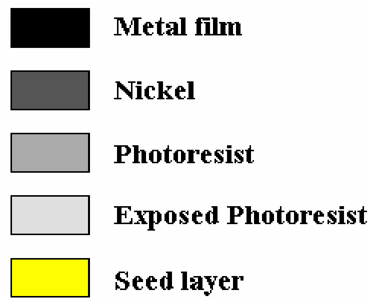

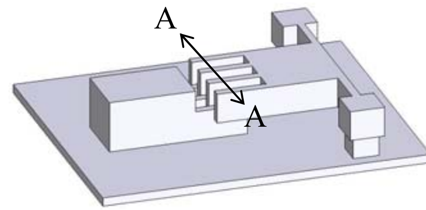

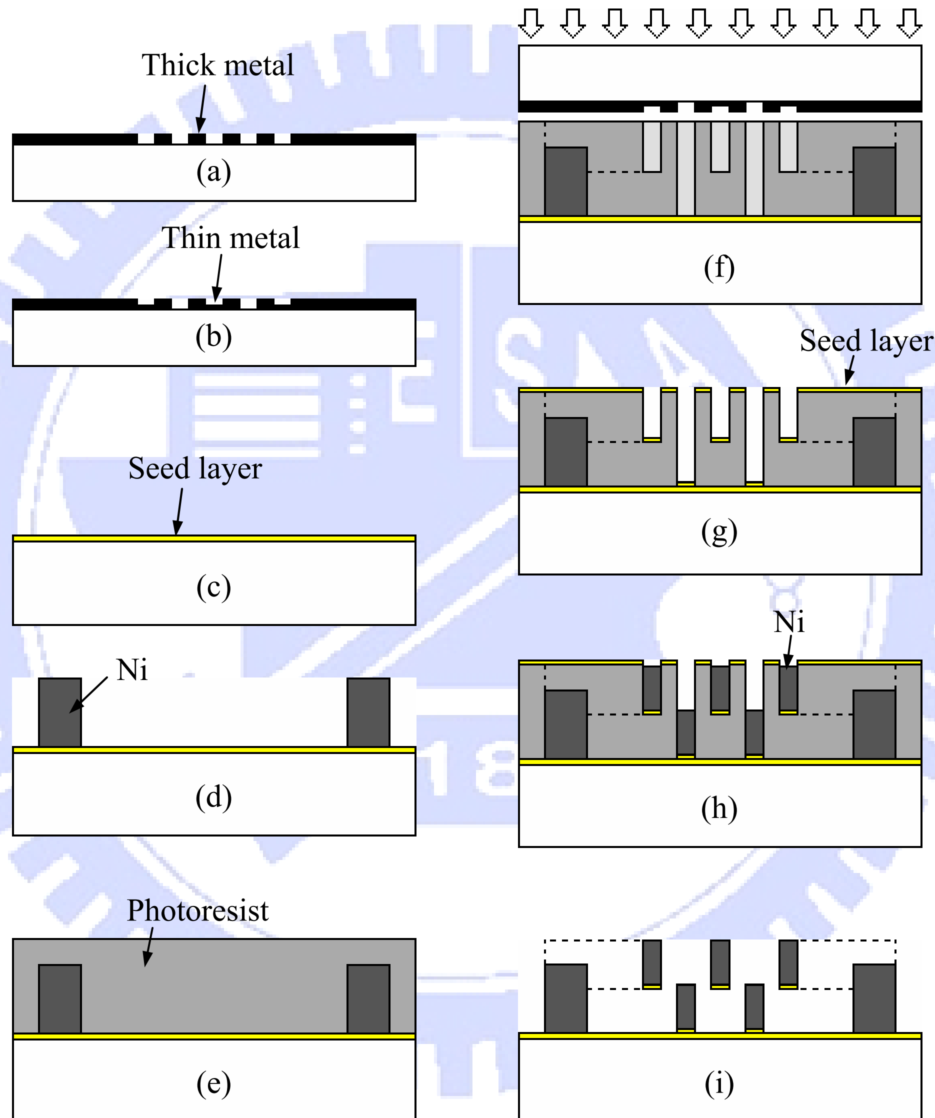

Figure 56. Process flow on AA cross-section to fabricate the metal-based VCD through multi-level photoresist mold; (a) deposit thick metal film; (b) deposit thin metal film; (c) deposit seed layer; (d) electroform nickel posts; (e) coating thick photoresist; (f) front side multiple exposure with the glass wafer; (g) deposit 2nd seed layer; (h) electroform nickel structures; (i) release.

metal-based VCD, including the upper fingers, lower fingers, torsion plate, and torsion springs (figure 56(h)). Finally, the VCD is fabricated after removing the photoresist molds (figure 56(i)).

The second approach introduces the electroformed copper as a sacrificial layer to set up the upper fingers for the required operation space. The detailed process is shown in figure 57. First, the seed layer is patterned by lift-off process and divided into two groups, electrode A and electrode B, where the electrodes A and B provide the electroplating current for the lower and upper fingers, respectively (figures 57(a) and 57(b)). Then, a thick photoresist is spin-coated and defined as the electroplating molds (figure 57(c)), and the lower fingers are constructed by nickel electroplating with current provided only by electrode A (figure 57(d)). Then, the copper and nickel are electroformed in turn to form the sacrificial layer and upper fingers with current provided only by electrode B (figure 57(e)). After removing the molds (figure 57(f)), nickel is electroformed to construct the anchors of the suspending comb structures (figure 57(g)), where current is supplied by electrode B. Finally, the sacrificial copper layer is removed by wet etching, and the metal-based VCD is fabricated (figure 57(h)).

These two approaches are simpler and more feasible than the original method described in Chapter 6, and both of them just require three photo masks totally.

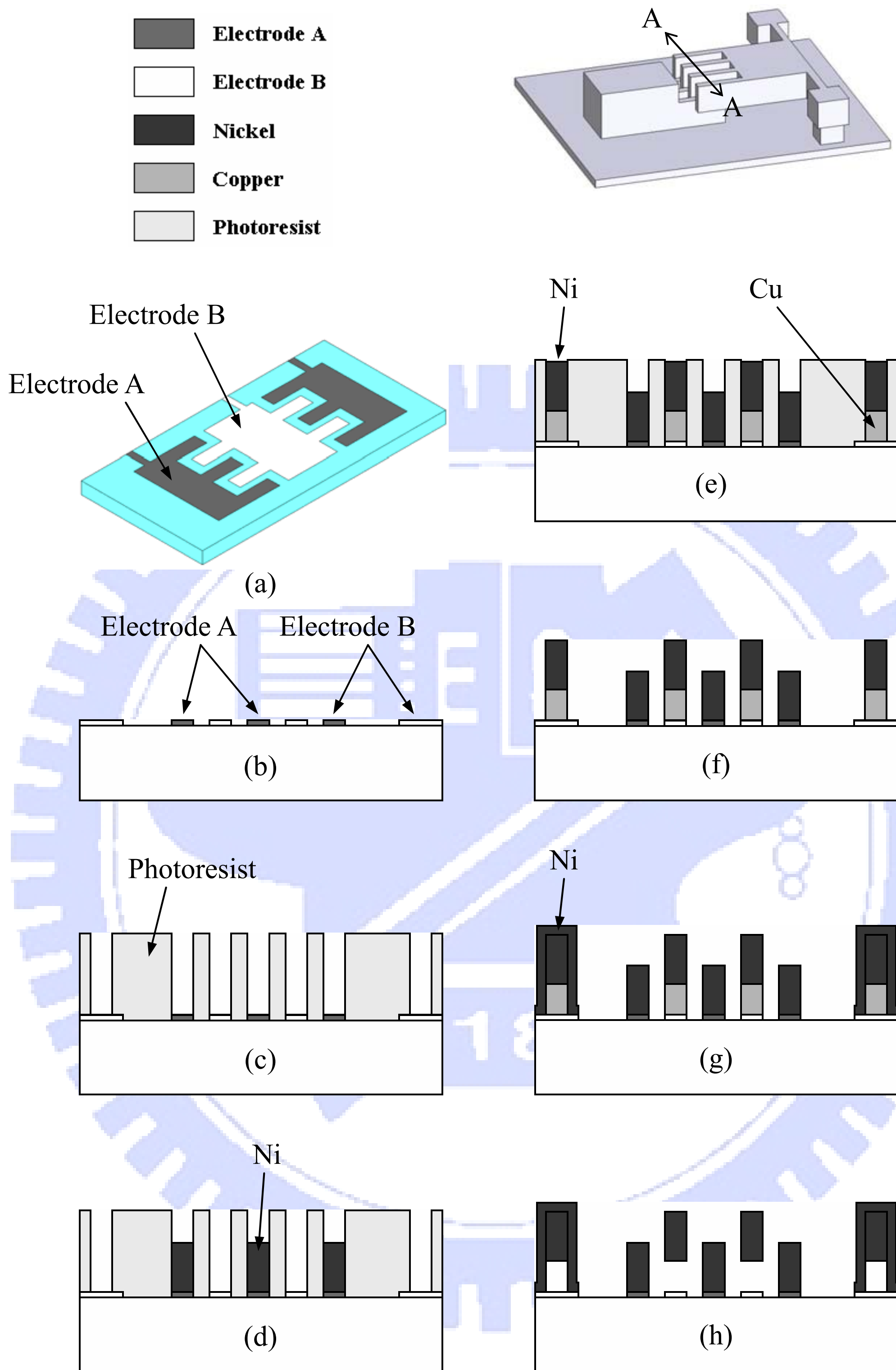

Figure 57. Process flow on AA cross-section to fabricate the metal-based VCD through the patterned seed layer; (a)–(b) pattern the seed layer; (c) construct the electroplating molds; (d) electroform nickel as the lower fingers (e) electroform copper and nickel in turn as the sacrificial layer and upper fingers; (f) remove molds; (g) electroform nickel as the anchors; (h) release.

References

[1] W.C. Tang, T.H. Nguyen and R.T. Howe, "Laterally driven polysilicon resonant microstructures" Tech. Dig. IEEE Micro Electro Mech. Syst. Workshop, pp.53–59, Salt Lake City, 20–22 Feb., 1989

[2] W. Ye, S. Mukherjee and N.C. MacDonald, "Optimal shape design of an electrostatic comb drive in microelectromechanical systems", *J. Microelectromech. Syst.*, vol. 7, pp.16–26, 1998

[3] T. Hirano, T. Furuhata, K.J. Gabriel and H. Fujita, "Design, fabrication, and operation of submicron gap comb-drive microactuators", *J. Microelectromech. Syst.*, vol. 1, pp.52–59, 1992

[4] L. Lin, R.T. Howe and A.P. Pisano, "Microelectromechanical filters for signal processing", *J. Microelectromech. Syst.*, vol. 7, pp.286–294, 1998

[5] K.Y. Park, W.C. Lee, H.S. Jang, Y.S. Oh and B.J. Ha, "Capacitive sensing type surface micromachined silicon accelerometer with a stiffness tuning capability", Dig. IEEE/ASME MEMS Workshop, pp.637–642, Heidelberg, Germany, 1998

[6] K. Tanaka, Y. Mochida, M. Sugimoto, K. Moriya, T. Hasegawa, K. Atsuchi and K. Ohwada, "A micromachined vibrating gyroscope", *Sensors and Actuators A*, vol. 50, pp.111–115, 1995

[7] W.-H. Juan and S.W. Pang, "High-aspect-ratio Si vertical micromirror arrays for optical switching", *J. Microelectromech. Syst.*, vol. 7, pp.207–213, 1998

[8] D. Hah, S. T.-Y. Huang, J.-C. Tsai, H. Toshiyoshi and M.C. Wu, "Low-voltage, large-scan angle MEMS analog micromirror arrays with hidden vertical comb-drive actuators", *J. Microelectromech. Syst.*, vol. 13, pp.279–289, 2004

[9] A. Selvakumar and K. Najafi, "Vertical comb array microactuators", *J. Microelectromech. Syst.*, vol. 12, pp.440–449, 2003

[10] J.-H. Lee, Y.-C. Ko, D.-H. Kong, J.-M. Kim, K.B. Lee and D.-Y. Jeon, "Design and fabrication of scanning mirror for laser display", *Sensors and Actuators A*, vol. 96, pp.223–230, 2002

[11] J.-L. A. Yeh, H. Jiang and N.C. Tien, "Integrated polysilicon and DRIE bulk silicon micromachining for an electrostatic torsional actuator", *J. Microelectromech. Syst.*, vol. 8, pp.456–465, 1999

[12] D. Hah, C.-A. Choi, C-K Kim and C-H Jun, "A self-aligned vertical comb-drive actuator on an SOI wafer for a 2D scanning micromirror", *J. Micromech. Microeng.*, vol. 14, pp.1148–1156, 2004

[13] V. Milanović, "Multilevel beam SOI-MEMS fabrication and applications", *J. Microelectromech. Syst.*, vol. 13, pp.19–30, 2004

[14] Q.X. Zhang, A.Q. Liu, J. Li and A.B. Yu, "Fabrication technique for

microelectromechanical systems vertical comb-drive actuators on a monolithic silicon substrate", *J. Vac. Sci. Technol. B*, vol. 23, pp.32–41, 2005

[15] J. Kim, S. Park and D. Cho, "A novel electrostatic vertical actuator fabricated in one homogeneous silicon wafer using extended SBM technology", Proc. of Transducers'01, pp.756-759, 2001

[16] J. M.-L. Tsai, H.-Y. Chu, J. Hsieh and W. Fang, "The BELST II process for a silicon high-aspect-ratio micromaching vertical comb actuator and its applications", *J. Micromech. Microeng.*, vol. 14, pp.235–241, 2004

[17] K.-H. Jeong and L.P. Lee, "A novel microfabrication of a self-aligned vertical comb drive on a single SOI wafer for optical MEMS applications", *J. Micromech. Microeng.*, vol.15, pp.277–281, 2005

[18] D. Hah, P. R. Patterson, H. D. Nguyen, H. Toshiyoshi and M. C. Wu, "Theory and experiments of angular vertical comb-drive actuators for scanning micromirrors", *J. Selected Topics In Quantum Electronics*, vol. 10, no.3, pp.505–513, 2004

[19] J. C. Chiou and Y. J. Lin, "A novel large displacement electrostatic actuator: pre-stress comb-drive actuator", *J. Micromech. Microeng.*, vol. 15, pp.1641–1648, 2005

[20] J. Kim, H. Choo, L. Lin and R. S. Muller, "Microfabricated torsional actuator using self-aligned plastic deformation", Proc. of Transducers'03, pp.1015–1018, 2003

[21] H. Becker and U. Heim, "Hot embossing as a method for the fabrication of polymer high aspect ratio structures", *Sensors and Actuators A*, vol. 83, pp.130–135, 2000

[22] G.-B. Lee, S.-H. Chen, G.-R. Huang, W.-C. Sung and Y.-H. Lin, "Microfabricated plastic chips by hot embossing methods and their applications for DNA separation and detection", *Sensors and Actuators B*, vol. 75, pp.142–148, 2001

[23] H. Becker and C. Gärtner, "Polymer microfabrication methods for microfluidic analytical applications", *Electrophoresis*, vol. 21, pp.12–26, 2000

[24] P. Abgrall, "Lab-on-chip technologies: making a microfluidic network and coupling it into a complete microsystem—a review", *J. Micromech. Microeng.*, vol. 17, pp.R15–R49, 2007

[25] Y. Zhao and T. Cui, "Fabrication of high-aspect-ratio polymer-based electrostatic comb drives using the hot embossing technique", *J. Micromech. Microeng.*, vol. 13, pp.430–435, 2003

[26] W. Dai, K. Lian and W. Wang, "Design and fabrication of a SU-8 based electrostatic microactuator", *Microsyst. Technol.*, vol. 13, pp.271–277, 2007

[27] S. J. Jeong and W. Wang, "Microaccelerometers using cured SU-8 as structural material", Proc. of SPIE, vol. 5344, pp.115–123, 2004

[28] W. Eberhardt, Th. Gerhäußer, M. Giousouf, H. Kück, R. Mohr and D. Warkentin, "Innovative concept for the fabrication of micromechanical sensor and actuator devices using selectively metallized polymers", *Sensors and Actuators A*, vol. 97–98, pp.473–477, 2002

[29] M. J. Madou, Fundamentals of Microfabrication, second ed., CRC Press, New York, 2002
[30] P. M. Zavracky, S. Majumder and N. E. McGruer, "Micromechanical switches fabricated using nickel surface micromachining", *J. Microelectromech. Syst.*, vol. 6, pp.3–9, 1997
[31] C.-H. Ho, K.-P. Chin, C.-R. Yang, H.-M. Wu and S.-L. Chen, "Ultrathick SU-8 mold formation and removal, and its application to the fabrication of LIGA-like micromotors with embedded roots", *Sensors and Actuators A*, vol. 102, pp.130–138, 2002
[32] C. Hsu and W. Hsu, "Design and characterization of an electrothermally driven monolithic long-stretch microdrive in compact arrangement", *J. Microelectromech. Syst.*, vol. 15, pp.935–944, 2006
[33] Y. Konaka and M. G. Allen, "Single- and multi-layer electroplated microaccelerometers", Proc. of MEMS'96, pp.168–173, 1996
[34] W. Qu, C. Wenzel and G. Gerlach, "Fabrication of a 3 Ddifferential-capacitive acceleration sensor by UV-LIGA", *Sensors and Actuators A*, vol. 77, pp.14–20, 1999
[35] J.-B. Yoon, C.-H. Han, E. Yoon and C.-K. Kim, "Monolithic fabrication of electroplated solenoid inductors using three-dimensional photolithography of a thick photoresist", *Jpn. J. Appl. Phys.*, vol. 37, pp.7081–7085, 1998
[36] G. M. Rebeiz, RF MEMS—Theory, Design, and Technology, John Wiley & Sons, Inc., New Jersey, 2003
[37] C. K. Ullal, M. Maldovan, E. L. Thomas, G. Chen, Y. -J. Han and S. Yang, "Photonic crystals through holographic lithography: Simple cubic, diamond-like, and gyroid-like structures", *Appl. Phys. Lett.*, vol. 84, pp.5434–5436, 2004
[38] Y. Y. Li, F. Cunin, J. R. Link, T. Gao, R. E. Betts, S. H. Reiver, V. Chin, S. N. Bhatia and M. J. Sailor, "Polymer replicas of photonic porous silicon for sensing and drug delivery applications", *Science*, vol. 299, pp.2045–2047, 2003
[39] B. H. Cumpston, S. P. Ananthavel, S. Barlow, D. L. Dyer, J. E. Ehrlich, L. L. Erskine, A. A. Heikal, S. M. Kuebler, I.-Y. S. Lee, D. McCord-Maughon, J. Qin, H. Rockel, M. Rumi, X.-L. Wu, S. R. Marder and J. W. Perry, "Two-photon polymerization initiators for three-dimensional optical data storage and microfabrication", *Nature*, vol. 398, pp.51–54, 1999
[40] A. Abbott, "Biology's new dimension", *Nature*, vol. 424, pp.870–872, 2003
[41] M. Han, W. Lee, S.-K. Lee and S. S. Lee, "3D microfabrication with inclined/rotated UV lithography," *Sensors and Actuators A*, vol. 111, pp.14–20, 2004
[42] B.-G. Kim, J.-H. Kim and E. Yoon, "Formation of 3-dimensional microfluidic components using double-side exposed thick photoresist molds," 7th International Conference on Miniaturized Chemical and Biochemical Analysis Systems, pp.627–630, Squaw Valley, California, USA, Oct. 5-9, 2003

[43] Y.-J. Chuang, F.-G. Tseng, J.-H. Cheng and W.-K. Lin, "A novel fabrication method of embedded micro-channels by using SU-8 thick-film photoresists", *Sensors and Actuators A*, vol. 103, pp.64–69, 2003

[44] R. A. Farrer, C. N. LaFratta, L. Li, J. Praino, M. J. Naughton, B. E. A. Saleh, M. C. Teich and J. T. Fourkas, "Selective functionalization of 3-D polymer microstructures", *J. Am. Chem. Soc.*, vol. 128, pp.1796–1797, 2006

[45] N.-T. Nguyen, S.-S. Ho and C. L.-N. Low, "A polymeric microgripper with integrated thermal actuators," *J. Micromech. Microeng.*, vol. 14, pp.969–974, 2004

[46] A. Bertsch, H. Lorenz and P. Renaud, "3D microfabrication by combining microstereolithography and thick resist UV lithography", *Sensors and Actuators A*, vol. 73, pp.14–23, 1999

[47] S. Maruo, O. Nakamura and S. Kawata, "Three-dimensional microfabrication with two-photon-absorbed photopolymerization", *Optics Letters*, vol. 22, pp.132–134, 1997

[48] S. Kawata, H.-B. Sun, T. Tanaka and K. Takada, "Finer features for functional microdevices", *Nature*, vol. 412, pp.697–698, 2001

[49] T. Baldacchini, C. N. LaFratta, R. A. Farrer, M. C. Teich, B. E. A. Saleh, M. J. Naughton and J. T. Fourkas, "Acrylic-based resin with favorable properties for three-dimensional two-photon polymerization", *J. Appl. Phys.*, vol. 95, pp.6072–6076, 2004

[50] C. N. LaFratta, L. Li and J. T. Fourkas, "Soft-lithographic replication of 3D microstructures with closed loops", *PNAS-Proceedings of the National Academy of Science of the USA*, vol. 103, no. 23, pp.8589–8594, 2006

[51] J. H. Moon and S. Yang, "Creating three-dimensional polymeric microstructures by multibeam interference lithography", *Journal of Macromolecular Science - Polymer Reviews*, vol. 45, pp.351–373, 2005

[52] K.-Y. Hung, H.-T. Hu and F.-G. Tseng, "A novel fabrication technology for smooth 3D inclined polymer microstructures with adjustable angles," The 12th International Conference on Solid State Sensors, Actuators and Microsystems (Transducers'03), pp.821–824, Boston, June 8-12, 2003

[53] Y. Oppliger, P. Sixt, J. M. Stauffer, J. M. Mayor, P. Regnault and G. Voirin, "One-step 3D shaping using a gray-tone mask for optical and microelectronic applications", *Microelectronic Engineering*, vol. 23, pp.449–454, 1994

[54] B. Wagner, H. J. Quenzer, W. Henke, W. Hoppe and W. Pilz, "Microfabrication of complex surface topographies using grey-tone lithography", *Sensors and Actuators A*, vol. 46–47, pp.89–94, 1995

[55] W. Däschner, P. Long, R. Stein, C. Wu and S. H. Lee, "General aspheric refractive micro-optics fabricated by optical lithography using a high energy beam sensitive glass gray-level mask", *J. Vac. Sci. Technol. B*, vol. 14, pp.3730–3733, 1996

[56] W. Däschner, P. Long, M. Larsson and S. H. Lee, "Fabrication of diffractive optical elements using a single optical exposure with a gray level mask", *J. Vac. Sci. Technol. B*, vol. 13, pp.2729–2731, 1995

[57] E. Mazza, S. Abel and J. Dual, "Experimental determination of mechanical properties of Ni and Ni-Fe microbars", *Microsystem Technologies*, vol. 2, pp.197–202, 1996

[58] W. N. Sharpe Jr., D.V. LaVan and R. L. Edwards, "Mechanical properties of LIGA-Deposited Nickel for MEMS Transducers", *International Conference on Solid-State Sensors and Actuators (Transducers'97)*, pp.607–610, 1997

[59] T. E. Buchheit, S. J. Glass, J. R. Sullivan, S. S. Mani, D. A. Lavan, T. A. Friedmann and R. Janek, "Micromechanical testing of MEMS materials", *Journal of Materials Science*, vol. 38, no. 20, pp.4081–4086, 2003

[60] T. Fritz, H. S. Cho, K. J. Hemker, W. Mokwa and U. Schnakenberg, "Characterization of electroplated nickel", *Microsyst. Technol.*, vol. 9, pp.87–91, 2002

[61] K. J. Hemker and H. Last, "Microsample tensile testing of LIGA nickel for MEMS applications", *Materials Science and Engineering*, A319-321, pp.882–886, 2001

[62] H. S. Cho, K. J. Hemker, K. Lian, J. Goettert and G. Dirras, "Measured mechanical properties of LIGA Ni structures", *Sensors and Actuators A*, vol. 103, pp.59–63, 2003

[63] L. H. Qian, S. C. Wang, Y. H. Zhao and K. Lu, "Microstrain effect on thermal properties of nanocrystalline Cu", *Acta Materialia*, vol. 50, pp.3425–3434, 2002

[64] I. W. Gazda, "Variations in CTE as a function of prestressing", *Carbon*, vol. 8, pp. 511–515, 1970

[65] W. Fang and C. Y. Lo, "On the thermal expansion coefficients of thin films", *Sensors and Actuators A*, vol. 84, pp.310–314, 2000

[66] J. W. Dini and H. R. Johnson, "Coefficient of thermal expansion of sulphamate nickel electrodeposits", *Journal of Materials Science Letters*, vol. 10, pp.1253–1254, 1975

[67] C. S. Pan and W. Hsu, "A microstructure for in-situ determination of residual strain", *Journal of Microelectromechanical systems*, vol. 8, no. 2, pp.200–207, 1999

[68] W. C. Oliver and G. M. Pharr, "An improved technique for determining hardness and elastic modulus using load and displacement sensing indentation experiments", *J. Mater. Res.*, vol. 7, pp.1564–1583, 1992

[69] J. Lou, S. Allameh, T. Buccheit and W. O. Soboyejo, "An investigation of the effects of thickness on mechanical properties of LIGA nickel MEMS structures", *Journal of Materials Science*, vol. 38, no. 20, pp.4129–4135, 2003

[70] C.-M. Cheng and R.-H. Chen, "Experimental investigation of fabrication properties of electroformed Ni-based micro mould inserts", *Microelectronic Engineering*, vol. 75, pp.423–432, 2004

[71] L. L. Chu, L. Que and Y. B. Gianchandani, " Temperature coefficients of material properties for electrodeposited MEMS", Proc. of MEMS'01, pp.68–71, 2001

[72] J. Aktaa, J. Th. Reszat, M. Walter, K. Bade and K. J. Hemker, "High cycle fatigue and

fracture behavior of LIGA nickel", *Scripta Materialia*, vol. 52, pp.1217–1221, 2005
[73] H. D. Espinosa and B. C. Prorok, "Size effects on the mechanical behavior of gold thin films", *Journal of Materials Science*, vol. 38, no. 20, pp.4125–4128, 2003
[74] C.-W. Baek, Y.-K. Kim, Y. Ahn and Y.-H. Kim, "Measurement of the mechanical properties of electroplated gold thin films using micromachined beam structures", *Sensors and Actuators A*, vol. 117, pp.17–27, 2005
[75] J. W. Dini, Electrodeposition: the materials science of coatings and substrates, Noyes Publications, New Jersey, 1992
[76] M. Bartek and R. F. Wolffenbuttel, "Dry release of metal structures in oxygen plasma: process characterization and optimization", *J. Micromech. Microeng.*, vol. 8, pp.91–94, 1998
[77] T. P. Moffat, D. Wheeler, W. H. Huber and D. Josell, "Superconformal electrodeposition of copper", *Electrochemical and Solid-State Letters*, vol. 4, pp.C26–C29, 2001
[78] D. Josell, B. Baker, C. Witt, D. Wheeler and T. P. Moffat, "Via filling by electrodeposition superconformal silver and copper and conformal nickel", *Electrochemical and Solid-State Letters*, vol. 149, pp.C637–C641, 2002
[79] R. Birringer, "Nanocrystalline materials," *Materials Science and Engineering*, A117, pp.33–43, 1989
[80] K. Lu and M.L. Sui, "Thermal expansion behaviors in nanocrystalline materials with a wide grain size range," *Acta Metallurgica Materialia*, vol. 43, no. 9, pp.3325–3332, 1995
[81] H. Zhang and B.S. Mitchell, "Thermal expansion behavior and microstructure in bulk nanocrystalline selenium by thermomechanical analysis," *Materials Science and Engineering*, A270, pp.237–243, 1999